THE UNIVERSITY OF CHICAGO

REMOTE ENTANGLEMENT VIA ADIABATIC PASSAGE USING A TUNABLY DISSIPATIVE QUANTUM COMMUNICATION SYSTEM

A DISSERTATION SUBMITTED TO
THE FACULTY OF THE PRITZKER SCHOOL OF MOLECULAR ENGINEERING
IN CANDIDACY FOR THE DEGREE OF
DOCTOR OF PHILOSOPHY

BY
HUNG-SHEN CHANG

CHICAGO, ILLINOIS
MARCH 2021

To my parents, Chih-Chieh Chang and Pi-Fen Hong

CONTENTS

LIST OF FIGURES

LIST OF TABLES

ACKNOWLEDGMENTS

It has been a fantastic five years at the University of Chicago. Working on cutting-edge quantum communication research in a world-leading institution has been a dream come true. My time in Chicago has been nothing less than phenomenal. It has defined and will continue to shape me significantly as a researcher. I am deeply grateful for the numerous people who have joined me on this journey. From the bottom of my heart, thank you.

First and foremost, I want to thank my graduate advisor, Andrew Cleland. I vividly remember five years ago, equipped with nothing but a passion for research, I strode into his office to talk about research opportunities. Despite my lack of background, he gave me an opportunity to work in the lab. Together with the rest of the group, we have turned the once empty lab spaces in Eckhardt Research Center into several platforms capable of performing world-leading superconducting quantum communication research. Andrew, I want to thank you for believing in me and giving me this opportunity. There are very few places where complex experiments like the ones in this thesis can be realized. Thank you for giving me the opportunity to carry these out here in Chicago. I also want to thank you for your advice and guidance during these five years, making sure that I have everything I need to succeed every step of the way. I would not be who I am today without the patience and effort that you have put forth for me. Lastly, thank you for assembling a group of smart *and* nice people to work with. It has truly been an honor to work and learn from them.

To my committee member David Awschalom and Dave Schuster, thank you for serving on my committee in the past five years. Together with Andrew, you have built an amazing quantum community here in Chicago which I have heavily benefited from. Here in the PME, I have been presented with opportunities and resources that would have been unimaginable in other institutions. The inclusive and supportive quantum community in the PME has also played a crucial role in my life in Chicago, both inside and outside the lab. It has been a pleasure being part of this community.

Youpeng has been my comrade-in-arms from the very beginning. Youpeng, thank you for everything in the past five years: the various qubit measurements and microwave control electron-

ics lessons, encouragement and sound advice, and most importantly, our friendship. Although our journey together in Chicago is ending soon, I sincerely hope our friendship continues. I firmly believe that both of us will do great things in the future and will look back to our memories in Chicago with pride and joy.

Another mentor I have the privilege to have in the earlier part of my PhD journey is Kevin Satzinger. Kevin, thank you for believing in me and taking me under your wings. You are a living reminder that dreams do come true and I take you as a role model in everything I do, holding myself to the "Satzinger standard". Whenever I want to "think happy thoughts", I close my eyes and reminisce of our time working together in the lab, one of the happiest memories I have in Chicago.

I am also in debt to our two postdocs, Audrey Bienfait and Étienne Dumur, who played a large role in helping us set up the lab from the ground up. Audrey, mother of fridges and junctions, thank you for your straightforward answers and comments to my questions. I also want to thank you for your much-needed words of encouragement during the hard times. To Étienne, *merci* for always having your door open and willing to answer any question I have any time of the day. I want you to know that I do not take your willingness to help for granted. I will cherish our memories from watching movies downtown to enjoying Chinese food in Chinatown. To other members of the lab: Ming-Han Chou, Chris Conner, Joel Grebel, and Haoxiong Yan, it has been a pleasure working with you. With you, I know the lab is in good hands and I wish you the best of luck.

None of the experiments would have been possible without the support we received outside the lab. To our clean room manager, Peter Duda, thank you for hanging in there with me through the ups and downs in the past few years. Bringing up a clean room is hard; both you and I know from firsthand experience. However, we are very fortunate to have you on our side to assist us in the process. As I am heading toward the completion of my PhD, I want to say: thank you for enabling us to make cool working quantum devices. To our administrative assistant, Mary Pat McCullough, thank you for being part of my journey in Chicago. From finding a spot in Andrew and David's calendars for me to meet with them last minute to overcoming all sorts of

hurdles UChicago procurement service throws at us. It takes a village to do what we do and we are fortunate to have you to assist (shield) us from the administrative and financial burdens that come with it. So, thank you!

To our extended families, Awschalom group and Schuster group, thank you for your constant companionship from the very beginning. It can be isolating at times budding my head at the setup and trying to figure out what is wrong with my experiment. It is nice to have someone right next door to bounce ideas off of. Awschalom group, thank you for treating me like family and inviting me to your familial group lunches over the years. In particular, to the SiC team whom I have grown close to over the years: Kevin Miao, Chris Anderson, Alex Bourassa, and Alex Crook, thank you for the fun and stimulating discussions in the hallways of ERC. I have learned so much from these hallway discussions and I consider it an honor to have overlapped with you in my time in Chicago. I cherish our friendship and hope to keep in touch. To Schuster group, in particular: Nate Earnest, Yao Lu, Nelson Leung, Kan-Heng Lee, and Vatsan Chakram, thank you for the various discussions on superconducting qubit physics, E_J's and E_C's, and junction fabrication. It is truly great to have another superconducting qubit group here in Chicago.

To my undergraduate advisor, Greg Fuchs, thank you for betting on a freshman with nothing but a passion for quantum research in 2012. You have opened my eyes and pulled me into the world of quantum research and I have not looked back ever since. You are one of the reasons that I have embarked on this journey in Chicago in the first place. I also want to thank Greg Calusine and Will Oliver at MIT Lincoln Laboratories for providing the traveling-wave parametric amplifier (TWPA) used in this work. Without it, the high readout fidelity reported in this work would not have been possible.

Finally, mom and dad, thank you for your unwavering support and love. You know better than anyone that becoming a capable scientist has been my dream ever since I was little. With this thesis, I am happy to say *we* did it!

ABSTRACT

Effective quantum communication between remote quantum nodes requires high fidelity quantum state transfer and remote entanglement generation. Recent experiments have demonstrated that microwave photons, as well as phonons, can be used to couple superconducting qubits, with a fidelity limited primarily by loss in the communication channel. Adiabatic protocols can overcome channel loss by transferring quantum states without populating the lossy communication channel. In this thesis, we present a unique superconducting quantum communication system, comprising two superconducting qubits connected by a 0.73 m-long communication channel. We begin by discussing the operation of a qubit and a tunable coupler, the basic elements comprising our superconducting quantum node. Next, we describe a fast and large bandwidth variable coupler that allows us to introduce loss to the channel. Finally, we integrate all these elements together on-chip to form a tunably-dissipative quantum communication platform comprising two qubits coupled through a 0.73 m-long transmission line via a pair of electrically-tunable couplers. Significantly, we show that the integration of the variable coupler allows us to introduce large tunable loss to the channel, with which the single photon lifetime in the line can be controllably reduced from its intrinsic value by over two orders of magnitude. This enables exploration of different entanglement protocols in the presence of significant channel loss. When set for minimum loss in the channel, we demonstrate an adiabatic quantum state transfer protocol that achieves 99% transfer efficiency as well as the deterministic generation of entangled Bell states with a fidelity of 96%, all without populating the intervening communication channel, and competitive with a qubit-resonant mode-qubit relay method. We also explore the performance of the adiabatic protocol in the presence of significant channel loss, and show that the adiabatic protocol protects against loss in the channel, achieving higher state transfer and entanglement fidelities than the relay method.

CHAPTER 1

INTRODUCTION

To begin, we provide the motivation and background of this thesis as well as a brief review of prior work of quantum communication with superconducting qubits. We will conclude with our approach of quantum communication, entangling two qubits over a cable without sending any photons through the cable.

1.1 Quantum bits

The basis of any quantum information system is a two-level system called a qubit.[1] The information is encoded in the superposition of the two basis states, typically the ground and excited states of the two-level system, $|g\rangle$ and $|e\rangle$ respectively.[2] The quantum state of a qubit can not only be in either state but also be in any *superposition* of these two states. We can express the quantum state of a qubit $|\psi\rangle$ as

$$|\psi\rangle = \cos(\theta/2)|g\rangle + \sin(\theta/2)e^{i\phi}|e\rangle. \tag{1.1}$$

This state $|\psi\rangle$ is often visually represented by a vector from the origin to a point on the surface of a unit sphere called the Bloch sphere, where θ and ϕ in Eq. 1.1 correspond to the polar and azimuthal angles of the vector on the sphere; see Fig. 1.1. More complex superposition states $|0\cdots00\rangle, \cdots, |1\cdots11\rangle$ can be formed with a multi-qubit system. Typically, a multi-qubit state formed by N qubits has $2^N - 1$ degrees of freedom. This is in sharp contrast to classical computing where a N bit system only has N degrees of freedom.

1. For completeness, there also exist proposals using a three-level system called a qutrit as the building block for quantum information processing, although these approaches are less common.

2. Here we have presupposed a system where the two states have different energies which is not always the case.

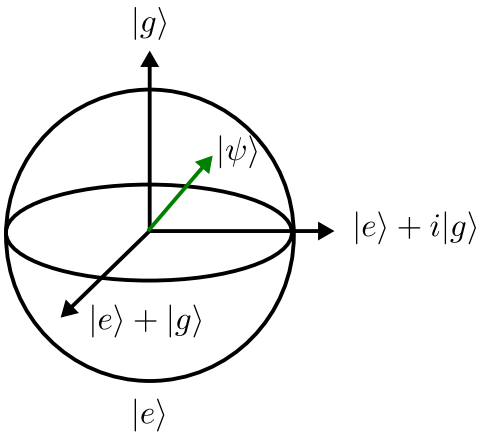

Figure 1.1: Bloch sphere representation of a qubit. The ground state $|g\rangle$ lies at the top of the Bloch sphere and the excited state $|e\rangle$ at the bottom. Any equal superposition state lies on the equator of the sphere.

Additionally, non-classical correlation can exist between quantum bits through *entanglement*, the topic of this thesis. Quantum computers harness these quantum properties, superposition and entanglement, to provide speedup compared to classical computers. A number of computational problems otherwise intractable for classical computers can potentially be solved in a reasonable time using quantum algorithms on quantum computers, with the most well-known example of prime factorization with Shor's algorithm [1].

1.2 Superconducting qubits

There are many candidates for the implementation of a qubit. Fundamentally, any physical system with a pair of states whose transition can be individually addressed can be used as a qubit. Defect centers in crystals [2, 3], superconducting quantum circuits [4], trapped ions [5], silicon qubits [6, 7], and neutral atoms [8] have all been explored as candidate qubits with varying degrees of success for fundamental quantum operation. Large scale quantum computation imposes two conflicting conditions on the qubit [9]:

1. *Long coherence*: The qubit must be robust against decoherence and dephasing. Quantum states are extremely fragile; any unwanted coupling with the surrounding environment can

destroy the quantum state of the qubit, thereby destroying the information stored in the qubit.

2. *Fast operation and readout*: One needs to be able to access, manipulate, and interface the qubit with another qubit to carry out computation.

Thus, the qubit must be well isolated in order to retain coherence, yet easily manipulated and read out to enable fast quantum operations and measurement. These nearly conflicting requirements are the challenges that face all quantum computation systems today.

Superconducting quantum circuits have emerged as one of the most promising systems for quantum computation in the last decade. Unlike other systems which use the quantum effects of subatomic particles, superconducting quantum circuits use the state of the electromagnetic field of non-linear superconducting circuits to encode the qubit. Consequently, superconducting qubits can be easily controlled and coupled by engineering their electromagnetic environment. In fact, as these quantum systems are built from circuit components, they can be precisely engineered and laid out using computer-aided design (CAD) software. Their circuit design can be simulated and verified with numerical simulation. In our lab, we verify our circuit designs using finite element electromagnetic simulation software *Sonnet*[3] and numerical circuit simulator *Qucs*[4]. Another significant advantage of superconducting qubits is that they are highly scalable and integratable. Superconducting qubits are fully compatible with existing semiconductor processing technology and can be readily fabricated in a clean room using standard lithography and etching processes. Additionally, similar to standard integrated circuit fabrication, several superconducting qubit chips can be made in parallel on a large wafer to compensate for variation in the fabrication.

However, since superconducting qubits rely on a macroscopic quantum state, they are more susceptible to decoherence due to unwanted interactions with the environment than other candidate qubits. Nevertheless, through a combination of improved materials, careful circuit engineering, and careful microwave filtering, superconducting quantum circuits have progressed significantly over the last two decades. For example, qubit coherence has increased by more than four orders of

3. https://www.sonnetsoftware.com/

4. http://qucs.sourceforge.net/

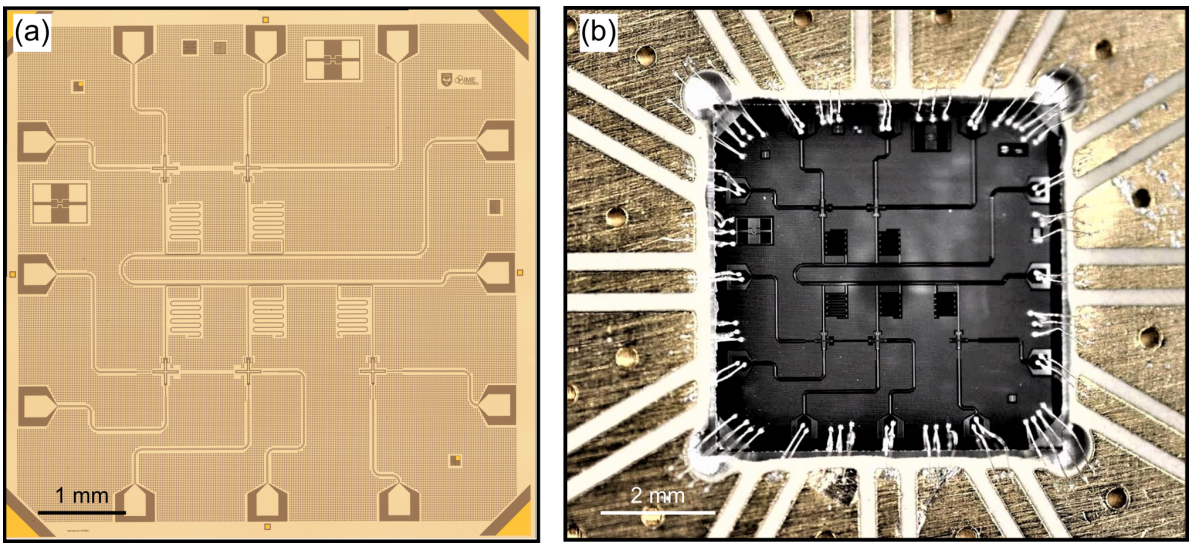

Figure 1.2: (a) A superconducting 5-qubit test device we made in the lab. (b) The 5-qubit test device packaged inside a PCB sample box with aluminum wirebonds.

magnitudes [10] with both T_1 and T_2 now in the hundreds of microseconds.

Such technological advance has driven significant commercial interest. Industrial companies such as Google and IBM have started using superconducting qubits as building blocks for multi-qubit quantum computation systems, putting many superconducting qubits together and operating them simultaneously to carry out potentially useful quantum information processing. Using a quantum system with 53 superconducting qubits, "quantum supremacy", defined as the crossing point where a quantum computer provides speedup compared to a classical computer, has been demonstrated [11]. It is worth noting that to date the largest devices realized have on the order of $\sim 10^2$ qubits, and it remains an outstanding challenge to make devices with even more qubits (1000, 10,000, or even 100,000) needed to build a useful fault-tolerant universal quantum computer.

1.3 Quantum network

In classical computation, thousands of processors can be connected together via a network to form a powerful cluster. Information can be distributed across a large area in a fraction of a second and computation can be carried out in parallel across remote nodes. Analogously, quantum computers can also benefit from such a network [12, 13], enabling quantum-secured communication through

a quantum network and exponentially faster computation with distributed quantum computation [14]. A schematic of a quantum network where different quantum processor nodes are connected together is shown in Fig. 1.3. The processor at each node can be based on different qubit implementations, and by linking them together, we can take advantage of unique properties of each qubit implementation. For example, isolated quantum systems with high coherence such as the NV center in diamond can be used as storage nodes while highly controllable quantum systems such as superconducting qubit can be used as computation nodes in the network [12].

1.3.1 Scaling up with modules

A quantum network also provides a promising pathway of scaling up quantum systems by connecting different computing modules through the network. Entangled states can be shared across different nodes in the network though quantum communication, entangling distant modules together and forming a quantum processor with more computational power. There are significant advantages to scaling up with this approach. For example, for superconducting circuits-based quantum processors, the current approach is to fabricate all qubits of the processor on a single chip. This places stringent requirements on the fabrication as all qubits need to be fabricated precisely and flawlessly to have a perfectly working device. In a distributed quantum processor composed of several modules, individual modules can be independently fabricated, characterized, and replaced as needed. A broken module can simply be replaced while keeping the other modules. Furthermore, the quantum processor can be scaled up straightforwardly by connecting more modules which can similarly be individually characterized and fabricated. All-to-all connections between modules can be realized through the incorporation of multi-port variable coupler such as the one detailed in Chapter 3. Basic quantum networks have been demonstrated in the last few years, enabling for example the loophole-free violation of a Bell inequality across 3 km [15] and inter-continental entanglement distribution via satellite [16].

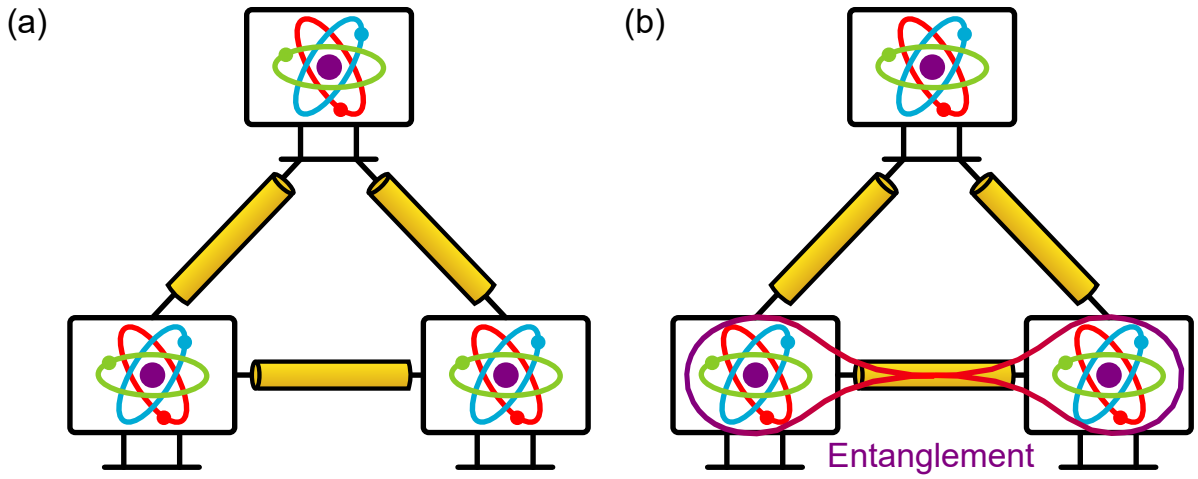

Figure 1.3: (a) Schematic of a quantum network where different quantum processor nodes, represented by an atom in the schematic, can be connected together. (b) Remote processor nodes can share quantum state and be entangled, forming a larger quantum processor in the aggregate.

1.3.2 Quantum communication with superconducting qubits

Despite its widespread use for quantum computation, the application of superconducting qubits for quantum communication in a quantum network has been limited. Unlike optical photon-based quantum systems which can be quantum coherent at room temperature, superconducting circuits must be operated at cryogenic environments with temperatures in the tens of milliKelvin. This is due to the fact that they work at microwave frequency and the environment must be cold enough $T \ll \hbar\omega/k_B$ to avoid thermal fluctuation in the environment from populating the qubit. Here, T is the temperature of the environment, $\hbar$ is the reduced Planck's constant, k_B is the Boltzmann constant, and ω is operating angular frequency of our qubit. Our typical qubits operate at $\omega/2\pi \approx 6$ GHz, corresponding to a temperature of $T = 0.3$ K. Typically, a dilution refrigerator with a base temperature of 10 mK is used to provide the sub-100 mK cryogenic environment required for the operation of superconducting qubits. Nevertheless, superconducting qubits provide an interesting platform for developing short-distance quantum communication and may lay the groundwork for a superconducting quantum circuit-based local quantum network.

1.4 Remote entanglement

A key resource of a quantum network is entanglement between remote quantum nodes. For example, in quantum communication protocols such as quantum key distribution [17], non-classical correlation between remote nodes due to entanglement is used as a resource to detect eavesdropping. This relies on the fact that a measurement on an entangled pair of qubits disturbs the entangled state. Thus, the entangled nodes can share their measurement results at the end of communication protocol and infer from the correlation of their results if eavesdropping has occurred.

Remote entanglement has been realized across a variety of quantum systems in the past decade: from atomic ensembles, trapped ions, and NV centers in diamond, to superconducting circuits and quantum dots [18]. The protocol to transfer quantum states between two distant nodes can be broadly categorized into two types: (1) probabilistic and (2) deterministic.

1.4.1 Probabilistic remote entanglement generation

A common probabilistic method for entanglement is through a beam splitter. In this method, two itinerant qubits are generated and sent through Hanbury Brown and Twiss setup. The two itinerant qubits can be entangled with a finite probability at the beam splitter and the successful generation of entanglement between the two can be heralded through detection at either of the outputs [19, 20, 21]. However, such protocols are probabilistic with low entanglement generation rates, defined as the experimental repetition rate of a successful entanglement generation. This limits their prospect for practical quantum communication. For example, the landmark experiment of the loophole-free violation of Bell inequality between two remote NV centers separated by 1.3 km utilizes this method for entanglement generation. The experiment suffers from an extremely low communication rates with an entanglement generation rate of $\sim 10^{-4}$, corresponding to one successful event every hour [15]. This limits the practicality of this method for entanglement generation in an actual quantum network.

1.4.2 Deterministic remote entanglement generation

Alternatively, remote entanglement can be generated deterministically by converting the stationary qubit at each node to an itinerant (flying) photon as carrier of information between nodes [22]. Specifically, to deterministically generate entanglement between the two nodes, a stationary photon at each node is partially converted to an itinerant one. The itinerant quantum is then caught by the other node and converted back to a stationary quantum, completing the entanglement generation between the two nodes. This approach allows for quantum state transfer and entanglement generation between remote nodes on demand. However, this approach faces another challenge. As shown in Fig. 1.4(a), the naturally released photon from a stationary qubit at each node has an exponentially decaying profile. This corresponds to an abrupt change in the time domain and has a significantly larger bandwidth than what can be obtained by the qubit. Such itinerant photon thus cannot be perfectly absorbed by another stationary qubit, limiting the transfer efficiency to at most 54% [22]. However, Cirac et al. [22] proposed in 1997 that if the wave packet is shaped in a time-symmetric manner by modulating the coupling between the nodes and the channel, 100% transfer fidelity is possible; see Fig. 1.4(b). In other words, if the coupling is modulated such that the emitted photon from the sender qubit has a symmetric wave packet, and the receiver qubit's coupling is tuned in the time-reversed manner, 100% state transfer fidelity is possible between the sender and receiver qubits through the channel. This proposal was later expanded by Korotkov et al. in 2011 [23] and proved to be key to deterministic generation of high fidelity remote entanglement for quantum communication. It is worth noting here that time symmetry is not an absolute requirement for perfect state transfer but is rather chosen as a useful condition for both theoretical and experimental considerations.

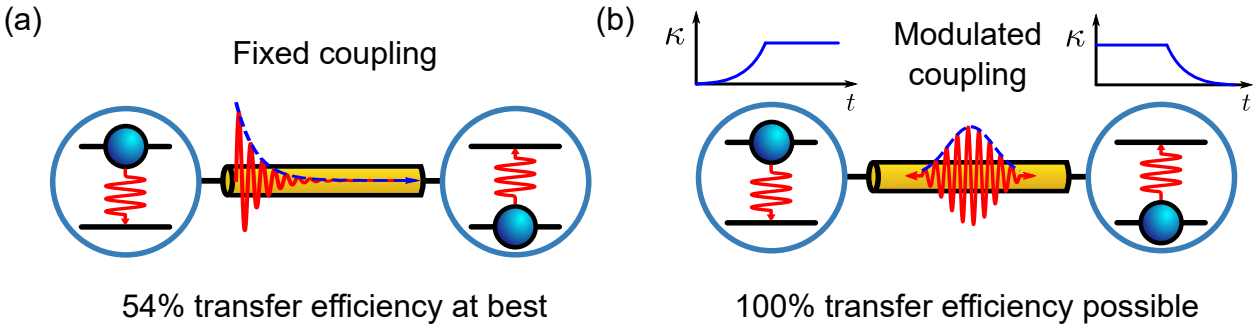

Figure 1.4: Pitch and catch of an itinerant photon. (a) A stationary qubit with fixed coupling has a natural exponentially decaying envelope (blue). Due to the wide spectral bandwidth of the envelope, the released photon cannot be captured perfectly by the other stationary qubit , limiting the transfer efficiency between the two qubits to 54% at best. (b) However, if the coupling is modulated in a time symmetric manner, a spectrally narrow symmetric itinerant photon can be emitted by the sender qubit and subsequently captured perfectly by the receiver qubit.

In 2018, Kurpiers et al. [18] realized the first experimental demonstration of the proposal by Cirac et al. and generated remote entanglement between superconducting qubits deterministically. They coupled two remote planar transmon qubits to two dedicated resonators which were then connected through a meter of coaxial cable. Due to the limited effective coupling between the node and the channel, a circulator was used to cancel out the reflection in the channel during the transfer to avoid interference from reflection. They reported the generation of a Bell state with 78.9% fidelity limited primarily by the loss in the channel, both from the various microwave components (circulators and connectors) and intrinsic to the channel itself [18]. Since then, quantum communication with superconducting qubits has progressed significantly using a variety of other approaches (3D and 2D) and coupling schemes.

In the same year, Axline et al. [24] and Campagne-Ibarcq et al. [25] carried out remote entanglement using a 3D architecture and parametric coupling. Concurrently, Leung et al. [26] and Zhong et al. [27] took an alternative approach and removed the circulator interrupting the channel (used to prevent reflection in the channel) to realize a low loss channel. To overcome the reflection in the channel, Zhong et al. [27] used photons whose spatial extents were smaller than the channel length and thus could be fully emitted before any reflection came back to the node. To achieve this, they used a galvanically-connected Josephson junction-based tunable coupler capable

of large coupling and fast emission. With this approach, Zhong et al. [27] were able to achieve greater than 90% state transfer and Bell state fidelity. Leung et al. [26] took a different approach by hybridizing the multi-modal channel to high quality on-chip transmission line resonators. With this approach, they generated Bell state with fidelity of 79.3%. All realizations, however, have fidelities limited primarily by the loss in the communication channel [18, 24, 25, 26, 27, 28].

1.5 Summary and thesis outline

To address the loss in the communication channel, in this thesis, we introduce and demonstrate an alternative approach for state transfer: an adiabatic protocol, which can overcome channel loss by transferring the quantum state between the two remote qubits without ever populating the intermediate channel. We build on our prior work [27] and realize a two-node superconducting quantum communication system comprising two superconducting qubits coupled through a 0.73-m long on-chip transmission line via a pair of electrically-tunable couplers. Using this system, we deterministically generate entanglement between two remote superconducting qubits using the adiabatic protocol.

As the adiabatic protocol does not populate the intervening communication channel during the sequence, it protects against channel loss. We prove this claim by including in this system the capability to introduce large tunable loss to the channel, with which the single photon lifetime in the line can be controllably reduced from its intrinsic value by over two orders of magnitude. Using this capability, we explore the performance of the adiabatic protocol in the presence of significant channel loss. We show that the adiabatic protocol is more robust against channel loss than the alternative relay method, in which a quantum state is sequentially swapped to a channel mode and then to the second qubit. Furthermore, the system provides a unique platform to explore the performance of quantum communication protocols in the presence of significant, tunable dissipation.

The thesis is outlined as follows: In Chapter 2, we discuss the working principle behind the various superconducting quantum circuit elements. In particular, we will focus on the Xmon superconducting qubit: its working principle, control, and characterization. We will cover how we

realize high fidelity quantum control and projective single-shot readout of the qubit. In Chapter 3, we introduce a new type of active superconducting microwave element: a fast and broadband superconducting variable coupler, capable of routing and shaping quantum signals. This together with a resistive load will provide us with a tunable dissipation source for the channel in the quantum communication experiment in Chapter 4. Finally, we put all of these circuit elements together in Chapter 4 and present the main result of this thesis: generating entanglement between remote superconducting qubits via adiabatic passage using a tunably dissipative quantum communication system. In the concluding chapter, we summarize the main results of the thesis and discuss the outlook for this setup as well as the adaption of the adiabatic protocol for inter-chip remote entanglement generation.

CHAPTER 2

SUPERCONDUCTING QUANTUM CIRCUITS

Our quantum communication system consists of different superconducting quantum circuit components which must be operated at cryogenic temperatures $T \sim 10$ mK. The reasoning is two-fold. First, we need the metal (typically aluminum) to superconduct to achieve minimal loss. Thus, T must be lower than the critical temperature of aluminum, $T_C = 1.2$ K . Second, superconducting quantum circuit typically operates at GHz, corresponding to a single photon energy of hundreds of milliKelvin ($\sim$300 mK for a qubit at 6 GHz). Therefore, to operate the circuit in its quantum ground state and to avoid unwanted excitation into higher levels due to the thermal excitation from the environment, we need the thermal energy of the environment to be small, $T \ll \hbar\omega/k_B$. This allows us to freeze out the higher levels and operate the system in its two lowest energy states, and ground $|g\rangle$ and the excited states $|e\rangle$.

In our superconducting quantum communication system, we use a superconducting quantum bit (qubit) [29] at each node to prepare and measure the quantum state. A Josephson junction based tunable coupler is used to transfer the quantum state between nodes on-demand while the linking quantum channel is realized as a multi-modal on-chip transmission line. In this chapter, we go over the basic physics behind each circuit component starting from the quantization of the electrical harmonic oscillator, the LC resonator. We then describe the Xmon qubit, a weakly anharmonic oscillator. Finally, we describe how we can control and readout the qubit state using classical microwave pulses as well as coupling it to other quantum systems.

2.1 The quantized LC resonator

The most basic resonant electrical circuit is an LC resonant circuit shown in Fig. 2.1(a). The LC resonator is the electrical realization of a simple harmonic oscillator. We will prove this claim by deriving the system Hamiltonian. We begin by writing down the energy stored in the capacitor in

terms of the charge stored Q and its capacitance C,

$$U = \frac{Q^2}{2C}, \tag{2.1}$$

while the energy stored in the inductor of inductance L with current $I = \dot{Q}$ flowing through it is

$$T = \frac{LI^2}{2} = \frac{L\dot{Q}^2}{2}. \tag{2.2}$$

The Lagrangian is straightforward to write down,

$$\mathcal{L} = T - U = \frac{L\dot{Q}^2}{2} - \frac{Q^2}{2C}. \tag{2.3}$$

The conjugate coordinate to Q is the inductor flux Φ:

$$\Phi = \frac{d\mathcal{L}}{d\dot{Q}} = L\dot{Q}, \tag{2.4}$$

where $\Phi = LI$ is the flux through the inductor. To derive the Hamiltonian, we apply the Euler-Lagrange equation to the Lagrangian $\mathcal{L}$ and arrive at the Hamiltonian of the circuit,

$$H = \Phi\dot{Q} - \mathcal{L} = \frac{\Phi^2}{2L} + \frac{Q^2}{2C}. \tag{2.5}$$

Using canonical quantization, we promote the two conjugate coordinates Q and Φ to quantum operators obeying the familiar commutation relation:

$$[Q, \Phi] = i\hbar. \tag{2.6}$$

Defining the creation and annihilation operators in terms of the resonant frequency of the LC resonant circuit $\omega = 1/\sqrt{LC}$,

$$a = \sqrt{\frac{1}{2\hbar\omega L}}(\Phi + i\omega LQ), \tag{2.7}$$

$$a^\dagger = \sqrt{\frac{1}{2\hbar\omega L}}(\Phi - i\omega LQ), \tag{2.8}$$

$$[a, a^\dagger] = 1. \tag{2.9}$$

The flux and charge operators can be written in terms of these annihilation and creation operators,

$$Q = i\sqrt{\frac{\hbar}{2\omega}}(a^\dagger - a), \tag{2.10}$$

$$\Phi = \sqrt{\frac{\hbar\omega}{2}}(a^\dagger + a). \tag{2.11}$$

The Hamiltonian in Eq. 2.5 can be written as

$$H = \hbar\omega\left(a^\dagger a + \frac{1}{2}\right). \tag{2.12}$$

This corresponds to the familiar Hamiltonian of a simple harmonic oscillator with equally spaced energy levels separated by $\hbar\omega$ shown schematically in Fig. 2.1(b).

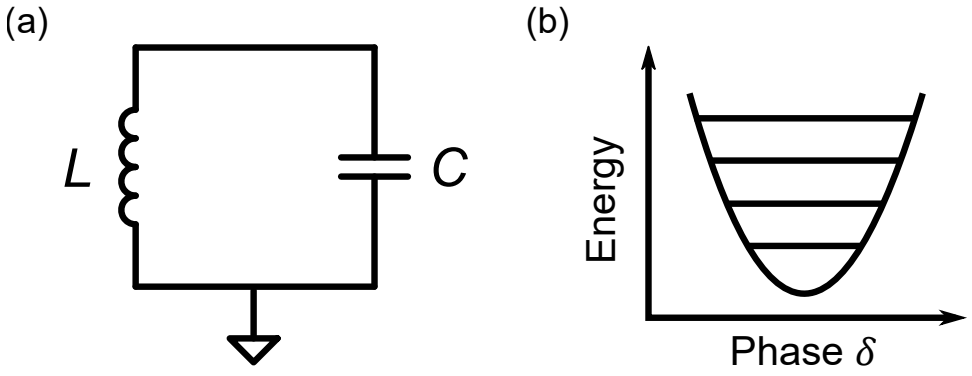

Figure 2.1: (a) Circuit schematic of a parallel LC resonant circuit. (b) The energy levels of the LC resonant circuit in (a). The harmonic potential results in evenly spaced energy levels separated by $\hbar\omega$.

In the above calculation, we have chosen the charge Q as the free parameter. It is often more convenient to choose node flux Φ, defined as the integral of voltage at a circuit node, as the free parameter[1]:

$$\Phi(t) = \int_{-\infty}^{t} V(t')dt'. \tag{2.13}$$

Repeating the equivalent calculation above for the node flux results in the same Hamiltonian as Eq. 2.12. We show this briefly here. The various terms of the Lagrangian written in terms of the node flux becomes

$$T = \frac{C\dot{\Phi}^2}{2}, \tag{2.14}$$

$$U = \frac{\Phi^2}{2L}, \tag{2.15}$$

$$\mathcal{L} = T - U = \frac{C\dot{\Phi}^2}{2} - \frac{\Phi^2}{2L}. \tag{2.16}$$

The conjugate of the node flux is the charge Q:[2]

$$Q = \frac{d\mathcal{L}}{d\dot{\Phi}} = C\dot{\Phi}. \tag{2.17}$$

Again, we promote the two conjugate coordinates to quantum operators obeying the commutation relation:

$$[\Phi, Q] = i\hbar. \tag{2.18}$$

1. Unfortunately, there is a collision of notation between the node flux defined here and the previously defined inductor flux in Eq. 2.4.

2. There is a minor caveat here. Using the node flux Φ as the free parameter, the definition of charge Q here differs from previous definition in Eq. 2.1 by a sign.

The annihilation and creation operators are then defined as

$$a = \sqrt{\frac{1}{2\hbar\omega C}}(Q + i\omega C\Phi), \tag{2.19}$$

$$a^\dagger = \sqrt{\frac{1}{2\hbar\omega C}}(Q - i\omega C\Phi), \tag{2.20}$$

$$[a, a^\dagger] = 1. \tag{2.21}$$

The flux and charge operators can be written in terms of these annihilation and creation operators,

$$\Phi = \sqrt{\frac{\hbar L\omega}{2}}(a + a^\dagger), \tag{2.22}$$

$$Q = -i\sqrt{\frac{\hbar C\omega}{2}}(a - a^\dagger). \tag{2.23}$$

Following the Euler-Lagrange equation, we arrive at the Hamiltonian of a simple harmonic oscillator like before.

$$H = Q\dot{\Phi} - \mathcal{L} \tag{2.24}$$

$$= \frac{\Phi^2}{2L} + \frac{Q^2}{2C} \tag{2.25}$$

$$= \hbar\omega(a^\dagger a + \frac{1}{2}). \tag{2.26}$$

2.2 Transmission line resonators

In superconducting circuits, one of the simplest ways to realize high quality LC resonators on-chip is to use segments of transmission line. By engineering their boundary conditions and lengths, their resonant frequency ω_0 and coupling strength g, defined as rate of coherent exchange with other quantum systems, can be carefully engineered. In a superconducting quantum circuit, they can be used as long-lived quantum memory, as a quantum bus that mediates the interaction between quantum bits as in this thesis, and as intermediary between the qubit and the environment through the Purcell effect.

Short-circuited quarter-wave resonator

Here we focus on one such type of resonator, the short-circuited quarter-wave resonator, following Ref. [30]. Consider a transmission line with loss constant α, propagation constant β, characteristic impedance Z_0, and length ℓ. The input impedance of such a line is

$$Z_{\text{in}} = Z_0 \tanh(\alpha + i\beta)\ell \tag{2.27}$$

$$= Z_0 \frac{1 - i\tanh(\alpha\ell)\cot(\beta\ell)}{\tanh(\alpha\ell) - i\cot(\beta\ell)}. \tag{2.28}$$

In the low loss limit, where $\alpha\ell \ll 1$, we can approximate $\tanh(\alpha\ell) \approx \alpha\ell$. Close to the resonant frequency ω_0, the length of the lines equals to a fourth of the wavelength $\ell = \lambda/4$, we then have

$$\beta\ell = \frac{\pi}{2} + \frac{\pi\Delta\omega}{2\omega_0}, \tag{2.29}$$

where $\Delta\omega = \omega - \omega_0$. We then have

$$\cot\beta\ell = \cot\left(\frac{\pi}{2} + \frac{\pi\Delta\omega}{\omega_0}\right) \approx \frac{-\pi\Delta\omega}{2\omega_0}. \tag{2.30}$$

Substituting this result into Eq. 2.28,

$$Z_{\text{in}} = Z_0 \frac{1 + i\alpha\ell\Delta\omega/2\omega_0}{\alpha\ell + i\pi\Delta\omega/2\omega_0} \approx \frac{Z_0}{\alpha\ell + i\pi\Delta\omega/2\omega_0}. \tag{2.31}$$

Matching this equation to the impedance of a parallel RLC circuit, we get

$$C = \frac{\pi}{4\omega_0 Z_0}, \tag{2.32}$$

$$L = \frac{1}{\omega_0^2 C}, \tag{2.33}$$

$$R = \frac{Z_0}{\alpha\ell}. \tag{2.34}$$

Thus, around its resonance, a short-circuited quarter-wave resonator is equivalent to a parallel RLC resonator with equivalent capacitance, inductance, and resistance as above.

Below we show cryogenic measurement of several short-circuited quarter-wave resonators measured in the "hanger" configuration. In this configuration, the resonators are coupled to a common measurement waveguide which can be probed in transmission.

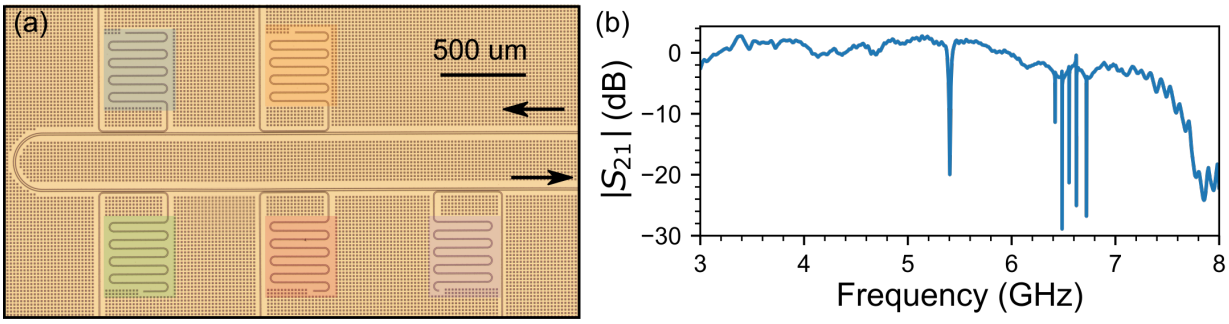

Figure 2.2: Quarter-wave transmission line resonators. (a) Optical micrograph of five short-circuited quarter-wave transmission line resonators coupled to the common measurement waveguide in the hanger configuration. (b) Wide frequency transmission measurements measured at 10 mK. The five transmission line resonators' resonances can be seen as dips in transmission. The overall transmission level is offset by an arbitrary amount from attenuators in the input lines and the amplifiers in the output lines. The 7.5 GHz cutoff is attributed to the operating frequency range of the cryogenic high electron mobility transistor amplifier (HEMT) used at 4K. Ripples in transmission are likely due to slight impedance mismatch between coaxial connections.

In this measurement configuration, whenever we are probing frequency at the resonant frequency of one of the five resonators, we observe a dip in transmission. We can study all five resonances individually. Fig. 2.3(a,b) is an example of the typical dip in transmission and flipping of the phase of the resonator measured. Here, the transmission magnitude is normalized to 0 dB far off-resonant, $|\tilde{S}_{21}|$, and a linear offset is subtracted from the transmission phase, $\angle\tilde{S}_{21}$. We can also plot inverse of the normalized transmission $1/\tilde{S}_{21}$ in the complex plane in Fig. 2.3(c). Following [31], we fit to this circle and obtain the two quality factors Q_i and Q_c using the following expression:

$$\frac{1}{\tilde{S}_{21}} = 1 + \frac{Q_i}{Q_c} e^{i\phi} \frac{1}{1 + 2iQ_i\Delta\omega}. \tag{2.35}$$

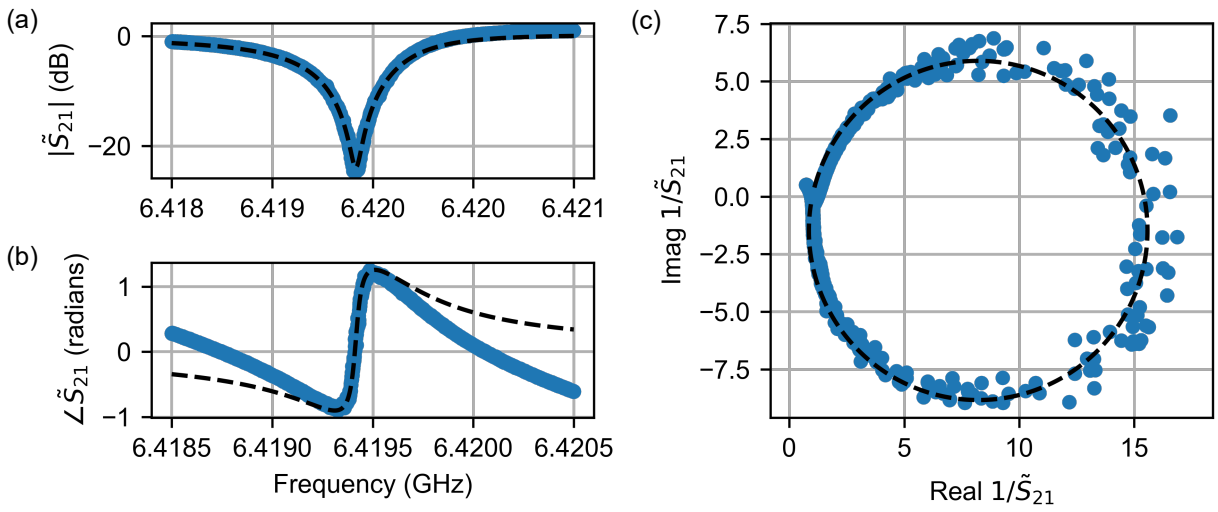

Figure 2.3: (a) Normalized transmission magnitude $|\tilde{S}_{21}|$ and (b) phase $\angle\tilde{S}_{21}$ of one of the resonators. (c) The inverse of the same normalized transmission data $1/\tilde{S}_{21}$ is also plotted in the complex plane and fitted to a circle using Eq. 2.35. From the fit, we obtain the resonant frequency $f_r = 6.419$ GHz, the internal quality factor $Q_i = 1.283 \times 10^5$, and the coupling quality factor $Q_c = 8.71 \times 10^3$. The data is measured at around -135 dBm of input power at the sample corresponding to ~ 1 photon level in the resonator [32].

The internal quality factor Q_i relates to the intrinsic loss in the resonator while the coupling quality factor Q_c relates to how strongly the resonator couples to the measurement waveguide. We can repeat this measurement as a function of input power, equivalently the number of photons in the resonator. The most important aspect of this measurement is the low power internal quality factor which corresponds to the single photon lifetime of the resonator, T_{1r}, as we typically operate our quantum circuit at the single photon level. We observe a low power Q_i of 10^5 which corresponds to a $T_1 \approx 3$ μs at 6 GHz, sufficient for what we plan to do here.

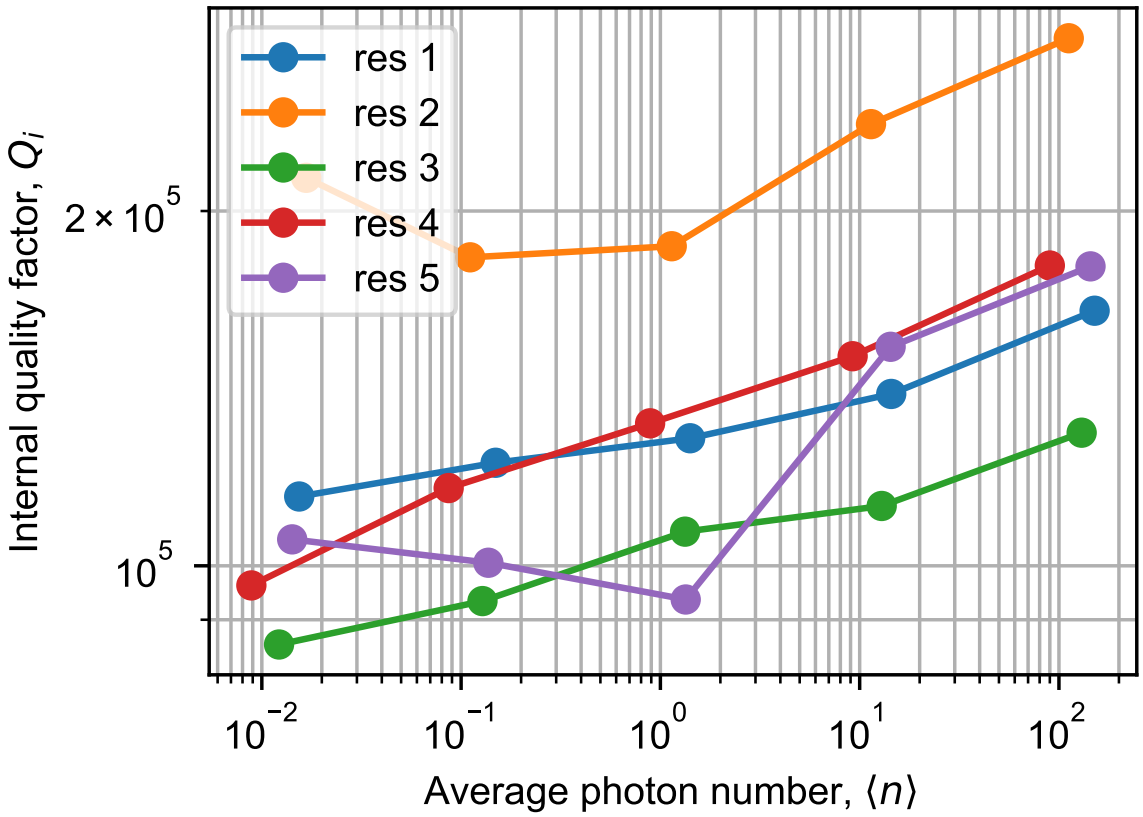

Figure 2.4: Power dependence of the internal quality factor Q_i of the resonators, obtained from fits to Eq. 2.35. For the horizontal axis, we have converted the input power at the sample to an estimated average photon number in the resonator following Ref. [32].

2.3 Josephson junctions

As shown in Fig. 2.1(a), the harmonic potential of the LC resonant circuit results in energy levels evenly spaced in energy by $\hbar/\sqrt{LC}$. Such energy levels cannot be used as a quantum bit as no transition is individually addressable. In order to construct a quantum bit, we need to add a nonlinear element into the circuit. This is provided by the Josephson junction [33, 34].

As shown in Fig. 2.5(a), a Josephson tunnel junction consists of a thin insulating barrier ($\sim$ nm thick) sandwiched between two superconductor metal electrodes. The thin insulating layer allows the superconducting phase ϕ_L and ϕ_R of the electrodes to differ. The Ginzburg-Landau order parameter of the superconducting condensate of each electrode can be written in terms of its phase ϕ and Cooper pair density n [35] as $\psi(r) = \sqrt{n}e^{i\phi(r)}$. This is depicted schematically in Fig. 2.5(a) and a scanning electron microscope picture of an actual Josephson junction from the device in this thesis is shown in Fig. 2.5(b). In our lab, Josephson junctions are fabricated by evaporation through a shadow mask using the Dolan bridge technique [36].

The current through the junction I and the voltage across the junction V is related to the phase difference across the junction $\delta = \phi_L - \phi_R$ by the Josephson relations [33]:

$$I(t) = I_c \sin\delta, \tag{2.36}$$

$$V(t) = \frac{\Phi_0}{2\pi}\frac{d\delta}{dt}, \tag{2.37}$$

where I_c is the critical current of the junction and Φ_0 is the magnetic flux quantum ($= h/2e = 2 \times 10^{-15}$ Wb). It is generally more convenient to describe the Josephson junction in terms of flux Φ. Using our previous definition of node flux Eq. 2.13, we integrate the voltage expression in Eq. 2.37 and find the following relation between the phase ϕ and the flux Φ:

$$\Phi(t) = \int_{-\infty}^{t} V(t')dt' = \int_{-\infty}^{t} \frac{\Phi_0}{2\pi}\frac{d\delta}{dt}dt' = \frac{\Phi_0}{2\pi}\delta, \tag{2.38}$$

$$\Rightarrow \delta = \frac{2\pi\Phi}{\Phi_0}. \tag{2.39}$$

2.3.1 Junction inductance

The key role of the Josephson junction is that we can use it as a *lossless nonlinear inductor* with inductance L_J. We show this below. For an inductor, its inductance is related to the voltage and rate of change of current in time by $V = L(dI/dt)$. We thus differentiate Eq. 2.36 with respect to time and arrive at the following expression for the inductance of the junction [37, 38]:

$$L_J = \frac{V}{dI/dt} = \frac{\Phi_0}{2\pi}\frac{1}{I_c \cos\delta}, \tag{2.40}$$

where we have used Eq. 2.37 for the substitution of $d\delta/dt$ in the last equal sign.

From Eq. 2.40, we see that the Josephson junction acts as a nonlinear inductor whose effective inductance depends on phase difference δ. This is the key source of nonlinearity for our qubit, which we will introduce later on in the chapter. To find the energy stored in the junction, we integrate the product of the current and voltage:

$$U = \int I(t')V(t')dt' = \int I_c \sin\delta \left(\frac{\Phi_0}{2\pi}\right)\left(\frac{d\delta}{dt'}\right)dt' \tag{2.41}$$

$$= \frac{\Phi_0 I_c}{2\pi} \tag{2.42}$$

$$= -E_J \cos\delta, \tag{2.43}$$

where $E_J = \Phi_0 I_c/2\pi$ is the Josephson energy of the Josephson junction.

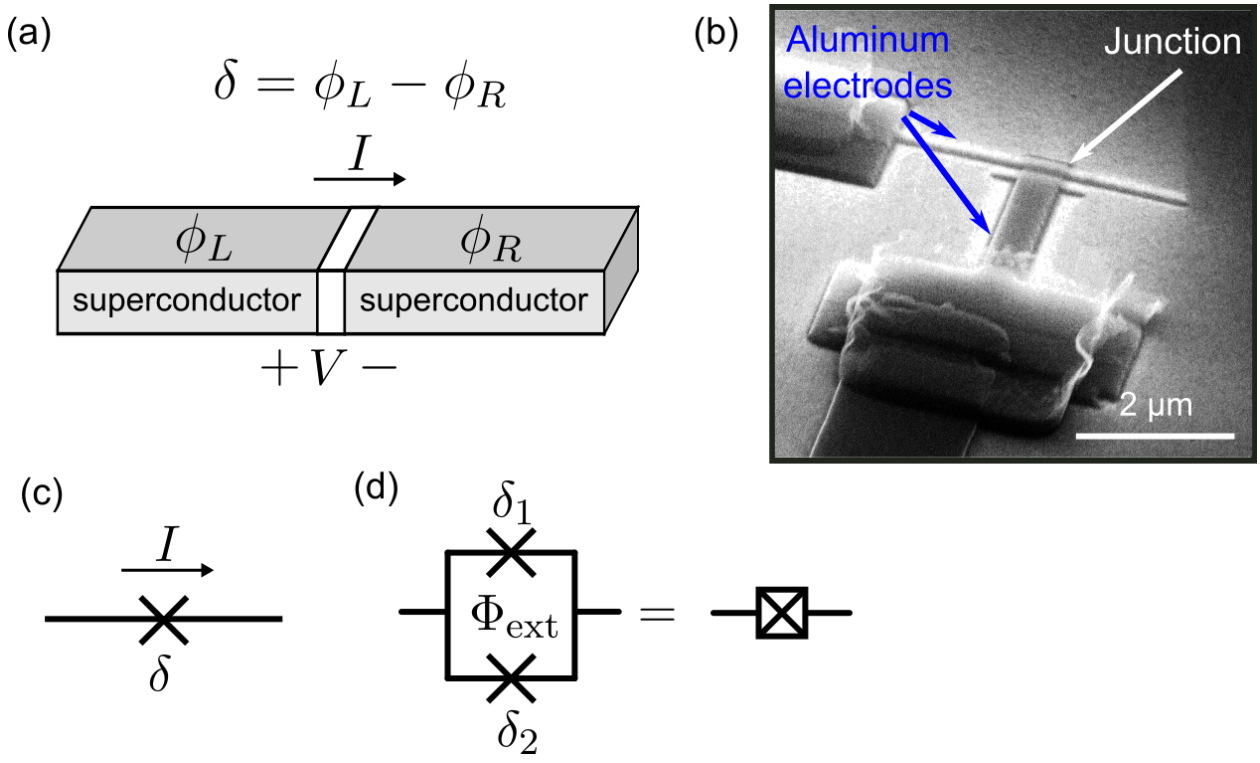

Figure 2.5: Josephson junctions. (a) Schematic of a Josephson tunnel junction with a thin insulating layer (white) sandwiched between two superconductors (grey). The Ginzburg-Landau order parameter of the superconducting condensate of the left and right superconducting electrodes $\psi(r) = \sqrt{n_i}e^{i\phi_i}$ differs by $\delta = \phi_L - \phi_R$. (b) Scanning electron micrograph of a fabricated Josephson tunnel junction formed by two overlapping aluminum electrodes (blue arrows). The junction is formed as a thin layer of aluminum oxide at the overlapping region (white arrow). (c) The Josephson junction is typically represented as an "X" in the circuit. (d) Connecting two symmetric junctions in parallel forms a superconducting quantum interference device (SQUID) with phase δ_1 and δ_2 across each junction. The SQUID is typically represented as a square with a cross in the middle in the circuit.

2.3.2 SQUID

A DC superconducting quantum interference device (SQUID) consists of two Josephson junctions connected in parallel. It is typically used in place of a single Josephson junction in a superconducting qubit to enable frequency tunability. By controlling the external flux Φ_{ext} through the superconducting loop, its inductance can be tuned; see Fig.2.5(d).[3] Consider two Josephson junctions in parallel as in Fig. 2.5(d), with phase δ_1 and δ_2 across each junction, the energy stored in the two junctions are:

$$U = -E_{J1}\cos\delta_1 - E_{J2}\cos\delta_2, \tag{2.44}$$

where E_{Ji} is the Josephson energy of each junction.

For simplicity, we consider a symmetric SQUID and set $E_{J1} = E_{J2}$. We can then rewrite the total energy stored in the two junctions as

$$U = -2E_J\cos\left(\frac{\delta_1 - \delta_2}{2}\right)\cos\left(\frac{\delta_1 + \delta_2}{2}\right). \tag{2.45}$$

Using flux quantization, we obtain the following relation between the phase difference of the two junctions $\delta_1 - \delta_2$ and the external flux Φ_{ext} [39],

$$\delta_1 - \delta_2 = 2\pi\left(\frac{\Phi_{\text{ext}}}{\Phi_0} + m\right), \tag{2.46}$$

where Φ_0 is the magnetic flux quanta and m is an integer. Substituting Eq. 2.46 into Eq. 2.45, we get

$$U = -2E_J\left|\cos\left(\frac{\pi\Phi_{\text{ext}}}{\Phi_0}\right)\right|\cos\left(\frac{\delta_1 + \delta_2}{2}\right). \tag{2.47}$$

Thus by controlling the external magnetic flux through the superconducting loop Φ_{ext}, we can change the energy stored in the SQUID, U, and equivalently its effective inductance. In the context of superconducting circuits, SQUID provides a flux tunable non-linear inductor to our toolbox. As

3. We note that we have ignored the geometric inductance of the SQUID loop here.

we will see later in this chapter, incorporation of SQUID in the qubit circuit enables frequency tunability of the qubit [40] and thus control over the Z axis of the qubit state.

2.4 Superconducting qubit

If we exchange the linear inductor in our original parallel LC circuit in Fig .2.1(a) with a Josephson junction as shown in Fig. 2.6(a), we can replace the second term in the Hamiltonian of the LC circuit with the energy stored in the junction Eq. 2.43,

$$U = -E_J \cos\delta. \tag{2.48}$$

The consequence of this is shown in Fig. 2.6(b), where the original quadratic potential becomes a cosine. Inserting this into the original Hamiltonian of the LC resonator, we arrive at the Hamiltonian of our superconducting qubit circuit,

$$H = \frac{Q^2}{2C} - E_J \cos\delta. \tag{2.49}$$

When the circuit superconducts, electrons in the circuit pair up and form Cooper pairs [39]. As bosons,the Cooper pairs all condense into the quantum ground state when cooled, allowing us to describe the circuit with a single macroscopic quantum state [35]. We can rewrite the Hamiltonian in terms of number of Cooper pairs $n = Q/2e$ and the charging energy of the cooper pair $E_C = e^2/2C$ as

$$H = 4E_C n^2 - E_J \cos\delta, \tag{2.50}$$

where δ and n satisfy the commutation relation $[\delta, n] = 1$. The two variables here δ and n are analogous to the position and momentum of a simple harmonic oscillator.

Using this model, we can visualize the eigenenergies within the cosine potential shown in Fig. 2.6(b). Significantly, the energy levels are unequally spaced. This allows us to selectively address a single transition. For example, we can selectively address the transition between the

ground state $|g\rangle$ and the first excited state $|e\rangle$, without addressing transitions between higher levels. While there exists many more levels above $|e\rangle$, in this work we only use the lowest two energy states as our qubit and will focus our discussion on them.

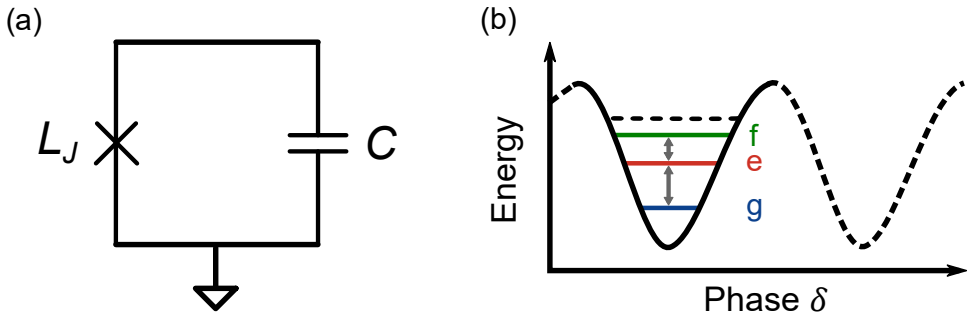

Figure 2.6: (a) Circuit schematic of a superconducting qubit. Replacing the linear inductor of the parallel LC resonant circuit with a Josephson junction introduces nonlinearity. (b) Such nonlinearity leads to an anharmonic cosine potential with unequally spaced energy levels, suitable to be used as a qubit.

The Xmon qubit

There is a wide variety of superconducting qubits. In this thesis, we use the Xmon qubit [41, 42] which is a specific realization of the transmon qubit first developed at Yale [40, 37] and one of the widely used superconducting qubit implementations. The Xmon qubit is easy to control and readout and can be readily implemented on a 2D circuit with high coherence [40, 41]. In Fig 2.7(b), we show an optical micrograph of what an Xmon qubit looks like with a corresponding circuit model shown in Fig 2.7(a). The shunting capacitor is realized as a cross-shaped open-circuited coplanar waveguide, forming a low loss capacitance C to ground. The capacitance is in parallel with a SQUID, consisting of two Josephson junctions in parallel, with inductance L_J connecting to ground at the bottom of the capacitor. A magnified view of the SQUID loop is shown inset. The use of a SQUID loop affords tuning of the frequency of the qubit by controlling the magnetic flux threaded through the SQUID [40, 41]. The readout circuit is on top and partially shown. Typical

values for C and L_J for our qubits are

$$C \approx 90 \text{ fF}, \tag{2.51}$$

$$L_J \approx 7 \text{ nH}, \tag{2.52}$$

$$E_C \approx 230 \text{ MHz}, \tag{2.53}$$

$$E_J \approx 20 \text{ GHz}, \tag{2.54}$$

$$\omega_{ge}/2\pi \approx 5.5 \text{ GHz}, \tag{2.55}$$

$$\eta/2\pi = -E_C \approx -230 \text{ MHz}, \tag{2.56}$$

$$Z_0 = \sqrt{L_J/C} \approx 300\ \Omega. \tag{2.57}$$

The Xmon qubit achieves long coherence time by operating in the regime where $E_J \gg E_C$, resulting in energy levels that are largely independent of the DC offset charge n_g. Fluctuations in n_g can translate to shifts in frequency resulting in dephasing. In the Xmon regime $E_C \gg E_J$, δ is confined to small perturbations around zero and we can Taylor-expand the potential term in the Hamiltonian in Eq. 2.50 to fourth order in δ:

$$-E_J \cos\delta \approx -E_J + \frac{E_J\delta^2}{2} - \frac{E_J\delta^4}{24}. \tag{2.58}$$

We can rewrite the Hamiltonian as

$$H = 4E_C n^2 + \frac{E_J\delta^2}{2} - E_J - \frac{E_J\delta^4}{24}. \tag{2.59}$$

We can thus view the Xmon as a simple harmonic oscillator perturbed by a fourth order potential. Defining the creation and annihilation operators in terms of the charging energy E_C and the

Josephson energy E_J,

$$a = \left(\frac{1}{8E_C E_J}\right)^{1/4} \left(2\sqrt{E_C}n + i\sqrt{\frac{E_J}{2}}\delta\right), \tag{2.60}$$

$$a^\dagger = \left(\frac{1}{8E_C E_J}\right)^{1/4} \left(2\sqrt{E_C}n - i\sqrt{\frac{E_J}{2}}\delta\right). \tag{2.61}$$

We can then quantize the Xmon Hamiltonian using these creation and annihilation operators,

$$\delta = \left(\frac{2E_C}{E_J}\right)^{1/4} (a + a^\dagger), \tag{2.62}$$

$$n = -i\left(\frac{E_J}{8E_C}\right)^{1/4} \frac{1}{\sqrt{2}}(a - a^\dagger). \tag{2.63}$$

We can rewrite the quantized Hamiltonian as

$$H = -E_J + \sqrt{8E_C E_J}(a^\dagger a + \frac{1}{2}) - \frac{E_C}{12}(a - a^\dagger)^4. \tag{2.64}$$

Applying first order correction with perturbation theory to the above Hamiltonian gives us the following eigenvalues [40]:

$$E_m \approx -E_J + \sqrt{8E_C E_J}(m + 1/2) - \frac{E_C}{12}(6m^2 + 6m + 3). \tag{2.65}$$

associated with the eigenstate $|m\rangle$. The two lowest energy states can be used as a qubit. Defining the transition energy between state $|i\rangle$ and $|j\rangle$ as $E_{ij} = E_j - E_i$, the energy difference of such a qubit is

$$E_{ge} = E_{01} = E_1 - E_0 = \sqrt{8E_J E_C} - E_C. \tag{2.66}$$

The anharmonicity of the lowest two states used as the qubit is defined as $\eta = \omega_{12} - \omega_{01} = \omega_{ef} - \omega_{ge}$. Combining this with Eq. 2.65 yields

$$\eta = \omega_{12} - \omega_{01} = (E_{ef} - E_{ge})/\hbar = -E_C/\hbar. \tag{2.67}$$

Thus, the larger the charging energy E_C, the more anharmonic the qubit is and the qubit is less likely to populate higher energy levels during state manipulation. The anharmonicity also sets a limit on the speed in which a qubit can be controlled, as fast pulses are spectrally broad and can exceed η, inducing leakage to the $|f\rangle$ state. The anharmonicity of our qubit is $\eta \approx -2\pi \times 200$ MHz. Considering only the primary non-computational level [4], we can describe the Xmon qubit as a weakly anharmonic oscillator with three energy levels,

$$H/\hbar = (\omega + \eta)a^\dagger a + \frac{\eta}{2}a^\dagger a^\dagger aa. \tag{2.68}$$

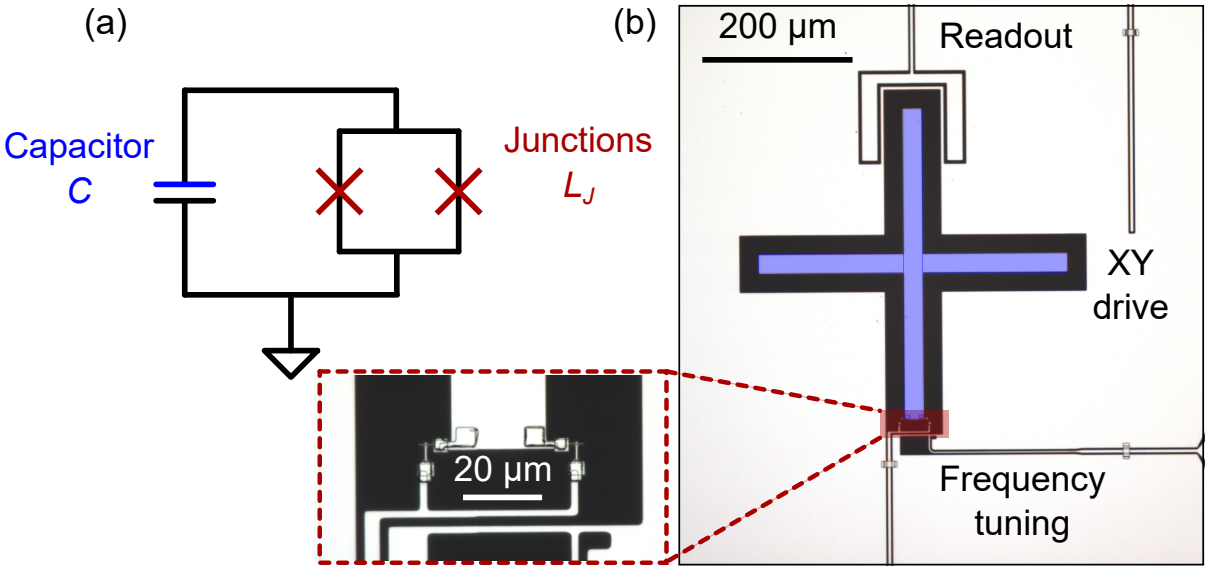

Figure 2.7: The Xmon qubit. (a) Circuit schematic of our Xmon qubit. We exchange the inductor of the parallel LC resonator with a pair of Josephson junctions in parallel forming a SQUID (red). This allows us to tune the qubit frequency by applying an external flux. (b) Optical micrograph of the Xmon qubit. The light areas are aluminum and the dark areas are the exposed sapphire substrate. The Xmon qubit consists of a cross-shaped shunting capacitor (blue) with a SQUID loop (red) connected at the bottom of the cross to ground. The drive (XY control) line is capacitively coupled to the right of the cross while the flux bias (Z control) line is inductively coupled to the SQUID loop at the bottom of the cross. The top of the cross is capacitively coupled to a half-wave resonator (not shown) for readout. (Inset) Magnified view of the SQUID loop with its flux bias line.

4. This simplification is justified by the sufficient anharmonicity of the Xmon qubit. In reality, the Xmon qubit has an infinite number of energy levels, not just three.

2.5 Superconducting qubit control

As shown in Fig. 2.7(b), there are several elements around the superconducting qubits to control and read out the quantum states of the qubit. We will first focus on the control lines used to manipulate the quantum state of the qubit. As shown in Fig. 2.7(b), the Xmon qubit is controlled by a drive line for XY control and a flux bias line for Z control.

2.5.1 XY drive

We can prepare any quantum states on the Bloch sphere on the qubit by sending in resonant microwave pulses. To do so, we pattern an XY drive line that is capacitively coupled to the Xmon; see Fig. 2.7(b). By applying a microwave drive at the qubit frequency to the XY drive line, we can resonantly excite the qubit and drive Rabi oscillation on the Bloch sphere. This corresponds to a rotation around the X(Y) or any other axes on the equator of the Bloch sphere depending on the phase of the microwave drive.

Consider the drive circuit in Fig. 2.8(a) where a voltage source with impedance Z_0 delivers a voltage drive signal V_{XY} to the qubit via the XY drive line,

$$\begin{aligned} V_{XY}(t) &= E(t)\sin(\omega_{XY}t + \phi_{XY}) \\ &= E(t)[I\sin(\omega_{XY}t) + Q\cos(\omega_{XY}t)], \end{aligned} \tag{2.69}$$

where $E(t)$ is the slowly-varying envelope of the signal at frequency ω_{XY} and I and Q are the in-phase and quadrature component of the drive signal V_{XY}, respectively. When the driving frequency is on resonant with the qubit frequency $\omega_{XY} = \omega_{ge} = E_{ge}/\hbar$, we can write down the drive Hamiltonian as [43]:

$$H_{XY} = -\frac{E(t)}{2}\left(\frac{V_0 Q_{ZPF}}{1 - C_c/C}\right)(I\sigma_x + Q\sigma_y), \tag{2.70}$$

where Q_{ZPF} is the zero-point fluctuation of the charge and is defined by the circuit impedance Z_{LC} as $Q_{ZPF} = \sqrt{\hbar/Z_{LC}}$ [43] and σ_x and σ_y are the Pauli operators for the qubit. The Pauli

operators are a set of 2×2 complex matrices as defined by:

$$\sigma_x = \begin{bmatrix} 0 & 1 \\ 1 & 0 \end{bmatrix}, \ \sigma_y = \begin{bmatrix} 0 & -i \\ i & 0 \end{bmatrix}, \ \sigma_z = \begin{bmatrix} 1 & 0 \\ 0 & -1 \end{bmatrix}. \tag{2.71}$$

The Pauli operators are unitary and Hermitian. They obey the cyclic commutation relation with the Levi-Civita symbol ϵ_{ijk},

$$[\sigma_i, \sigma_j] = 2i\epsilon_{ijk}\sigma_k. \tag{2.72}$$

The time evolution operator $U(t)$ is thus

$$U(t) = \text{Exp}\left[\frac{i}{2\hbar}\left(\frac{V_0 Q_{ZPF}}{1 - C_c/C}\right)[I\sigma_x + Q\sigma_y]\int E(t)dt\right]. \tag{2.73}$$

The driving signal can be set such that $I = 1$ and $Q = 0$ and the envelope function $E(t)$ and the driving duration T can be chosen such that

$$\frac{i}{2\hbar}\left(\frac{V_0 Q_{zpf}}{1 - C_c/C}\right)\int_0^T E(t)dt = \frac{\pi}{2}. \tag{2.74}$$

Then the time evolution operator becomes

$$U(T) = \text{Exp}\left(\frac{i\pi\sigma_x}{2}\right) = i\sigma_x. \tag{2.75}$$

This corresponds to a π-rotation along the X axis of the Bloch sphere. From Eq. 2.70, we see that by changing the phase of the drive, we can rotate around any axis on the equator of the Bloch sphere.

Rabi oscillation

The first experiment to calibrate the XY drive is to carry out a Rabi oscillation sequence. Applying an on-resonant microwave drive at the qubit frequency $\omega_{ge}/2\pi$ to the XY control line causes the

qubit to oscillate between the ground state $|g\rangle$ and the exited state $|e\rangle$. This is displayed schematically in Fig. 2.8(b). In Fig 2.8(c), we plot the measured excited state population as a function of the drive time. We begin in ground state $|g\rangle$ and go to the excited state $|e\rangle$. Driving the qubit further causes the qubit to return to the ground state, completing a full cycle. From this measurement, we obtain the drive lengths for the π and $\pi/2$ pulses on the qubit. The drive duration represented by the red dashed line Fig. 2.8(c) corresponds to the drive length to realize a π pulse on a qubit, which swaps the excitation between the $|g\rangle$ and $|e\rangle$ state. Equivalently, the orange dashed line corresponds to the drive length for a $\pi/2$ pulse on the qubit, which maps the ground state $|g\rangle$ to an equal superposition state $|e\rangle + i|g\rangle$.

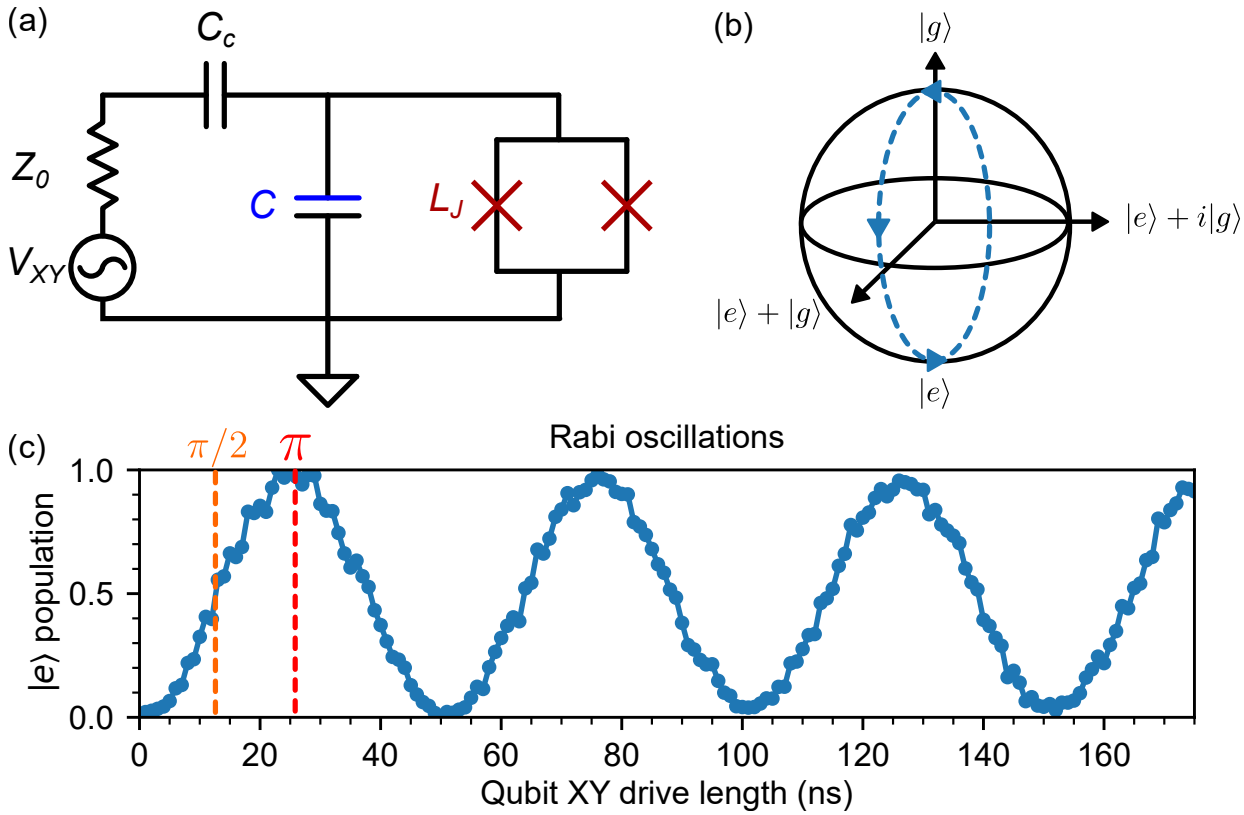

Figure 2.8: (a) Circuit schematic of qubit under a voltage drive V_{XY} . (b) Schematic of a qubit under drive on the Bloch sphere as it evolves between the ground and the excited state. (c) Measured Rabi oscillations. Orange and red vertical dashed lines mark the XY drive lengths for the $\pi/2$ and π pulses respectively.

2.5.2 *Z flux bias*

The XY line only allows for control over two axes of the Bloch sphere. We can introduce another control line, the Z flux bias line, for control over the Z axis. The Z flux bias line is a shorted coplanar waveguide that is inductively coupled to the SQUID loop of the qubit; see Fig. 2.7(b). Flux biasing the line inductively induces a magnetic flux threaded through the qubit SQUID Φ_{ext}, changing its effective inductance L_J and thus tuning the transition frequency of the qubit $\omega_{ge}/2\pi$. Equivalently, this corresponds to an effective rotation around the Z axis of the Bloch sphere in the frame of the qubit. This is because if the frequency of the qubit is changed with respect to its initial frame, the state of the qubit evolves either slower or faster than its initial frame and acquires a phase ϕ around the Z axes of the Bloch sphere.

From Eq. 2.47, the energy stored in a symmetric SQUID loop is

$$U = -2E_J \left|\cos\left(\frac{\pi\Phi_{\text{ext}}}{\Phi_0}\right)\right| \cos\left(\frac{\delta_1+\delta_2}{2}\right). \tag{2.76}$$

From this expression, we see that the SQUID acts as a Josephson junction whose energy has a cosine dependence on the external flux Φ_{ext}. We substitute the above expression into the expression of the transition frequency of the qubit (Eq. 2.66) and get

$$E_{eg} = \sqrt{8E_C E_J \left|\cos\left(\frac{\pi\Phi_{\text{ext}}}{\Phi_0}\right)\right|} - E_C. \tag{2.77}$$

Thus, the transition frequency of the Xmon $\omega_{ge}/2\pi$ can be tuned by the flux biasing the Z control line with a period of one flux quanta Φ_0. This also allows us to rotate the qubit around the Z axis of the Bloch sphere, corresponding to a qubit phase ϕ rotation. As all single qubit gates can be decomposed into X, Y, and Z rotations on the Bloch sphere, with the XY drive line and the Z flux bias line, we have control over all three axes of the Bloch sphere.

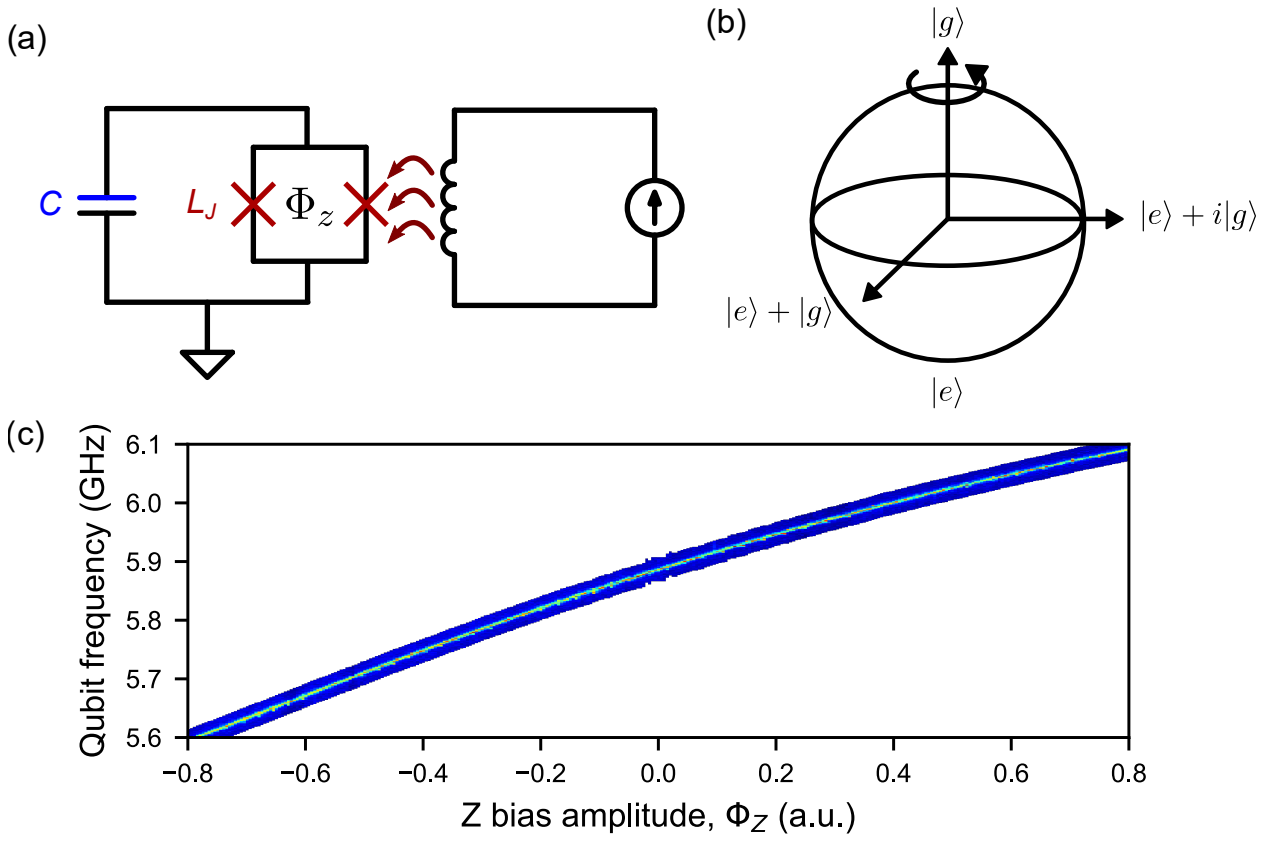

Figure 2.9: Qubit frequency tuning. (a) Circuit schematic of flux tuning circuit of the qubit. (b) Biasing the SQUID tunes the effective frequency of the qubit. The qubit rotates and accumulates a phase ϕ relative to its initial frame, corresponding to an effective rotation around the Z axis of the Bloch sphere (c) Measured qubit frequency as a function of Z flux bias (arbitrary unit).

2.6 Superconducting qubit readout

To read out the state of the qubit, we use a dispersive readout technique and place a linear resonator (readout resonator, realized as a coplanar waveguide resonator) between the qubit and the measurement circuit [44, 45]. At one end, the linear resonator is coupled to the qubit and at the other end, it is coupled to the measurement waveguide. The resonator and the qubit are detuned and operate in the non-resonant dispersive coupling regime. We probe the resonator and the qubit it is coupled to by sending in a microwave tone through the measurement waveguide which reflects on the resonator and measuring the transmitted amplitude and phase of the output signal. The amplitude and phase of the probe tone allows us to see if the qubit is in the ground or excited state. If the qubit changes state, its inductance changes, shifting the resonant frequency of the readout resonator it is coupled to. Thus, by measuring the resonant frequency of the readout resonator, we can determine the state of the qubit.

2.6.1 Dispersively coupled resonator and qubit

We treat this formally by considering the circuit of a qubit coupled to a linear LC resonator in Fig. 2.10(a). We use the Jaynes-Cummings model to write down the coupled qubit-resonator Hamiltonian [46, 47, 37] in terms of the creation and annihilation operators: a and $a^\dagger$ for the resonator and σ_+ and σ_- for the qubit.

$$H_{JCM} = \hbar\omega_r a^\dagger a - \frac{\hbar\omega_q\sigma_z}{2} - \hbar g(\sigma_- - \sigma_+)(a - a^\dagger) \tag{2.78}$$

$$= \hbar\omega_r a^\dagger a - \frac{\hbar\omega_q\sigma_z}{2} + \hbar g(-\sigma_- a + \sigma_- a^\dagger + \sigma_+ a - \sigma_+ a^\dagger), \tag{2.79}$$

where ω_r and ω_q are the resonances of the readout resonator and the qubit respectively and g is the coupling constant between the two systems. Using the rotating wave approximation, we eliminate terms that do not conserve the total number of excitations (i.e. $\sigma_- a$ and $\sigma_+ a^\dagger$ terms). This is because these terms are non-resonant and rapidly oscillating; in the timescale of the experiment,

they quickly average out to zero.[5]. Doing so, we arrive at

$$H_{JCM} = \hbar\omega_r a^\dagger a - \frac{\hbar\omega_q}{2}\sigma_z + \hbar g(\sigma_+ a + \sigma_- a^\dagger), \tag{2.80}$$

where σ_z is the Pauli Z operator of the qubit. Let $\Delta = \omega_q - \omega_r$ be the detuning between the qubit and the readout resonator. For $|\Delta| \gg g$, we can apply the dispersive approximation to the Hamiltonian,

$$H_{JCM} = \hbar\omega_r n - \frac{\hbar\omega_q}{2}\sigma_z - \frac{\hbar g^2}{\Delta}\sigma_z n, \tag{2.81}$$

where $n = a^\dagger a$ is the photon number of the readout resonator. Using this result, the above Hamiltonian can be rewritten as

$$H_{JCM} = \hbar(\omega_r + \chi\sigma_z)n - \frac{\hbar\omega_q}{2}\sigma_z, \tag{2.82}$$

where $\chi = -g^2/\Delta$ is the dispersive shift. If we consider the third level of the qubit $|f\rangle$, the expression of dispersive shift is slightly modified [40],

$$\chi = -\frac{g^2}{\Delta}\frac{1}{1+\Delta/\eta} \approx -\frac{g^2}{\Delta^2}\eta, \tag{2.83}$$

where η is the anharmonicity of the qubit.

From Eq. 2.82, we can see that the dispersive shift corresponds to a shift in resonator frequency that is dependent on the state of the qubit to be in either $|g\rangle$ or $|e\rangle$ state. Thus, by measuring the shift of the resonant frequency of the readout resonator, we can determine the state of the qubit.

2.6.2 Experimental readout data

In Fig. 2.10(b) below, we display the measured transmission $|I + iQ|$ (arbitrary unit) through the readout line as a function of frequency with the qubit prepared in either the ground or excited state. If we prepare qubit in the ground state, we obtain the blue line where the dip corresponds to the loaded resonance of the readout resonator. If we excite the qubit in the excited state by first

5. Note that in certain cases, these terms can be important and should not be neglected as in Ref. [48]

applying a π pulse through the XY drive line, the resonance of the readout resonant is changed and its resonance changes by twice the dispersive shift $2\chi/2\pi$ and we obtain the red line. The shift is dependent on the detuning between the qubit and the readout resonator, Δ. The difference between the red and the blue traces is how we are able to projectively measure the state of the qubit.

We plot the equivalent data in the two-dimensional complex IQ plane as shown in Fig. 2.10(c). If we prepare the qubit in the ground state, we see that the IQ points are centered at a region in the IQ plane. If instead the qubit is prepared in the excited state, we see that the IQ points are now centered at another region in the IQ plane. This allows us to discriminate the state of the qubit by drawing a discrimination line in between the two clouds and assigning different regions of the IQ plane to either the ground state $|g\rangle$ or the excited state $|e\rangle$ of the qubit. If the measured signal lies on the left side of the line, the qubit is in the ground state $|g\rangle$. Conversely, if the measured IQ lies on the right side of the line, the qubit is in the excited state $|e\rangle$. From this calibration, we can determine the probability of the qubit to be in either state at the end of each measurement. We note that as is clear from Fig. 2.10(c), the readout measurement is imperfect and there is some chance of incorrectly reading out the state of the qubit. This is known as readout error and can be corrected through linear inversion. A detailed discussion is provided in Chapter 4.

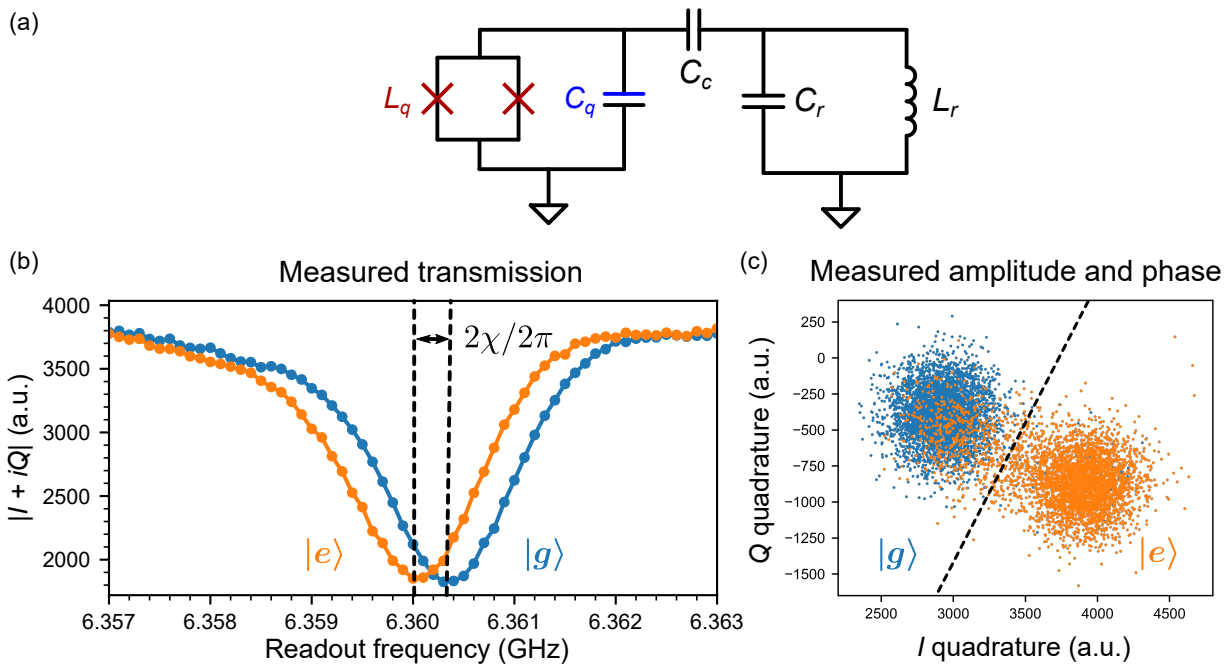

Figure 2.10: Qubit readout. (a) Superconducting qubit measurement circuit for dispersive readout. The measurement circuit consists of a readout resonator capacitively coupled to a qubit via a coupling capacitor C_c. When the qubit is in a different quantum state, the resonance of the readout resonator shifts. Such shift translates to a change in transmission through the readout resonator. (b) Measured transmission amplitude $|I + iQ|$ through the readout resonator when the qubit is initially prepared in $|g\rangle$ (blue) and $|e\rangle$ states (orange). The overall transmission offset is arbitrary, set by the various attenuation and amplification in the measurement signal chain. The difference in the resonant frequencies of the resonator when the qubit is in state $|g\rangle$ and in $|e\rangle$ is twice the dispersive shift $2\chi/2\pi$. Here, $2\chi/2\pi = 0.3$ MHz. (c) The equivalent data plotted in the complex transmission IQ plane with blue and orange points corresponding when the qubit is in the ground or excited state, respectively. This data allows us to assign measurements in the IQ plane to either the ground or excited state, discriminated by the dashed line in the IQ plane. The size of the two clouds is dependent on the noise in the measurements. The readout measurement also includes state preparation errors as well; the qubit can change state after the initial state preparation, for example due to T_1 and $T_{2,\text{Ramsey}}$ processes during readout.

Bandpass filter

As an aside, we note that more complex readout schemes with bandpass filters can be used in the readout chain to enable high-fidelity fast readout [44, 43]. This is done by engineering the microwave environment of the readout line by placing another resonator between the readout resonator and the measurement waveguide. The second resonator acts as a filter such that the readout resonator strongly couples to the measurement waveguide at the readout frequency $f \approx 6$ GHz but weakly couples to the chain at the qubit frequency $f \approx 5$ GHz. The filter increases the coupling of the readout resonator to the measurement waveguide by the quality factor of the filter Q_F. In our experiment, we were able to obtain decent readout visibility without the use of the bandpass filter. However, it is possible that employing a filter could further improve the readout fidelity to be $> 95\%$.

Airbridges

Airbridged ground connections across transmission lines play a crucial role in superconducting quantum circuits as on-chip transmission lines can break ground planes into patches across the chip. If these ground plane patches are not connected by airbridges, they can result in slot-line modes which can be an additional source of dissipation for the qubits, limiting their T_1. We fabricate airbridges on our superconducting quantum circuit using a liftoff process similar to Ref. [49] to electrically connect the ground planes together. We deposit SiO_2 as a sacrificial layer, over which a layer of aluminum stretching across the SiO_2 connecting the ground planes on either side of the transmission line is deposited. The aluminum deposition is preceded by an Ar ion mill to mill away the native aluminum oxide on the base layer and establish galvanic contact between the deposited aluminum and the base layer. The sacrificial SiO_2 layer is etched away via vapor HF in the last step of the fabrication to release the airbridges. A detailed process flow of the fabrication is provided in Appendix A.

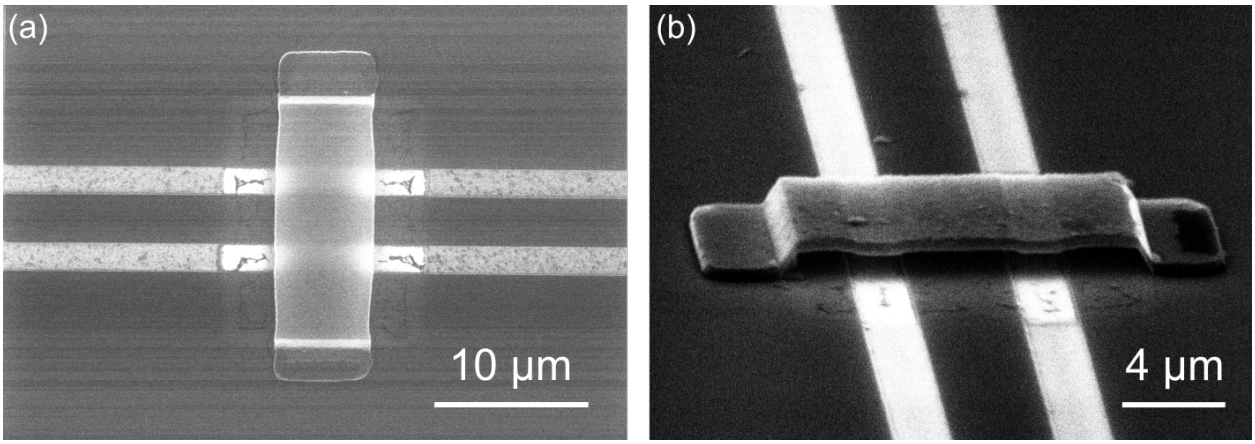

Figure 2.11: Airbridge over a transmission line. (a) Top-down view and (b) angled view of a free-standing airbridge connecting the ground planes across the transmission line. The SiO_2 scaffold has been removed via vapor HF.

Packaging

Another crucial aspect of measuring superconducting qubits is packaging. Packaging is the intermediary between the quantum circuit and the coaxial cables at the base stage of the fridge. As shown in Fig. 2.12(a) below, we placed our chip inside a superconducting aluminum sample box. For electrical connections, we wirebond the chip to a printed circuit board insert which is in turn soldered to non-magnetic SMA connectors. The aluminum wirebonds superconduct at low temperature, providing a close to ideal connection between the chip and the mount[6]. The PCB inserts are made of Rogers board (RO4350B) and are plated with gold on top for ease of wirebonding. The samples can then be connected to the coaxial cables at the base temperature stage of the fridge through these SMA connectors. Inside the fridge, the aluminum sample mount is sandwiched between two high permeability μ-metal magnetic shields which protect the device from magnetic noise from the environment.

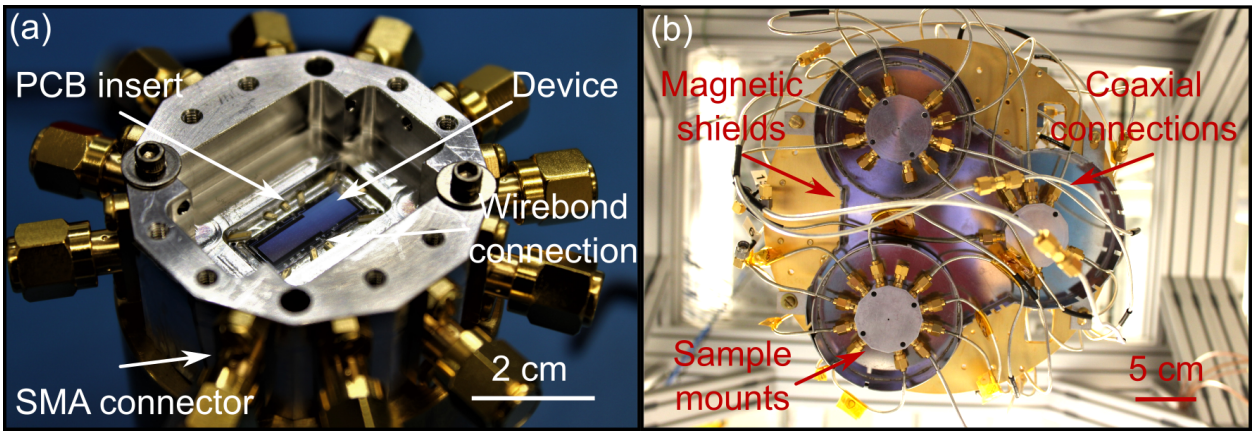

Figure 2.12: Device packaging. (a) Picture of the quantum circuit chip inside the aluminum sample mount. The superconducting quantum circuit chip is wirebonded to the PCB inserts which in terms are soldered onto SMA connectors. (b) Picture of the sample mount in (a) placed inside the fridge and connected to coaxial cables. The coaxial cables then lead up from the base stage of the fridge to room temperature. The two μ-metal magnetic shields can be seen behind the mount.

6. In reality, each wirebond does have a small inductance on the orders of a few nanohenries.

2.7 Superconducting qubit characterization

2.7.1 Energy relaxation time (T_1)

One of the most basic characterizations of superconducting qubits is how long they can keep their excitation. This is known as the energy relaxation time T_1. We measure the qubit T_1 by exciting the qubit in the excited state $|e\rangle$ with a π pulse and watching how long it can keep this excitation as a function of time. By fitting the decay with an exponential, we find a typical T_1 of approximately $10 - 20$ μs, consistent with those of other qubits fabricated and measured using similar setups in our lab as well as many other groups. In Fig. 2.13(a), we show the measured T_1 data of the device used in Chapter 4.

2.7.2 Phase coherence time ($T_{2,Ramsey}$)

The second time of interest is how long a superposition state encoded in the qubit can keep its phase ϕ. This is known as the phase coherence time $T_{2,\text{Ramsey}}$. We measure this via a Ramsey sequence by first exciting the qubit in an equal superposition state $|e\rangle + i|g\rangle$, waiting for a delay time to see how the qubit has dephased, and projecting the state to the measurement axis (Z axis) via another $\pi/2$ pulse; see Fig. 2.13(c). To increase the visibility, we detune the $\pi/2$ pulse slightly so that the qubit precesses around its Z axis in the rotating frame, resulting in oscillations in the final measurement. In Fig. 2.13(c) we show the measured $T_{2,\text{Ramsey}}$ of the device used in Chapter 4. We fit the envelope to a decaying exponential $\exp[-t/T_{2,\text{Ramsey}}]$ [41] and obtain typical coherence time of $1 - 2$ μs at the operating point of $\omega_{ge}/2\pi = 5.504$ GHz. The decoherence process on the Bloch sphere is shown schematically in Fig. 2.13(d).

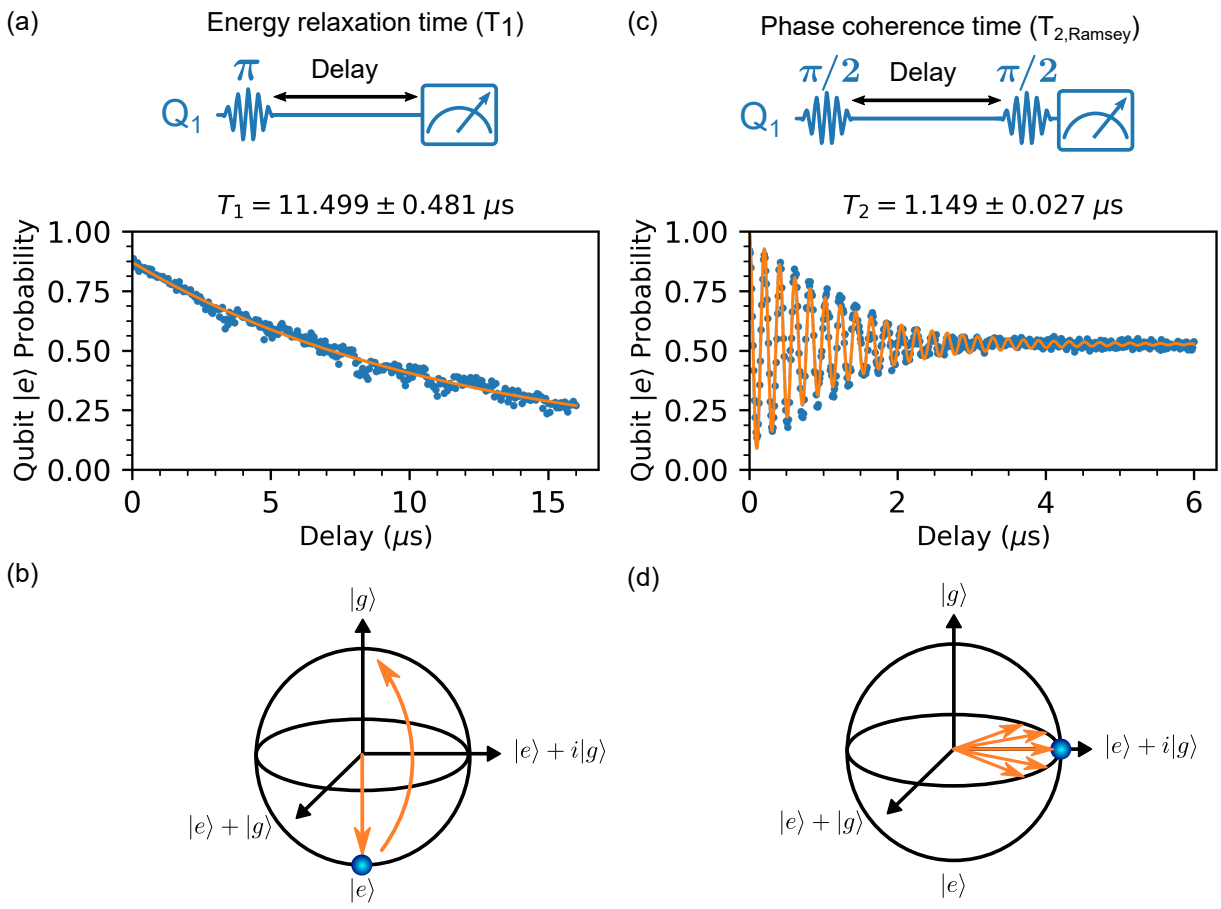

Figure 2.13: Qubit lifetime and coherence time. (a) Qubit lifetime measurement. To measure the energy relaxation time T_1 of the qubit, we excite the qubit in the excited state $|e\rangle$ with a πpulse and measure its decay as a function of time. The pulse sequence is shown inset. From fitting the data to a decaying exponential (orange trace), we obtain $T_1 = 11.5 \pm 0.5$ μs, corresponding to a quality factor of $Q = \omega T_1 = 4 \times 10^5$. (b) Bloch sphere representation of the energy relaxation process. The excitation in the $|e\rangle$ state is represented by a blue sphere. (c) To measure the phase coherence time $T_{2,\text{Ramsey}}$ of the qubit. We excite the qubit in a superposition state on the equator of the Bloch sphere via a $\pi/2$ pulse and watch its decay. In the end, we map it back to the measurement axis (Z axis) via another $\pi/2$ pulse to measure the qubit. The excited state population is fitted to a cosine with a decaying exponential envelope to obtain the $T_{2,\text{Ramsey}}$ coherence time. We introduce a slight detuning $\Delta\omega_{\text{fringe}}$ to the $\pi/2$ pulse such that the qubit precesses around its Z axis in the rotating frame to allow for better fitting. (d) Bloch sphere representation of the decoherence process. Dephasing causes a spread in the expectation value of the phase, causing a point to spread into a band of values of different ϕ's as represented by a band of orange vectors in the schematic.

2.8 Coupling

To make a useful quantum system, various quantum systems need to couple to one another. In an electrical circuit, this is done by engineering a coupling capacitor or inductor between two LC resonators. Here, we explore these two coupling schemes.

2.8.1 Capacitive coupling

Two LC resonators can be coupled to one another capacitively by simply placing a coupling capacitor C_c in between them; see Fig. 2.14.

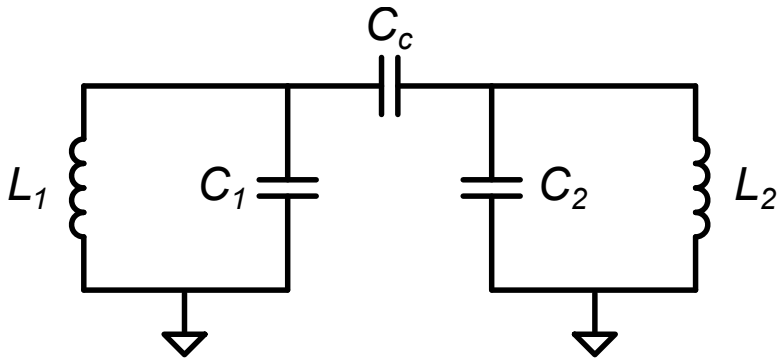

Figure 2.14: Capacitively coupled LC resonators. Circuit schematic of two capacitively coupled LC resonators with coupling capacitance C_c.

The coupling g for the circuit is:

$$g = \frac{C_c}{2}\sqrt{\frac{\omega_1\omega_2}{(C_1+C_c)(C_2+C_c)}}. \tag{2.84}$$

where ω_1 and ω_2 are the resonant frequencies of the two LC resonators. Capacitive coupling is preferred for strong, efficient coupling to parallel LC resonators, where the resonances correspond to impedance maxima. Considering the relation $V = ZI$, a parallel resonance presents a large impedance on resonance; a fixed current can thus drive a larger voltage across the other resonator resulting in a larger coupling g.

2.8.2 *Inductive coupling*

Another way to couple resonant circuits is through an inductor. This is typically done by placing the inductors of two LC resonant circuits in close proximity resulting in a mutual inductance M between the two inductors; see Fig. 2.15.

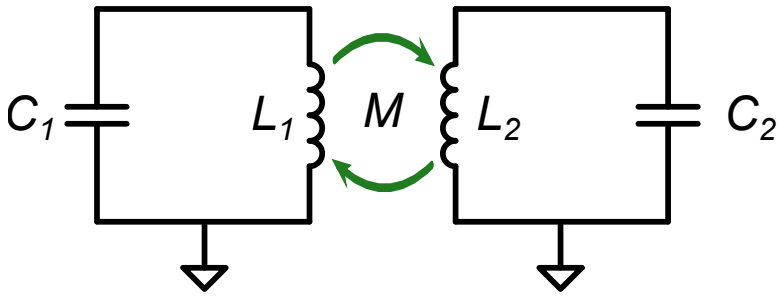

Figure 2.15: Inductively coupled LC resonators. Circuit schematic of two inductively coupled LC resonators with mutual inductance M.

The coupling g for the circuit is:

$$g = -\frac{M}{2}\sqrt{\frac{\omega_1\omega_2}{L_1L_2}}, \tag{2.85}$$

where ω_1 and ω_2 are the resonant frequencies of the two LC resonators. Inductive coupling is preferred for strong, efficient coupling to series LC resonators, where the resonances correspond to impedance minima. Considering the relation $I = V/Z$, a series resonance presents minimal impedance on resonance; a fixed voltage can thus drive a larger current across the other resonator resulting in a larger coupling g.

2.8.3 *Tunable inductive coupling*

Unlike geometric coupling where the coupling is always on, we can use Josephson junction based tunable coupler [50, 51] to turn on and off the coupling between coupled quantum systems on-demand. Tunable coupling offers several distinct advantages over a fixed capacitive or inductive coupling. In the context of our experiment in Chapter 4, the tunable coupler plays a key role in turning on/off the interaction of our qubits to the channel on-demand. The coupling can be turned off during state preparation at each quantum node. This retains the qubit's coherence during state

preparation and allows for independent tune up of each qubit without worrying about its interaction with the channel and the other qubit. Conversely, when we want the qubit to couple to the channel for state transfer, the coupling can be turned on and modulated in time with nanosecond precision. As we will show in Chapter 4, this is crucial to realize the adiabatic state transfer protocol, the focus of this thesis. After the desired transfer is achieved, the coupler can then be turned off and the quantum information can be processed coherently in the receiver qubit.

Our tunable coupler is based on the gmon design that was first developed at UCSB [50, 52, 53, 54]. This type of Josephson junction based coupler design affords dynamic tunability turning from 0 to 50 MHz on nanosecond time scales while retaining the coherence of the qubit [50]. The large coupling strength and dynamical tunability of the gmon make it a suitable tunable coupling circuit for a quantum node. The tunable coupler is implemented as an π-inductive network and the qubit is connected to ground through this inductive network. One path to ground is through the first meander inductor $L_{g1} = 0.2$ nH, while the other path to ground is through the Josephson junction in series with a second meander inductor $L_{g2} = 0.2$ nH. This is depicted in the circuit schematic in Fig. 2.16(a) and an optical micrograph of the device used in this thesis is shown in Fig. 2.16(b). The inductance of the Josephson junction $L_T(\delta)$ can be tuned by controlling the phase across the junction δ, brought about by an inductively coupled flux bias line ("G" in Fig. 2.16(b)). By modulating δ, we can control the ratio of the current flowing through each branch of the bridge. When $\delta = \pi/2$, the junction inductance is very large, presenting a large a large impedance to the right branch of the inductive network, and all the qubit current I_q goes to ground through the left meander inductor L_{g1} (i.e. $I_1 = I_q$, $I_2 = 0$) and the coupling is turned off. Conversely, when $\delta = \pi$ the junction inductance is negative $L_J = -L_{J0}$, canceling out the geometric inductance of the network. This allows the qubit current to flow through the right coupler branch (i.e. $I_2 \neq 0$) and the coupling between qubit and the transmission line is turned on.

To treat this formally, we consider the circuit of the qubit and the tunable coupler network in Fig. 2.16(a), where a current I_q flows from the left qubit to ground. For simplicity, we set $L_{g1} = L_{g2} = L_g$. The current through the coupler junction I_2 to the second grounding inductor

L_{g2} can be written approximately as [50]

$$I_2 = \frac{I_q L_g}{2L_g + L_T(\delta)}. \tag{2.86}$$

This current generates a flux in the second branch of the network $\Phi_2 = I_2 L_g$. Using these two expressions, the mutual inductance can be expressed as

$$M = \frac{\Phi_2}{I_q} = \frac{{L_g}^2}{2L_g + L_T(\delta)} = \frac{{L_g}^2}{2L_g + L_{T0}/\cos\delta}, \tag{2.87}$$

where I have used the previously derived expression for nonlinear inductance of a Josephson junction (Eq. 2.40) for the coupler inductance L_T in the last equal sign and δ is the phase difference across the coupler junction. This can be substituted into the coupling strength expression of two inductively coupled LC resonators (Eq. 2.85). Doing so, we arrive at the coupling strength of the coupler as a function of its phase δ:

$$g(\delta) = -\frac{1}{2}\frac{M}{\sqrt{L_1 L_2}}\sqrt{\omega_1 \omega_2} \tag{2.88}$$

$$= -\frac{1}{2}\left(\frac{{L_g}^2}{2L_g + L_{T0}/\cos\delta}\right)\sqrt{\frac{\omega_q \omega_2}{(L_g + L_q)(L_g + L_2)}}, \tag{2.89}$$

where $L_1 = L_q$ and $\omega_1 = \omega_q$ are the inductance and resonant frequency of the qubit and L_2 and ω_2 are the inductance and resonant frequency of the system it is coupled to.

2.8.4 Tunable capacitive coupling

We note that tunable capacitive couplers have also been developed [55] and implemented [11, 56, 57, 58]. However, they are not used in the experiment described in this thesis and are thus not discussed in detail here. For a detailed description of tunable capacitive couplers, see Ref. [55].

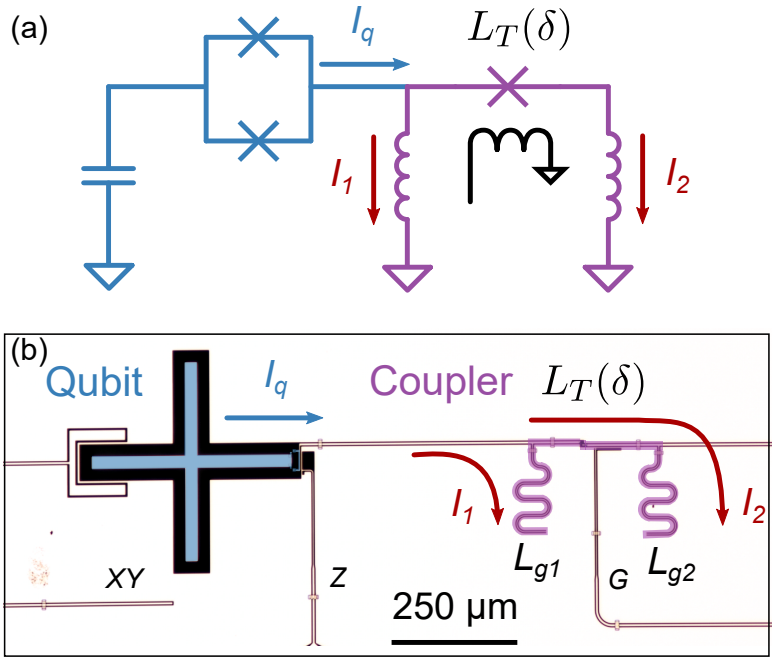

Figure 2.16: (a) Circuit schematic of a quantum node consisting of a qubit (blue) and its tunable coupler (purple). The qubit current I_q is marked by the blue arrow. The currents through the two branches of the tunable coupler networks I_1 and I_2 are marked by red arrows. (a) False-color optical micrograph of the qubit and the tunable coupler. The coupler is controlled by a G control line inductively coupled to the coupler junction. Current sent down the control line brings about a magnetic flux through the superconducting loop and changes the phase δ across the coupler junction, tuning its effective inductance $L_T(\delta)$

CHAPTER 3

SUPERCONDUCTING VARIABLE COUPLER NETWORK

In this chapter, we explore a fast and broadband superconducting variable coupler, with switching times on the orders of nanosecond. This is a key device for the experiments in Chapter 4.[1]

3.1 Introduction

Switches are highly useful components in radiofrequency, microwave and optical classical communication systems, and likely will play an important role in quantum communication applications. Conventional semiconductor-based microwave couplers have been used with superconducting quantum circuits, enabling for example the *in situ* measurements of multiple devices via a common readout chain. However, the semiconducting elements are lossy, and furthermore dissipate energy when switched, making them unsuitable for applications requiring rapid, repeated switching in cryogenic systems. Superconducting Josephson junction-based couplers, in contrast, can be designed for dissipation-free operation with fast switching and are easily integrated with superconducting quantum circuits. These enable, for example, the on-chip, quantum-coherent routing of microwave photons, providing an appealing alternative to semiconductor switches. Here, we present and characterize an on-chip superconducting variable coupler based on the superconducting quantum interference device (SQUID), with two parallel Josephson junctions. The variable coupler is dissipation-free, features large on-off ratios in excess of 40 dB, and the coupling can be changed over a time of $\sim 5 - 10$ ns. The device is broadband, with "on" transmission above -1 dB over a 1.5 GHz bandwidth, and "off" isolation below -20 dB over a 3.8 GHz bandwidth. The center operating frequency can further be tuned from 3 to 8 GHz, achieving similar performance at each operating frequency. The simple design presented here can be readily integrated with superconducting qubit circuits, and can be easily generalized to realize a four- or more port device.

1. The following is reproduced from "A fast and large bandwidth superconducting variable coupler", Hung-Shen Chang, et al. *Applied Physics Letters* (2020), with the permission of AIP Publishing.

In recent years, superconducting qubit circuits have made significant progress, showing that distributed quantum computing using superconductors may be possible. This drives a need for active microwave components able to route and modulate single microwave photons while preserving quantum coherence. A superconducting variable coupler capable of controllably routing microwave photons between different ports would enable the distribution of entanglement between different nodes in a quantum network [59, 20]. Additionally, such a coupler would allow for multiplexing of classical microwave signals, enabling the integrated readout and control of multiple qubits using a single microwave cable. A few different realizations of superconducting microwave-frequency couplers have been demonstrated [60, 61, 62, 63, 64]; however, these mostly have fixed operating frequencies, involve complicated fabrication, and often suffer from limited bandwidth, limiting their uses to small-bandwidth applications.

3.2 Our approach

Here we report the design, implementation and characterization of a broadband, three-port superconducting variable coupler, based on the Josephson flux-tunable SQUID [65]. A variable coupler is a generalized form of a switch. Specifically, a variable coupler affords continuous control of the transmission, but it can also be operated in a binary fashion ("on" and "off") as a switch but not vice versa. We use the intrinsic LC plasma resonance of the SQUID to control the transmission to each port in the coupler, enabling fast and widely-tunable operation, providing a simple approach that preserves a direct galvanic coupling through each port. We experimentally characterize the device at cryogenic temperatures, and demonstrate a large on-off power ratio of over 40 dB, a wide instantaneous bandwidth exceeding 1 GHz for both transmission and isolation, and fast switching times of a few nanoseconds. The design affords complete and continuous electronic control of the transmission between the three ports, enabling fast and coherent routing of single photon microwave signals. The coupler can be readily integrated with superconducting qubits, as shown in Ref. [66], and can be easily extended to a larger number of ports.

3.3 Device description

Our three-port device controllably routes signals from port 2 or port 3 to port 1, using two Josephson SQUIDs as tunable resonators placed in series with the two input ports, as shown in Fig. 3.1. The SQUID plasma resonance frequency is defined as $\omega_p = 1/\sqrt{LC}$, where L is the Josephson plus geometric inductance of the SQUID loop, and C is the associated parallel capacitance. When this frequency is resonant with the incoming signal, the SQUID presents a large series impedance, and fully reflects any incoming signals. Conversely, when the resonance frequency is far detuned from the incoming signal, it presents a small impedance and a substantial fraction of the incoming signal is transmitted through the SQUID. By controlling the magnetic flux linking the SQUID, using an on-chip flux line, we can tune the resonance frequency and thus vary the SQUID transmission continuously from zero to nearly unity. Using a shunting capacitance in parallel with the SQUID further improves the transmission in detuned operation, by better matching the circuit to the system impedance (here $Z_0 = 50\ \Omega$).

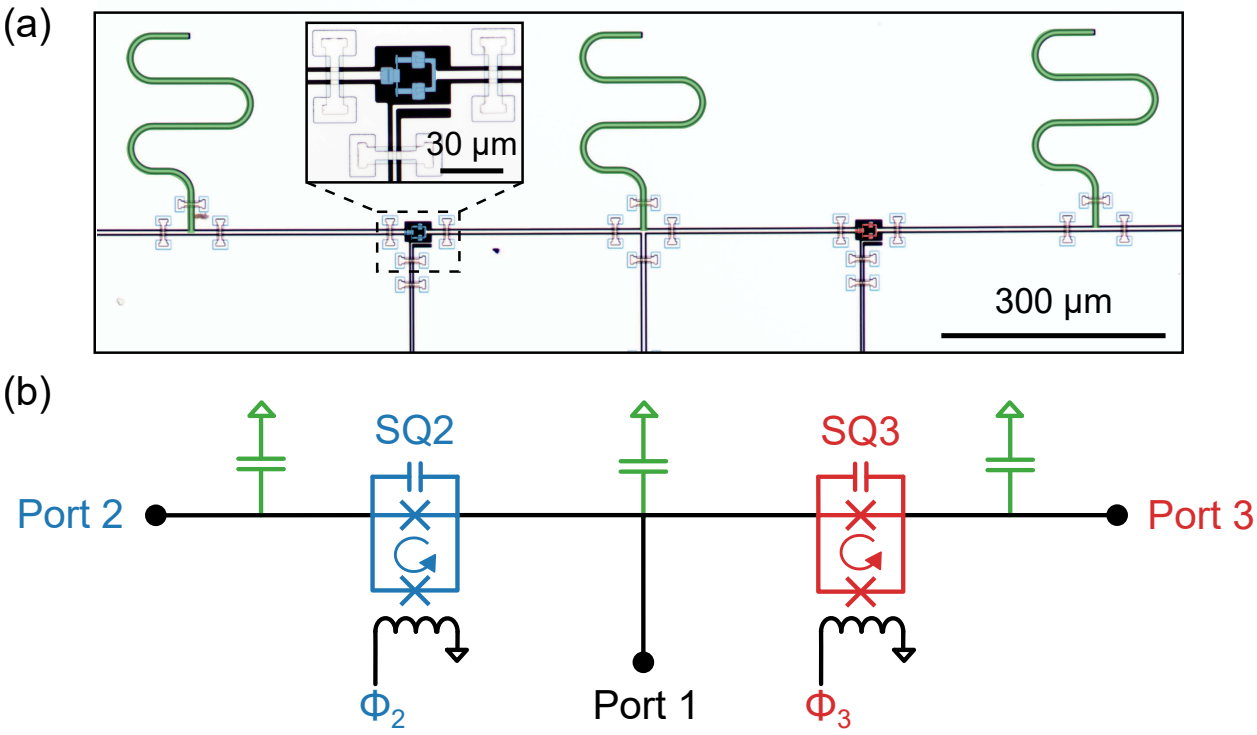

Figure 3.1: Device description, where signals into port 2 or port 3 are routed to port 1, using those ports' associated SQUID couplers. (a) False-color optical micrograph of the complete device. Inset: magnified view of one SQUID and its associated flux control line. (b) Schematic circuit diagram for (a), with port 1 in black, port 2 and its associated SQUID (SQ2) in blue, port 3 and its SQUID (SQ3) in red, with three shunt capacitors in green.

3.4 Experimental setup

The device is fabricated on a sapphire substrate with Al base wiring and Al-Al oxide-Al Josephson tunnel junctions, using a process outlined in Appendix A, with slight modifications. We characterize the coupler by cooling it in a dilution refrigerator with a base temperature below 10 mK and measuring the transmission between ports 2 and 3 and port 1 using a microwave vector network analyzer. Fig. 3.2 shows the schematic of the wiring inside the refrigerator. Ports 2 and 3 are treated as input lines and are heavily attenuated and filtered at each temperature stage. Port 1 is treated as an output line, connected to two circulators in series (QuinStar) at the mixing temperature stage, then amplified by a high electron mobility transistor amplifier (Low Noise Factory) at a temperature of 4 K, followed by a room-temperature amplifier (Miteq). This wiring configuration allows us to measure the transmission from port 2 to port 1 and from port 3 to port 1 (S_{12} and S_{13}) but not the transmission in the reverse direction (S_{21} and S_{31}). The device is placed inside an aluminum sample box which is placed inside a single layer of high permeability magnetic shielding, bolted to the mixing chamber stage; electrical connections are made with aluminum wire bonds.

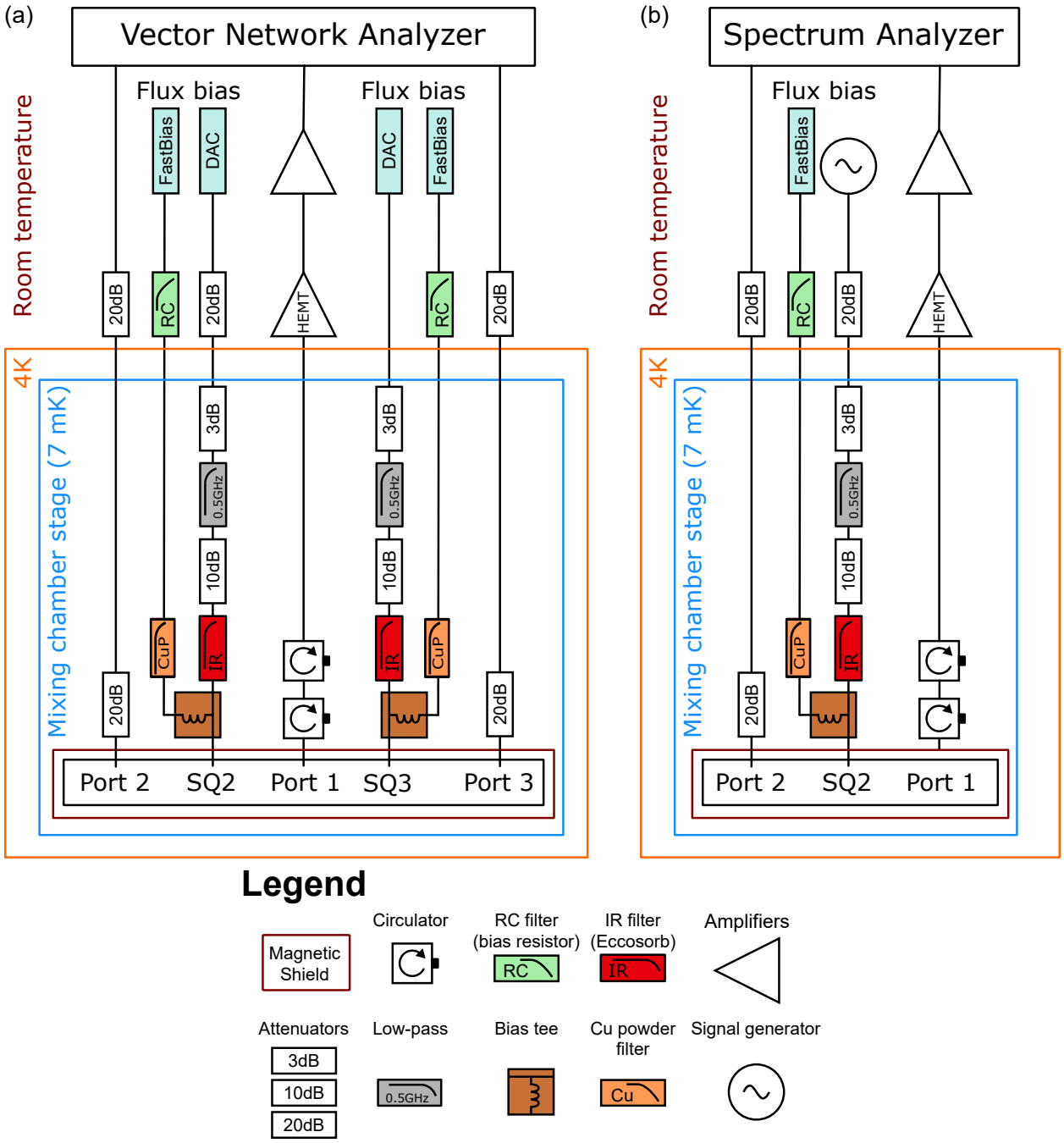

Figure 3.2: Schematic of the measurement setups for measuring (a) microwave transmission through the device with a vector network analyzer and (b) sideband spectrum as shown in Fig. 4 of the main text with a spectrum analyzer. For this measurement, we connect the flux bias lines to a signal generator outside of the fridge to modulate the flux through the SQUID loop (SQ2). The output spectrum is measured with a spectrum analyzer. Solid lines mark the different temperature stages inside the dilution refrigerator.

3.5 Experimental results

3.5.1 Flux controlled transmission

In Fig. 3.3, we show electronic control of transmission from port 2 and port 3 to port 1, as a function of the control flux. With port 3 turned off ($|S_{13}| < -40$ dB), flux-biasing SQ2 controls the transmission S_{12} from port 2 to port 1. The transmission can be tuned continuously from near-unit transmission 0 dB to -40 dB, demonstrating a large on-off ratio (calibration of unit transmission is described in the section below). Transmission S_{13} from port 3 to port 1 is maintained at a uniform small value near -40 dB for all SQ2 flux biases. We observe two pronounced dips in $|S_{12}|$ as a function of flux, which corresponds to where the SQUID plasma resonance is resonant with the probe signal at $f = 5$ GHz, reflecting almost all the signal. In Fig. 3.3(b), we show a detail for the transmission at the two flux bias points where port 2's impedance is nearly $50\ \Omega$, resulting in near-unit transmission, where the measured transmission is normalized to 0 dB at the maximum transmission point. The coupler's insertion loss is characterized in a separate measurement, where it was found to be around $\sim 0.6 \pm 0.2$ dB (See Section 3.5.7). We fit the flux dependence of the transmission using a linear circuit model [30], modeling the SQUID as a parallel LC resonator with flux tunable inductance and extract the unbiased inductance of the SQUID to be 166.5 ± 0.1 pH, the SQUID capacitance to be 199.3 ± 0.3 fF, and the shunting capacitance to be 160.0 ± 0.4 fF. For all subsequent measurements in the main text, the device is tuned to operate near $f = 5$ GHz.

3.5.2 Power sweep

At high powers, non-idealities due to the intrinsic SQUID nonlinearity become apparent. We characterize the power-handling of our device by measuring the transmission as a function of input power with port 2 "on" and port 3 "off," as shown in Fig. 3.3(c). To maintain a relative transmission level above -1 dB through port 2, we find a chip-level maximum power into port 2 of about -83 dBm, while maintaining the transmission below -20 dB for port 3, the maximum power into port 3 is about -95 dBm

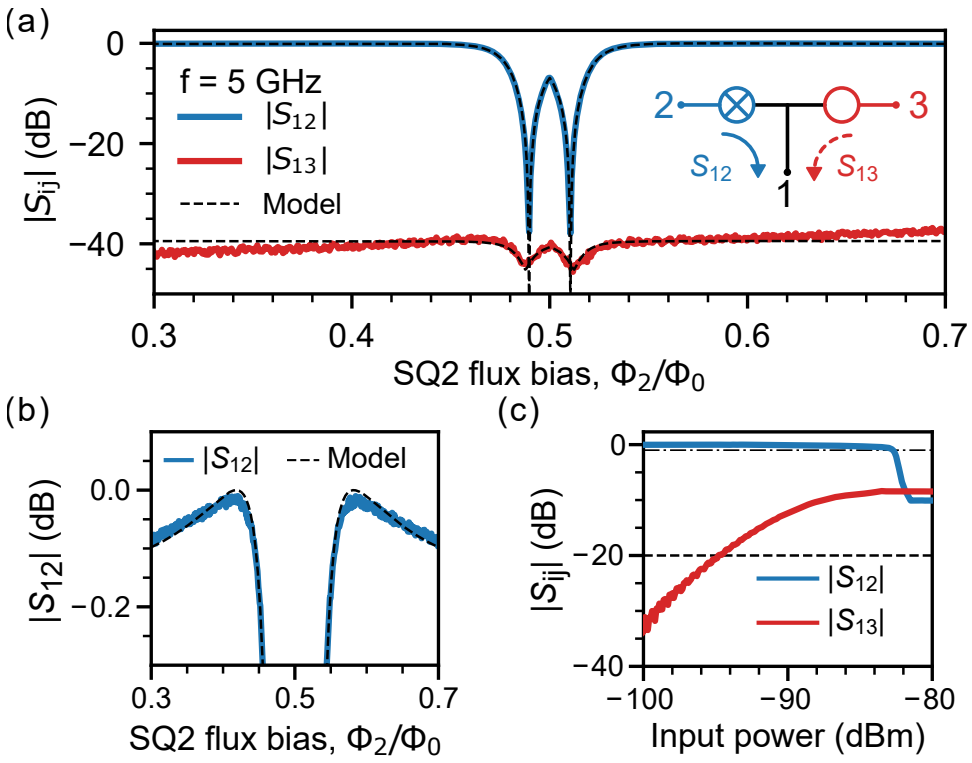

Figure 3.3: Flux-controlled SQUID transmission. (a) Normalized transmission for a fixed frequency signal at $f = 5$ GHz from ports 2 and 3 to port 1, as a function of the SQ2 flux bias Φ_2 in units of the magnetic flux quantum $\Phi_0 = h/2e$. Transmission $|S_{12}|$ is tuned continuously from unit transmission to -40 dB. Port 3's transmission $|S_{13}|$ is maintained near -40 dB for all SQ2 flux bias values. Dashed lines are a fit to a linear circuit model [30], where the SQUIDs are modeled as parallel linear LC resonators with flux-tunable inductances L. (b) Detail of the transmission vs. flux bias curve in (a), showing that near-unit transmission is achieved at two flux bias points, corresponding to where port 2's impedance is nearly matched to $50\ \Omega$. (c) Transmission $|S_{12}|$ (blue) and $|S_{13}|$ (red) at their maximum and minimum transmission points, respectively, as a function of port 2 and port 3 input power.

3.5.3 *On/off spectroscopy*

In Fig. 3.4, we display the transmission through each port ($|S_{12}|$ and $|S_{13}|$) over a broad frequency range with each port tuned to its maximum and minimum transmission points respectively. In mode A, the SQUID fluxes are set so that port 2 is set to its maximum transmission while port 3 is set to its minimum, while in mode B the fluxes are set to where port 3's transmission is maximized while port 2's transmission is minimized. In mode A, we observe a flat transmission through port 2 with $|S_{12}^A| \gtrsim -1$ dB while port 3's transmission has $|S_{13}^A| \lesssim -20$ dB, both across a ~ 1.5 GHz band centered at 5 GHz. In mode B, we measure a large isolation bandwidth for port 2 with an equivalently broad and large transmission through port 3. The on-off ratios for both ports is greater than 40 dB for the same bandwidths.

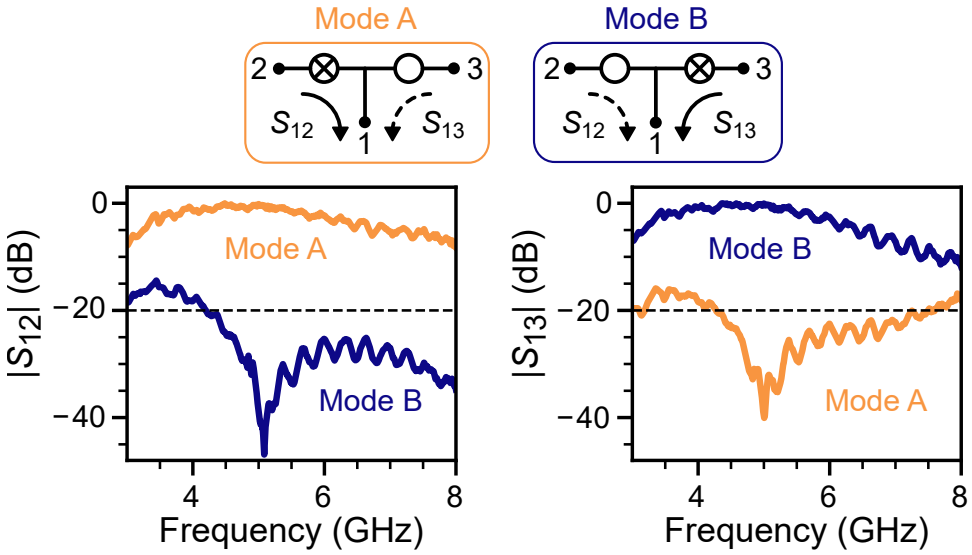

Figure 3.4: Transmission $|S_{12}|$ (left) and $|S_{13}|$ (right) for two flux-tuning points, mode A (orange, see top left diagram) where port 2 is at maximum and port 3 at minimum transmission, and mode B (blue, see top right diagram) where these are reversed. Dashed lines represent the -20 dB transmission threshold used to define the isolation bandwidth.

3.5.4 Frequency tunability

These measurements demonstrate operation around a 5 GHz probe signal. To demonstrate the broad tunability of the device, we measure the variable coupler at different operating frequencies ranging from 4 to 8 GHz and perform spectroscopy measurements similar to those in Fig. 3.4. We show that the flux tunability of the SQUIDs allow equivalent operation for operating frequencies between 4 and 8 GHz, demonstrating an octave of tunable, broadband operation, achieving on-off ratios in excess of 40 dB, and "on" and "off" bandwidths of more than 1 GHz for all operating frequencies. Device parameters extracted from these spectra are summarized in Table 3.1.

Operating frequency (GHz) f_0	On/off ratio (dB) $\lvert S_{12}^A/S_{12}^B\rvert$	Transmission bandwidth (GHz) $\lvert S_{12}^A\rvert > -1$ dB	Isolation bandwidth (GHz) $\lvert S_{12}^B\rvert < -20$ dB
4.025	43.423	1.28	> 1.995
4.405	61.48	1.595	2.465
5.085	46.899	1.48	> 3.8
5.565	34.574	1.6	2.39
6.135	34.19	1.595	2.62
6.455	33.72	1.24	2.18
7.03	33.614	1.485	> 1.9
7.68	33.845	1.59	> 1.58
7.965	35.025	1.595	> 1.3
Operating frequency (GHz) f_0	On/off ratio (dB) $\lvert S_{13}^B/S_{13}^A\rvert$	Transmission bandwidth (GHz) $\lvert S_{13}^B\rvert > -1$ dB	Isolation bandwidth (GHz) $\lvert S_{13}^A\rvert < -20$ dB
4.225	49.529	1.58	> 1.995
4.37	49.134	1.56	> 2.315
5.005	40.066	1.58	3.22
5.36	34.66	1.545	1.51
5.915	32.902	1.54	1.685
6.57	33.393	1.55	1.845
6.895	35.285	1.59	> 1.9
7.54	34.686	1.535	> 1.57
7.775	35.487	1.455	> 1.32

Table 3.1: Performance of the variable coupler at different operating frequencies, measured for S_{12} (upper half) and S_{13} (lower half). All parameters are calculated from the spectroscopy data shown in Fig. 3.5 and Fig. 3.6.

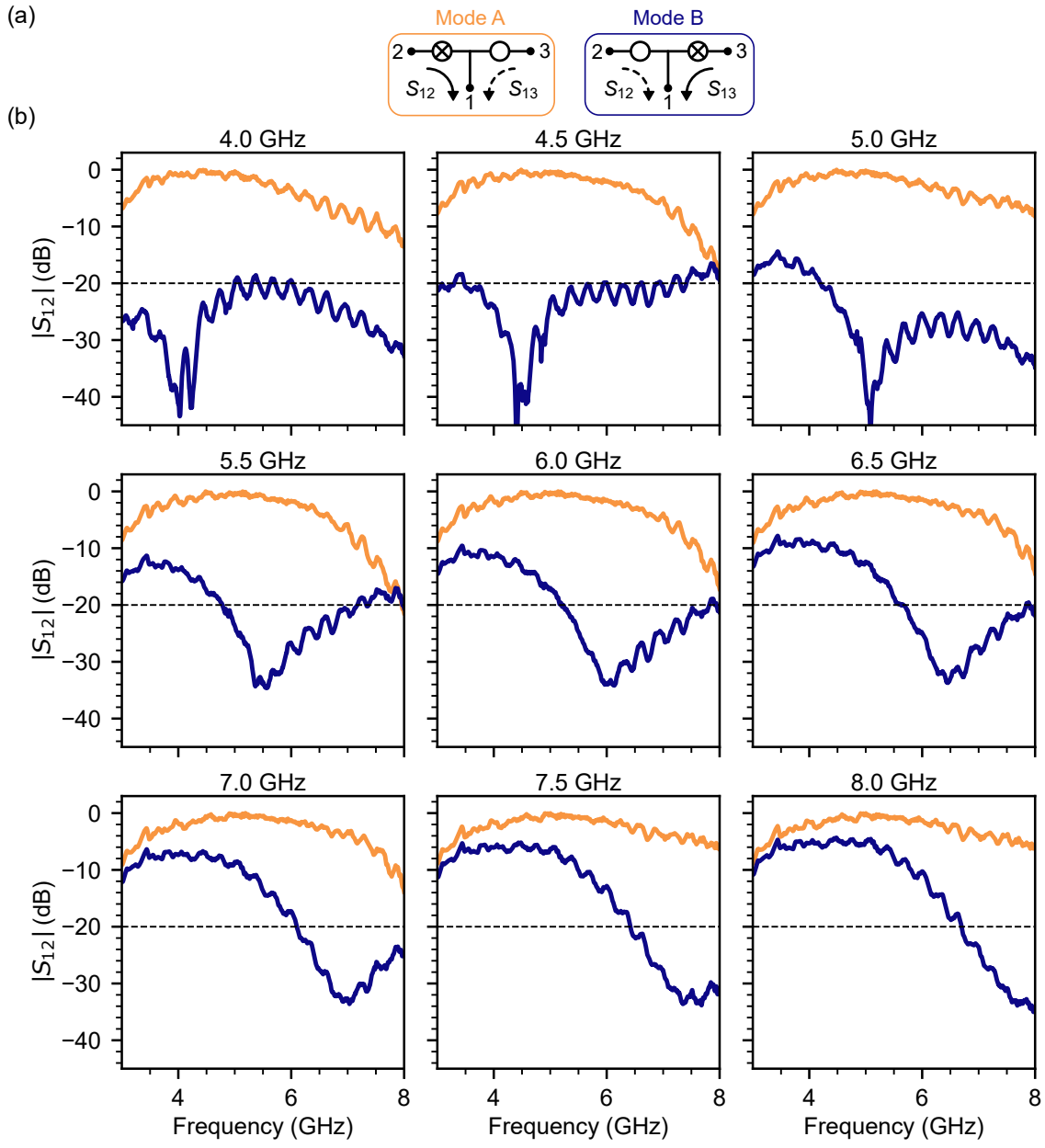

Figure 3.5: Coupler performance for different operating frequencies, between ports 1 and 2. (a) Schematic of the two modes measured here; see main text. (b) Measured transmission from port 2 to port 1 ($|S_{12}|$) as a function of frequency for mode A (orange) and mode B (blue), demonstrating broadband operation. Dashed line represents the -20 dB transmission threshold used to define the isolation bandwidth.

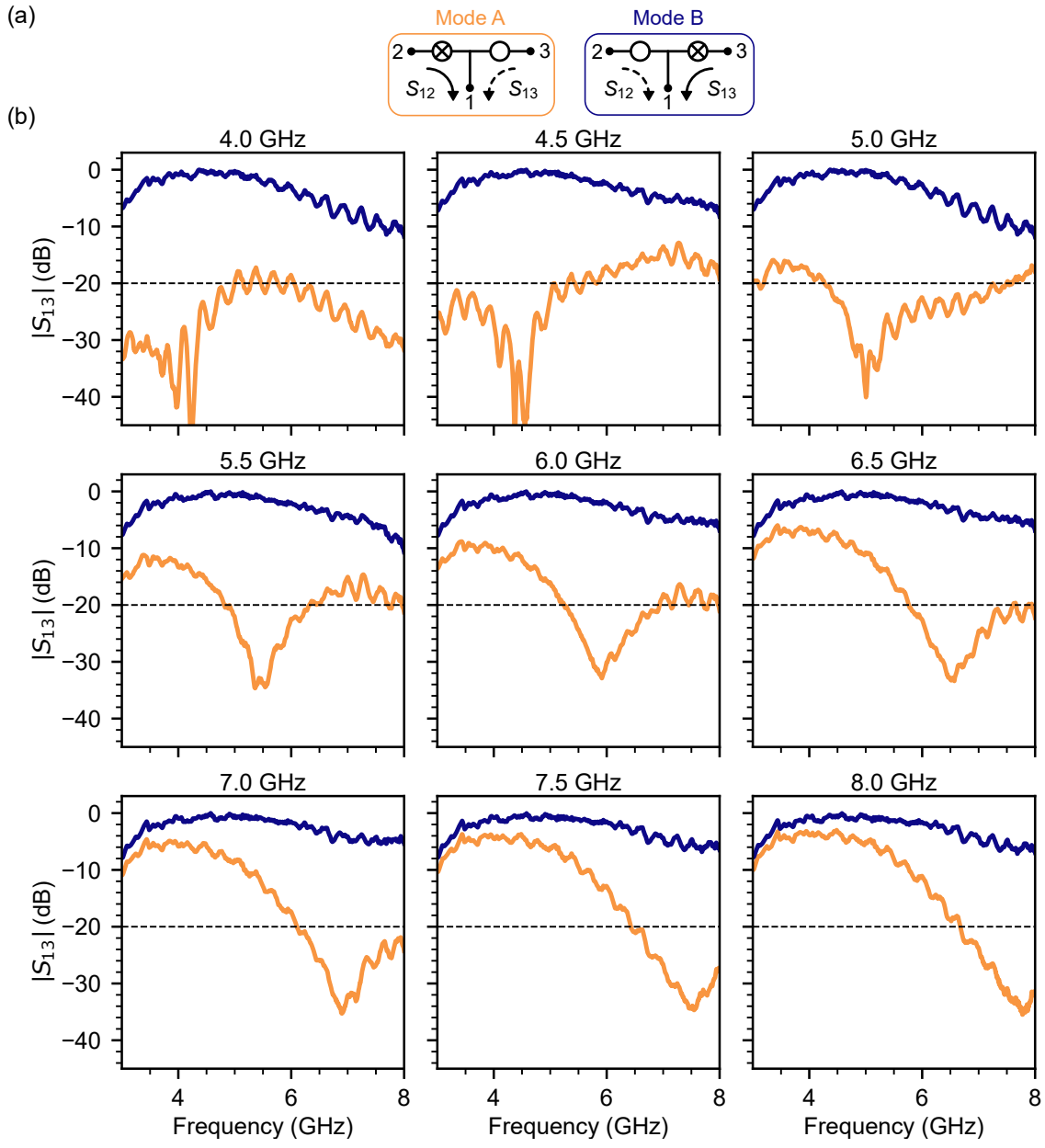

Figure 3.6: Coupler performance for different operating frequencies, between ports 1 and 3. (a) Schematic of the two modes measured here; see main text. (b) Measured transmission from port 3 to port 1 ($|S_{13}|$) as a function of frequency for mode A (orange) and mode B (blue), demonstrating broadband operation. Dashed line represents the -20 dB transmission threshold used to define the isolation bandwidth.

3.5.5 *Fast switching*

We characterize the switching speed of the variable coupler by measuring the transient response of our device as it switches between the two modes, shown in Fig. 3.7. For these measurements, a fixed-frequency signal at $f = 5$ GHz is sent to port 1 and a rectangular pulse is applied to each SQUID's flux line so as to switch from mode A to mode B or vice-versa. The time-domain transmissions $|S_{12}|$ and $|S_{13}|$ are captured for each port using a fast analog-to-digital converter. By fitting the response waveform to a hyperbolic tangent, as shown in the figure, we extract 10% to 90% switching times of 8 ± 1 ns and 4.9 ± 0.4 ns for port 2's off-to-on and on-to-off times, respectively, and 6.6 ± 0.8 ns and 9.0 ± 0.8 ns for port 3's off-to-on and on-to-off times, respectively. These times are mostly limited by the bandwidth of our flux-bias electronics and associated cabling.

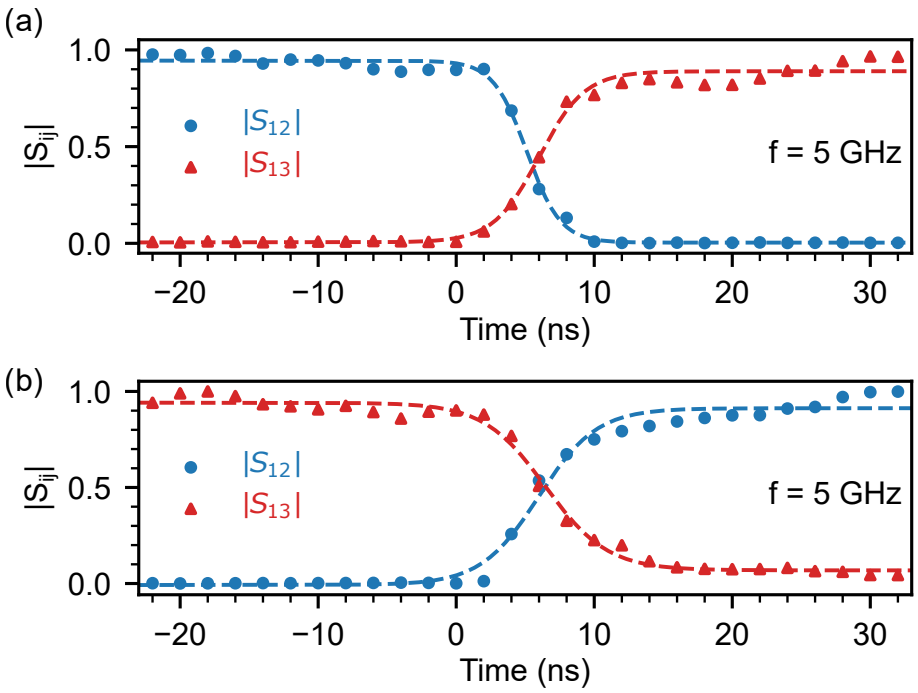

Figure 3.7: Fast switching. Measured rising and falling edges of the waveforms through each port when switched between different operating states. (a) Mode A to mode B. (b) Mode B to mode A. Dashed lines are fit to a hyperbolic tangent to extract the rise and fall switching times.

3.5.6 Sideband generation

A time-periodic modulation of the SQUID flux bias generates sidebands in the transmitted signal, offset from the carrier frequency by integer multiples of the modulation frequency. SQ2's flux bias is set to $0.473\Phi_0$ where $|S_{12}| = -2.0$ dB and $0.052\Phi_0$ from the maximum transmission bias, and port 3 is set to minimum transmission. A fixed-frequency signal at $f = 5$ GHz is applied to port 2 as the carrier signal and SQ2's flux bias is modulated about its set-point with a small radiofrequency modulation of -80 dBm, corresponding to a modulation amplitude of $(2.6 \times 10^{-7})\Phi_0$. We use a spectrum analyzer to measure the transmitted spectrum at port 1, which reveals sidebands on the carrier signal as shown in Fig. 3.8(a) as a function of the modulation frequency, as the latter is varied from 10 to 100 MHz. In Fig. 3.8(b), we explore the dependence of these sidebands on the modulation power for a fixed modulation frequency, where at low powers only the carrier signal is detected, and as the power is increased the first and then additional sidebands appear in the spectrum. This sideband generation capability of the coupler could be useful for shifting the operating frequency or for frequency-domain multiplexing of microwave signals, for example for qubit control and readout.

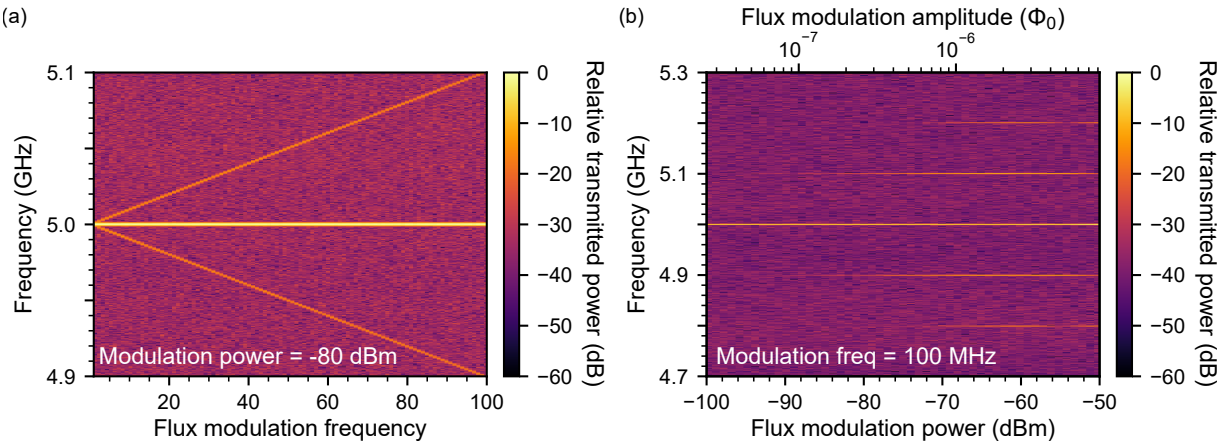

Figure 3.8: Sideband generation. (a) Measured sideband spectrum as a function of the flux modulation frequency with a constant flux modulation power of -80 dBm. The measured spectrum is normalized by the transmitted power of the carrier signal at $f = 5$ GHz. (b) Sideband spectrum as a function of flux modulation power, with equivalent modulation amplitude in units of the magnetic flux quantum $\Phi_0 = h/2e$ shown on top. The flux modulation frequency is kept constant at 100 MHz.

3.5.7 Insertion loss

The insertion loss of the variable coupler is measured by normalizing the measured transmission S_{12}^a from port 2 to port 1 with port 2 set to maximum transmission and port 3 set to minimum transmission. This measurement was then compared with a reference measurement S_{12}^b made in a subsequent cool-down by removing the device and connecting the port 2 and port 1 microwave lines directly to one another with a female/female SMA adapter. The insertion loss $L = -20\log_{10}\left(|S_{12}^a/S_{12}^b|\right)$ is then calculated as the ratio of these two transmission measurements, shown in Fig. 3.9. We observe a low insertion loss of less than 1 dB over a bandwidth of 800 MHz.

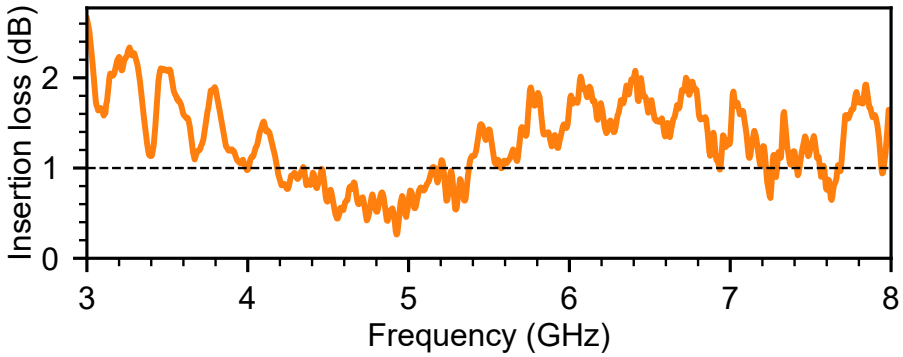

Figure 3.9: Insertion loss of the device. Dashed horizontal lines represent the 1 dB insertion loss point used to extract a bandwidth of 800 MHz.

3.6 Conclusion

In conclusion, we have presented and demonstrated a simple three-port superconducting variable coupler, using flux-biased SQUIDs operating at microwave frequencies to control the port-to-port transmission. The variable coupler has bandwidths in excess of 1 GHz, greater than 40 dB on-off coupling, and affords fast switching of a few nanoseconds. The flux tunability allows the center frequency to be set in the range of 4 to 8 GHz. The design can be easily modified to more than three ports, and can be readily integrated with superconducting qubit circuits for the routing and

modulation of individual microwave photons [66].

CHAPTER 4
REMOTE ENTANGLEMENT VIA ADIABATIC PASSAGE

4.1 Introduction

Remote entanglement of superconducting qubits has recently been demonstrated using both microwave photon- and phonon-mediated communication [18, 24, 25, 26, 27, 28]. Many of these demonstrations are limited by loss in the communication channel, due to loss in the various microwave components or intrinsic to the channel itself [18, 26, 28]; similar limitations apply to e.g. optically-based quantum communication systems. Adiabatic protocols analogous to stimulated Raman adiabatic passage (STIRAP) [67, 68] can mitigate such loss by adiabatically evolving an eigenstate of the system, using states that are "dark" with respect to the communication channel. These enable the high-fidelity coherent transfer of quantum states between sender and receiver nodes, even in the presence of large channel loss. Despite their use in a number of localized systems, such protocols have not been used for the generation of remote entangled states [67, 68].

In this chapter, we present a unique experimental system comprising a pair of superconducting Xmon qubits linked by an on-chip, 0.73 m-long superconducting microwave transmission line. By changing the coupling of the transmission line to a resistive load, we can vary the transmission line's energy lifetime T_{1r} over two orders of magnitude. We demonstrate an adiabatic protocol for quantum communication between the qubit nodes, compare its performance to a qubit-transmission mode-qubit relay method [69, 70, 27], and explore the performance of both protocols as a function of transmission loss.

We first describe the experimental device, then the two state transfer methods. We test the performance of each protocol in the low-loss limit, then as a function of transmission loss. The adiabatic process achieves significantly improved performance compared to the relay method, especially at intermediate levels of loss in the channel.[1]

1. The following is reproduced from "Remote Entanglement via Adiabatic Passage Using a Tunably Dissipative Quantum Communication System", Hung-Shen Chang, et al. *Phys. Rev. Lett.* 124, 240502 (2020), with the permission of the American Physical Society. Article is copyrighted by the American Physical Society.

4.2 Device and experimental setup

The experiment is carried out inside a dilution refrigerator with a base temperature below 10 mK. A detailed description of the experimental setup is provided in Ref. [27]. The process flow for the device fabrication is provided in Appendix A . The two quantum state transfer methods, and the device we use to test them, are shown in Fig. 4.1.

The device comprises two frequency-tunable superconducting Xmon qubits [40, 41], Q_1 and Q_2, each coupled to one end of the on-chip transmission line via an electrically-controlled tunable coupler [50], G_1 and G_2 respectively. A schematic of the device is shown in Fig. 4.1(b) and a complete circuit diagram is shown in Fig. 4.2 with detailed device parameters provided in Table 4.1.

4.2.1 Superconducting qubits

The superconducting qubits used in this experiment are frequency-tunable planar Xmon [40, 41] discussed in detail in Chapter 2. We use the qubit ground $|g\rangle$ and excited $|e\rangle$ states, whose transition frequency is tunable from $\sim$3 to 6 GHz. Microwave lines capacitively-coupled to each qubit are used to generate qubit rotations about the X and Y axes of the Bloch sphere via quadrature-resolved microwave pulses; Z-axis rotations and frequency tuning of each qubit are controlled using dc flux-bias lines inductively-coupled to each qubit's two-Josephson junction SQUID loop. To prevent spurious cross-excitations between the two qubits, the qubits are typically de-tuned from one another by 85 MHz, and each qubit's coupler G_1 (G_2) is turned off during qubit state preparation and readout. Each qubit's intrinsic qubit lifetime, coherence time, and idle frequency are provided in Table 4.1. Each qubit is read out simultaneously with the other qubit, using standard dispersive single-shot readout [71, 72, 73, 44, 45] via a capacitively-coupled quarter-wave coplanar waveguide resonator. We used a traveling-wave parametric amplifier [74] (MIT Lincoln Laboratories) to ensure nearly quantum-limited amplification of the readout signals. The $|g\rangle$ and $|e\rangle$ state readout fidelities for each qubit are shown in Table 4.1.

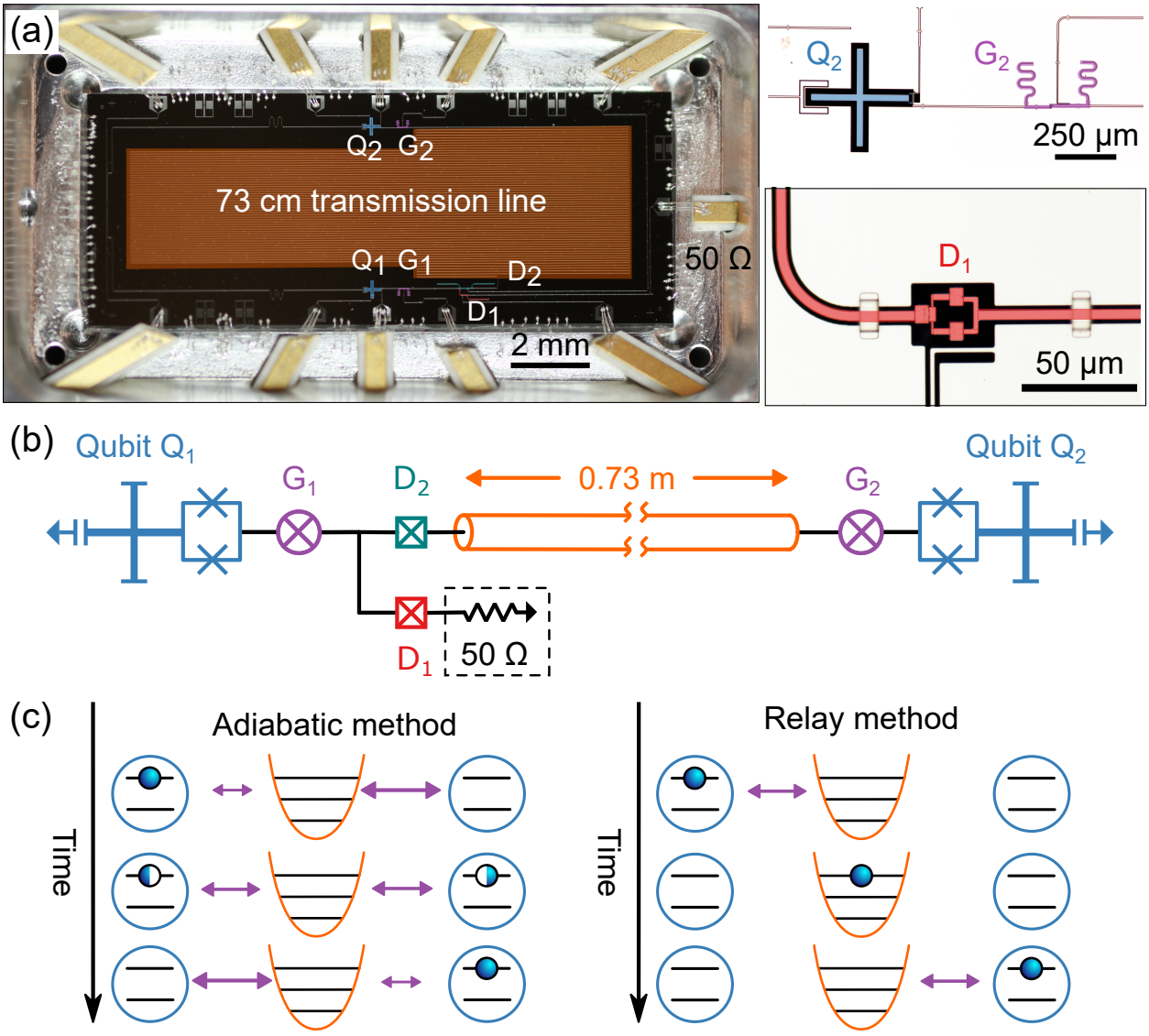

Figure 4.1: Experimental device and state transfer methods. (a) Optical micrograph of the device (left), with magnified views of one qubit and its associated tunable coupler (right top), and one variable loss coupler (right bottom). (b) A simplified circuit schematic, with two superconducting qubits (Q_1 and Q_2, blue), coupled by tunable couplers (G_1 and G_2, purple) to a 0.73 m-long superconducting transmission line (orange). The transmission line is interrupted near Q_1 by a variable coupler network. The variable coupler network comprises two tunable couplers D_1 (red) and D_2 (teal), with D_1 connected to an external $50\ \Omega$ load to ground (dashed box), while D_2 connects to the remainder of the transmission line.

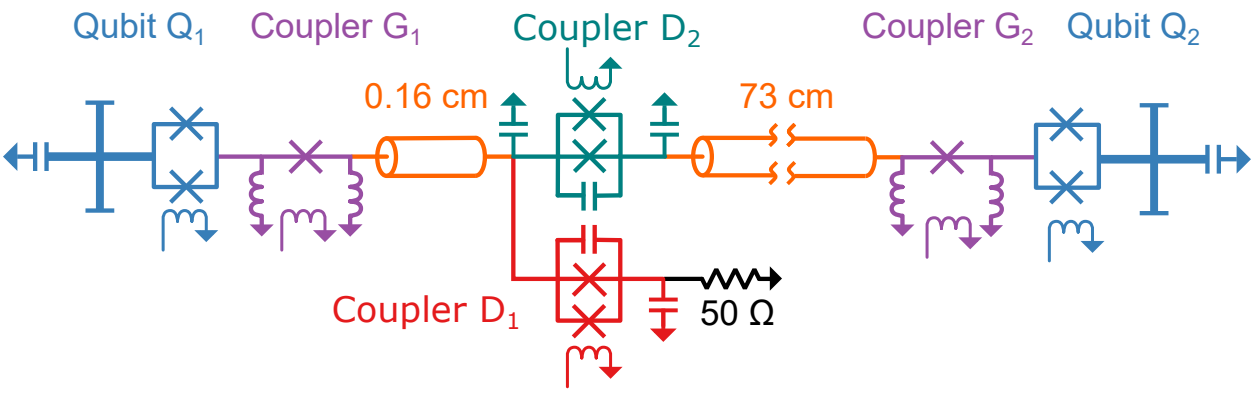

Figure 4.2: Complete circuit diagram for the experimental device. The qubits are in blue, their tunable couplers in purple, the two couplers making up the variable coupler network in teal and red, the transmission line in orange, and the $50\ \Omega$ load in black.

4.2.2 Flux-tunable couplers

The tunable coupling between each qubit and the communication channel is controlled via a galvanically-connected variable coupling π-bridge [50, 27], labeled as G_1 and G_2 in Fig. 4.1(b) and discussed in detail in Chapter 2. The tunable couplers G_1 and G_2 allow us to externally control the coupling $g_{1,2}$ of each qubit to the individual resonant modes in the transmission line. A dc flux-bias line affords flux control of each coupler by changing its Josephson junction inductance. However, changes in the coupler junction inductance induces a sympathetic frequency shift in the qubit connected to that coupler, as the inductance of the qubit is modified as well. Similarly, changes in the coupler junction inductance also shifts the transmission line frequency. With the coupler set to maximum coupling $g/2\pi = 15$ MHz, the qubit frequency is shifted by about 60 MHz, while the transmission-line resonant mode frequency is shifted by about 4 MHz. The shift in the transmission line resonant modes is much smaller, due to the transmission line's relatively large lumped inductance (Eq. 4.2) compared to the inductance of the qubit. Detailed calculations on the coupler-induced frequency shifts can be found in the supplementary of an earlier publication [27].

4.2.3 Variable coupler network

A variable control consisting of two additional tunable couplers, D_1 and D_2, is integrated into the transmission line, 1.6 mm from the coupler G_1 and its associated qubit Q_1. These are the variable couplers discussed in Chapter 3 and are used to electrically-controlled coupling between its input port and two output ports [75]. The coupler D_2 is placed inline with the transmission line leading to the tunable coupler G_2 and qubit Q_2 and is always set to provide maximum coupling (and minimal reflection) to the remaining length of transmission line. Specifically, D_2 is set to zero flux and it does not play any further role in this particular work. The SQUID bias of D_2 is not specially adjusted in the experiment. The other coupler D_1 connects to an off-chip lumped $50\ \Omega$ microwave load via a wire bond connection, yielding a variable dissipative cold load to the system. Varying the coupling to this load allows us to set the loss in the transmission line, quantified by the energy lifetime T_{1r} of each resonant mode.

Qubit parameters	Qubit 1	Qubit 2
Qubit maximum frequency, $\omega_{ge}^{max}/2\pi$ (GHz)	6.239	6.132
Qubit idle frequency, $\omega_{ge}^{idle}/2\pi$ (GHz)	5.504	5.419
Qubit capacitance, C_q (design value) (fF)	90	90
Qubit SQUID inductance, L_q (nH)	7.2	7.5
Qubit anharmonicity, $\alpha/2\pi$ (MHz)	-168	-171
Qubit intrinsic lifetime, $T_{1,\mathrm{int}}$ (μs)	11.5(5)	9.1(2)
Qubit Ramsey dephasing time, $T_{2,\mathrm{Ramsey}}$ (μs)	1.11(3)	1.15(3)
Qubit spin-echo dephasing time, T_{2E} (μs)	4.09(5)	3.54(4)
$\|g\rangle$ state readout fidelity, F_g	0.966(3)	0.959(4)
$\|e\rangle$ state readout fidelity, F_e	0.881(5)	0.888(8)
Readout resonator frequency, $\omega_r/2\pi$ (GHz)	6.361	6.415
Readout resonator quality factor, Q_r	6.9×10^3	6.4×10^3
Readout dispersive shift, $\chi_r/2\pi$ (MHz)	0.15	0.15

Flux-tunable couplers parameters	Coupler G_1	Coupler G_2
Coupler junction inductance, L_T (nH)	0.61	0.61
Coupler grounding inductance, L_g (design value) (nH)	0.2	0.2

Variable coupler network parameters	Coupler D_1	Coupler D_2
Coupler SQUID inductance, L_J (nH)	0.34	0.34
Coupler SQUID capacitance, C_J (fF)	125	125
Coupler grounding capacitance, C_g (design value) (fF)	100	100

Table 4.1: Device parameters for the two qubits, the flux-tunable couplers connecting each qubit to the channel, and the DC SQUID tunable couplers making up the variable coupler network that couples the channel to an external $50\ \Omega$ load.

4.2.4 Communication channel

The communication channel connecting the two qubits comprises a 0.73 m-long, on-chip coplanar waveguide. To suppress unwanted slotline modes, the transmission line is spanned by air-bridge crossovers every 2 mm, connecting the ground planes on either side of the transmission line [27]. The transmission line of length $\ell = 0.73$ m supports multiple resonant modes, separated in frequency by the free spectral range $\omega_{\rm FSR}/2\pi = 1/2T_\ell = 84$ MHz, where $T_\ell = 5.9$ ns is the photon one-way transit time in the channel. Each resonant standing mode n in the approximately short-circuited line can be modeled as a series RLC resonant circuit with the equivalent lumped-element parameters [30].

$$R_n = Z_0 \alpha \ell, \tag{4.1}$$

$$L_n = \frac{1}{2}\mathscr{L}\ell, \tag{4.2}$$

$$C_n = \frac{1}{\omega_n^2 L_n}, \tag{4.3}$$

where $Z_0 = 50\,\Omega$ is the characteristic impedance of the line, determined by geometry and substrate, $\alpha = 0.010$ dB/m is the (lossy) real part of the propagation parameter, determined from the intrinsic resonant mode lifetime $T_{1r,\rm int}$, $\mathscr{L} = 402$ nH/m is the inductance per unit length, $\ell = 0.73$ m is the total length, and $\omega_n = n\omega_{FSR} = n \times 2\pi\ 84$ MHz is the resonant frequency of the nth standing mode.

For sufficiently small qubit-resonator coupling, $g_{1,2} \ll \omega_{\rm FSR}$, each qubit can be selectively coupled to a single standing mode in the transmission line. This is shown in Fig. 4.3(a), where the transition frequency $\omega_{ge}/2\pi$ of qubit Q_1 is tuned over 400 MHz, yielding four separate vacuum Rabi swap resonances spaced by the free spectral range $\omega_{\rm FSR}/2\pi$. The loss coupler D_1 was set to minimum coupling, so the transmission line is limited only by its intrinsic loss. All experiments here were done with the mode at 5.351 GHz, just to the right of center in Fig. 4.3(a).

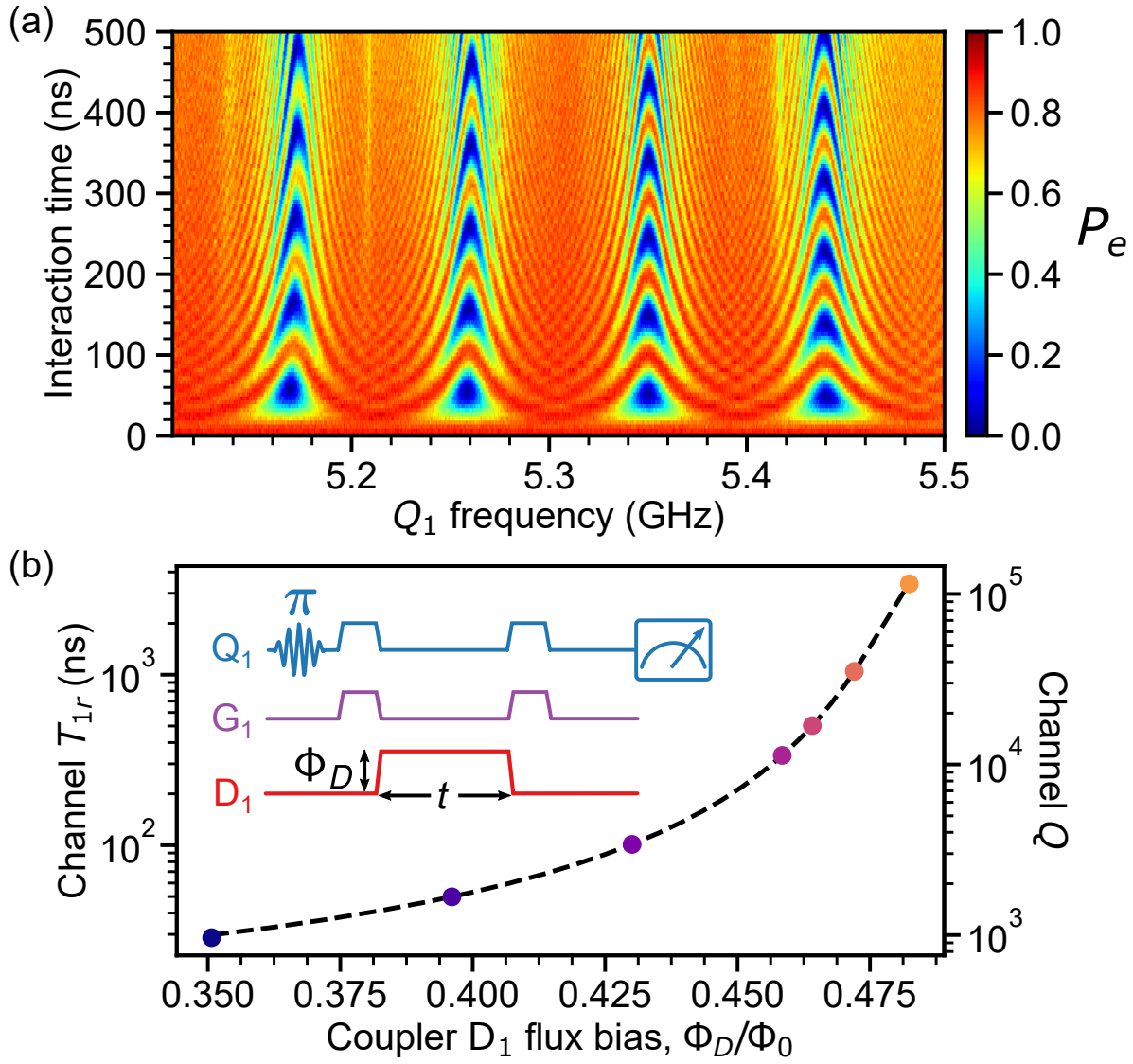

Figure 4.3: Variable loss transmission channel. (a) Vacuum Rabi swaps between qubit Q_1 and four sequential resonant transmission line modes. The coupling is set to $|g_1|/2\pi = 5.0 \pm 0.1$ MHz $\ll \omega_{\mathrm{FSR}}/2\pi$. (b) Measurement of the energy lifetime T_{1r} of one resonant mode in the transmission line, at 5.351 GHz, with equivalent quality factors Q shown on right; inset shows pulse sequence. A π pulse to qubit Q_1 puts it in the excited state, and this excitation is swapped into the resonant mode for a time t, after which it is recovered and the qubit P_e measured. The corresponding lifetime is measured as a function of transmission line loss, controlled during the lifetime measurement using coupler D_1. With D_1 turned off, we find the intrinsic lifetime $T_{1r} = 3410 \pm 40$ ns (orange); with maximum loss, we find $T_{1r} = 28.7 \pm 0.2$ ns (blue). The standard deviation of each data point is smaller than the points. Dashed lines are results calculated with a circuit model.

4.3 Strong tunable control of channel loss

In Fig. 4.3(b), we demonstrate tunable control over the channel loss, using qubit Q_1 to measure the lifetime of the resonant mode at 5.531 GHz as we vary the coupler D_1 and thus the transmission line loss. The pulse sequence for this measurement is shown inset in Fig. 4.3(b). The mode energy decay time T_{1r} for each loss setting (controlled by the D_1 flux) is shown in Fig. 4.3(b). With no coupling through D_1, we measure the intrinsic resonant mode lifetime $T_{1r} \approx 3410 \pm 40$ ns (orange), comparable to similar transmission lines without variable loss [27].

With maximum coupling to the load, we measure a lifetime $T_{1r} \approx 28.7 \pm 0.2$ ns (blue), corresponding to a loaded quality factor $Q_{\mathrm{r}} = 960$, about 120 times smaller than the intrinsic quality factor of 1.1×10^5. We also measure the resonant mode's Ramsey dephasing time T_{2r} at various D_1 flux bias points, and find $T_{2r} \approx 2T_{1r}$, indicating the coupler D_1 introduces negligible additional phase decoherence.

Non-ideality: Coupled loss

One non-ideality with this system is that qubit Q_1, due to its close proximity to the loss coupler D_1, also has its lifetime reduced when the couplers G_1 and D_1 are both set to non-zero coupling, allowing energy loss from Q_1 to the external load; this limits Q_1's performance. This is discussed in detail in the latter section of thesis. We note that this non-ideality can be avoided by placing the loss coupler D_1 in the middle of the transmission line, as the transmission line would protect both qubits from the external load. We realized this after the experiment was well under way. Fortunately, this does not affect Q_2. This is because while qubit Q_1 is almost directly coupled to the loss controller, while qubit Q2's connection is through the transmission line. The transmission line protects Q2 from this loss by acting as a filter, thus preventing Q2's states from "leaking" into the load.

4.4 Adiabatic protocol

The coupled system comprising of the two superconducting quits and the channel node and described by the coupled Hamiltonian,

$$H_{int}/\hbar = g_1(\sigma_1 a^\dagger + \sigma_1^\dagger a) + g_2(\sigma_2 a^\dagger + \sigma_2^\dagger a), \tag{4.4}$$

supports a dark eigenstate with no occupation in the channel.

We can transfer via this hybridized dark state of the coupled system. Dynamically varying the coupling allows for transfer from $Q_1 \Rightarrow Q_2$ without populating the channel in the process

We used two different communication protocols, adiabatic transfer and a qubit-resonant mode-qubit relay method. Both methods were used for qubit state transfer via the transmission line as well as Bell state generation, both as a function of loss in the communication channel. The relay method uses a single extended mode in the transmission line, swapping an excitation from one qubit into that mode and subsequently swapping the excitation from that mode to the other qubit. This method is described in detail elsewhere [27]; here it achieves an intrinsic loss-limited state transfer efficiency of $\eta = 0.95 \pm 0.01$ and a Bell state fidelity of $\mathcal{F}_s = \langle\psi^-|\rho|\psi^-\rangle = 0.941 \pm 0.005$, where ρ is the measured density matrix and $|\psi^-\rangle = (|eg\rangle - |ge\rangle)/\sqrt{2}$ is the reference Bell singlet state.

The adiabatic method uses the variable coupling of each qubit to the transmission line. When qubits Q_1 and Q_2 are set to the same frequency and couple to the same resonant mode in the channel with strengths $g_1(t)$ and $g_2(t)$, the single-excitation Hamiltonian for the system can be written in the rotating frame as

$$H/\hbar = g_1(t)\left(|e0g\rangle\langle g1g| + |g1g\rangle\langle e0g|\right) + g_2(t)\left(|g0e\rangle\langle g1g| + |g1g\rangle\langle g0e|\right), \tag{4.5}$$

where $|aNb\rangle$ corresponds to Q_1 (Q_2) in $|a\rangle$ ($|b\rangle$) with N photons in the resonant transmission line mode. This Hamiltonian supports a "dark" eigenstate $|D\rangle$ that has no occupancy in the resonant

mode,

$$|D(t)\rangle = \frac{1}{\sqrt{2}}\left(\cos\theta(t)|e0g\rangle - \sin\theta(t)|g0e\rangle\right), \tag{4.6}$$

where the mixing angle θ is given by $\tan\theta(t) = g_1(t)/g_2(t)$. With g_1 set to zero and g_2 to its maximum, the dark state is $|D\rangle = |e0g\rangle$, while exchanging the coupling values $g_1 \leftrightarrow g_2$ yields the dark state $|g0e\rangle$. By adiabatically varying the ratio $g_1(t)/g_2(t)$ in time from zero to its maximum, the system will swap the excitation from Q_1 to Q_2, without populating the lossy intermediate channel [76, 67].

Here, we implement a simple adiabatic scheme [76, 77], where we vary the couplings in time according to $g_1(t) = \bar{g}\sin\left(\pi t/2t_f\right)$ and $g_2(t) = \bar{g}\cos\left(\pi t/2t_f\right)$. We choose the parameters $\bar{g}/2\pi = 15$ MHz and $t_f = 132$ ns, minimizing the impact of finite qubit coherence while maintaining sufficient adiabaticity (see Section 4.8). We note that the adiabatic protocol supports better than 90% transfer efficiency even when $\bar{g} = 0.4\,\omega_{\mathrm{FSR}}$. This is discussed in the subsequent section.

4.4.1 Quantum state transfer via adiabatic passage

In Fig. 4.4(a), we demonstrate deterministic adiabatic state transfer from Q_1 to Q_2. With Q_1 in $|e\rangle$ and Q_1 and Q_2 set on-resonance with a single mode in the channel, we adjust the couplers G_1 and G_2 adiabatically to complete the state transfer. We show the excited state population of each qubit as a function of time t, measured with the resonant mode loss at its intrinsic minimum. We observe the expected gradual population transfer from Q_1 to Q_2, with Q_2's population reaching its maximum at $t = t_f$, with a transfer efficiency $\eta = P_{e,Q_2}(t = t_f)/P_{e,Q_1}(t = 0) = 0.99 \pm 0.01$. We further characterize the state transfer by carrying out quantum process tomography [78], yielding the process matrix χ shown inset in Fig. 4.4(a), with a process fidelity $\mathcal{F}_p = 0.96 \pm 0.01$, limited by qubit decoherence. The process matrix calculated from a master equation simulation displays a small trace distance to the measured χ matrix of $\mathcal{D} = \sqrt{\mathrm{Tr}\left([\chi - \chi_{\mathrm{sim}}]^2\right)} = 0.02 \pm 0.01$, indicating excellent agreement with experiment.

4.4.2 *Remote entanglement via adiabatic passage*

The adiabatic protocol can also be used to generate remote entanglement between Q_1 and Q_2. With Q_1 prepared in $|e\rangle$, we share half its excitation with Q_2 using the adiabatic protocol, by stopping the transfer at its midpoint $t = t_f/2$. This generates a Bell singlet state $|\psi^-\rangle = (|eg\rangle - |ge\rangle)/\sqrt{2}$. The qubit excited state population is shown as a function of time t in Fig. 4.4(b). We further characterize the Bell state by quantum state tomography [79, 80], and the reconstructed density matrix ρ is shown inset in Fig. 4.4(b). We find a Bell state fidelity $\mathcal{F}_s = \langle\psi^-|\rho|\psi^-\rangle = 0.964 \pm 0.007$, referenced to the ideal Bell singlet state ψ^-, and a concurrence $\mathcal{C} = 0.95 \pm 0.01$. The density matrix $\rho_{\rm sim}$ calculated from a master equation simulation shows a small trace distance to the measured ρ, $\sqrt{\mathrm{Tr}(|\rho - \rho_{\rm sim}|^2)} = 0.01$, indicating excellent agreement with experiment.

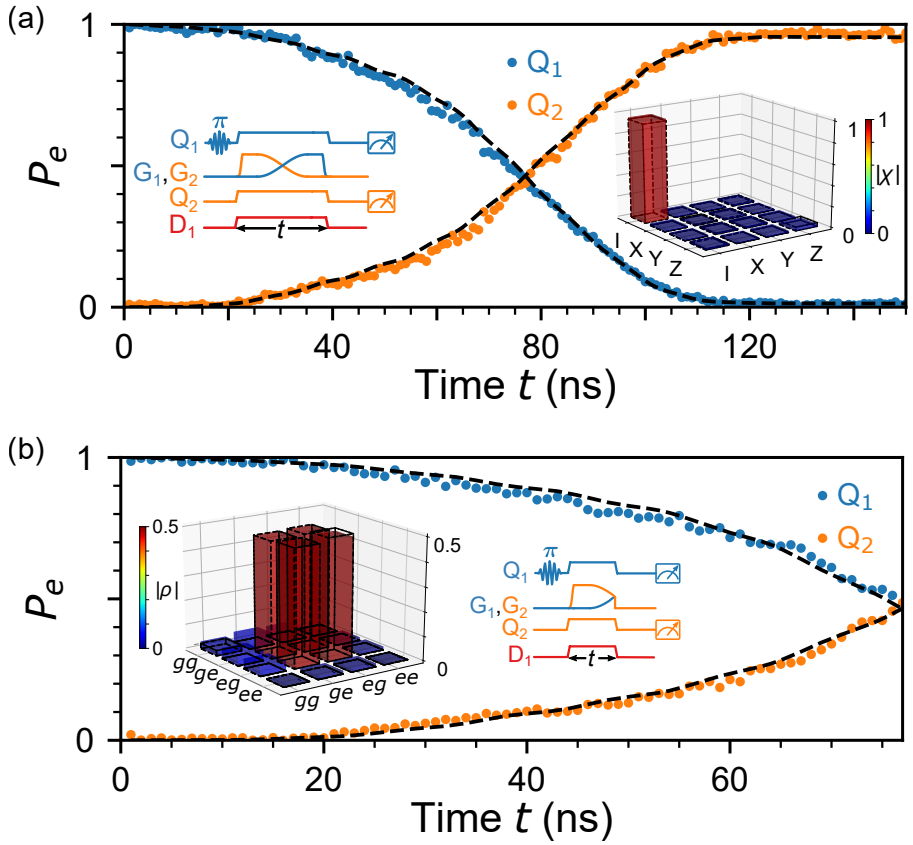

Figure 4.4: Quantum state transfer and remote entanglement using the adiabatic protocol. (a) Adiabatic state transfer between qubits Q_1 and Q_2, measured with intrinsic loss in the transmission line. Blue (orange) circles represent excited state populations of Q_1 (Q_2) measured simultaneously at time t. Left inset: Control pulse sequence. The couplers are set so that coupling g_2 starts at its maximum with g_1 set to zero. Dissipation in the resonant channel mode is controlled using D_1, here set to zero coupling. Right inset: Quantum process tomography, yielding a process fidelity $\mathcal{F}_p = 0.96 \pm 0.01$. (b) Adiabatic remote entanglement. Right inset shows control pulse sequence: With Q_1 initially prepared in $|e\rangle$, G_1 and G_2 are controlled using the adiabatic protocol to share half of Q_1's excitation with Q_2, resulting in a Bell singlet state $|\psi^-\rangle = (|eg\rangle - |ge\rangle)/\sqrt{2}$. Blue (orange) circles represent excited state populations of Q_1 (Q_2) measured simultaneously at time t. Left inset: Reconstructed density matrix of the final Bell state, yielding a state fidelity $\mathcal{F}_s = 0.964 \pm 0.007$ and concurrence $\mathcal{C} = 0.95 \pm 0.01$. In all panels, dashed lines are from master equation simulations accounting for channel dissipation and qubit imperfections (see Section 4.9).

4.5 Quantum state transfer under loss

We explore the impact of loss on both the relay method and the adiabatic protocol, with results shown as a function of the resonant channel mode energy lifetime T_{1r} in Fig 4.5. For the highest level of dissipation, with $T_{1r} = 28.7$ ns, we measure an adiabatic transfer efficiency $\eta = 0.67 \pm 0.01$, even though the transfer time t_f is four times the resonant mode lifetime. The efficiency is primarily limited by loss in qubit Q_1 due to its spurious coupling loss through D_1 to the $50\ \Omega$ load (see Section 4.9), in good agreement with master equation simulations. Results from a simulation without the spurious coupling are plotted as black dashed lines in Fig 4.5(a), limited by a small channel occupation due to the finite adiabaticity of the sequence. We compare these results to the relay method, where we use a weak coupling $|g_{1,2}|/2\pi = 5.0$ MHz to ensure the qubits only couple to a single transmission line mode; this results in a total transfer time $2\tau_{\mathrm{swap}} = 100$ ns. We find the adiabatic protocol consistently performs better than the relay method, with a $2.6\times$ higher transfer efficiency η ($2.3\times$ reduction in transfer loss) and $1.5\times$ higher process fidelity $\mathcal{F}_p$ ($2.3\times$ reduction in process infidelity) compared to the relay method in the most dissipative case; the adiabatic protocol is primarily limited by spurious coupling loss in Q_1, while the relay method is limited by loss in the channel (see Section 4.9).

4.6 Remote entanglement under loss

In Fig. 4.5(b), we display the entanglement fidelity using the adiabatic protocol with different levels of channel loss, and compare to the relay method. The adiabatic protocol outperforms the relay method in all levels of dissipation. At the highest loss level, where $T_{1r} = 28.7$ ns, the adiabatic protocol achieves $1.2\times$ higher Bell state fidelity $\mathcal{F}_s$ ($1.5\times$ reduction in Bell state infidelity) and $1.3\times$ higher concurrence $\mathcal{C}$ ($1.7\times$ reduction in concurrence infidelity) compared to the relay method; the spurious-coupling-free simulation result for the adiabatic protocol is shown by the black dashed lines, limited by a small channel occupation due to the finite adiabaticity of the sequence.

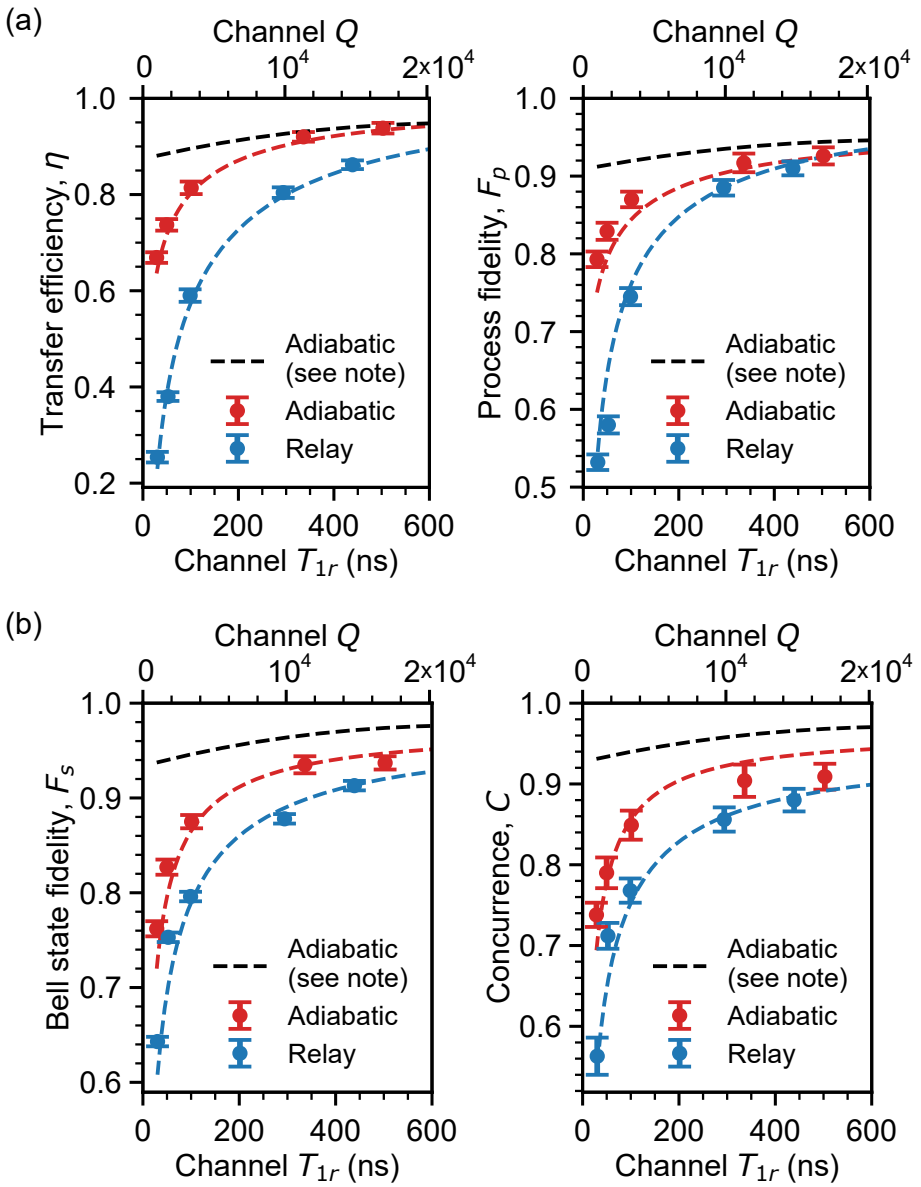

Figure 4.5: Quantum communication in the presence of channel loss, using both the relay method and adiabatic protocol. (a) Measured transfer efficiency η (left) and process fidelity $\mathcal{F}_p$ (right) for the adiabatic protocol (red) and the relay method (blue), for different resonant channel mode lifetimes T_{1r}, with equivalent quality factors Q shown on top. (b) Measured Bell state fidelity $\mathcal{F}_s$ (left) and concurrence $\mathcal{C}$ (right) for adiabatic protocol (red) and relay method (blue). In all panels, error bars are one standard deviation; red and blue dashed lines are from simulations including all sources of loss and black dashed lines are from a master equation simulation for the adiabatic protocol with no Q_1 spurious coupling loss (see Section 4.9).

4.7 Experimental methods

4.7.1 Readout correction

The qubit readout fidelities are displayed in Table 4.1. These are measured by preparing each qubit in $|g\rangle$ or $|e\rangle$ and performing measurements in the two-qubit basis, $|gg\rangle, |ge\rangle, |eg\rangle$ and $|ee\rangle$. These yield an assignment probability matrix, which is used for readout error correction through linear inversion [79, 81]. A typical assignment probability matrix is shown in Eq. 4.7. In the main text, we display the qubit excited state populations, and the quantum process and state tomography fidelities, which are all corrected for measurement errors. As shown in Table 4.2, there is a modest difference between fidelities obtained with or without these readout corrections.

$$M = \begin{bmatrix} 0.926 & 0.107 & 0.114 & 0.013 \\ 0.040 & 0.865 & 0.005 & 0.120 \\ 0.033 & 0.005 & 0.853 & 0.107 \\ 0.001 & 0.023 & 0.028 & 0.759 \end{bmatrix}. \tag{4.7}$$

4.7.2 Quantum state tomography

We carry out quantum state tomography by applying the single tomography gates $\left\{I, R_x^{\pi/2}, R_y^{\pi/2}\right\}$ and then reading out both qubits simultaneously. The density matrix is reconstructed using linear inversion to correct for measurement error and validated to ensure the resulting density matrix ρ is Hermitian, positive, and semi-definite with unit trace [79, 80]. In the experiment, Q_2's tomography pulse is rotated by a calibrated azimuthal angle φ on the Bloch sphere to account for the phase accumulated from the relative detunings of the two qubits during the transfer sequence.

4.7.3 Quantum process tomography

We perform quantum process tomography by preparing four representative single-qubit input states at the sending qubit, $\{|g\rangle, (|g\rangle + |e\rangle)/\sqrt{2}, (|g\rangle + i|e\rangle)/\sqrt{2}, |e\rangle\}$, and subsequently carrying out the state transfer protocol. At the end of the transfer, we measure the resulting density matrix for the receiver qubit via quantum state tomography, and we calculate the process fidelity through linear inversion. The process matrix is validated to ensure that it is positive, Hermitian, and semi-definite with unit trace [78]. In Table 4.2, we show the process fidelities and trace distances obtained using the adiabatic protocol for the six dissipation settings explored in the main text.

The process fidelity reflects the mapping of the density matrix for qubit 1 (the sender qubit, before the transfer) to that for qubit 2 (the receiver qubit, after the transfer). As the readout fidelities for the $|g\rangle$ and $|e\rangle$ states for the two qubits are quite similar (see Table S2), the change in the mapping for the as-measured density matrices (as reflected by the uncorrected process matrix) to the mapping for the measurement-corrected density matrices (as reflected by the corrected process matrix) is quite small, just a few percent. So in fact the smallness in the change of this fidelity is not that remarkable, as it only indirectly involves the assignment probabilities.

T_{1r} (ns)	Fidelity $\mathcal{F}_m$	Fidelity (corrected) $\mathcal{F}_c$	Trace distance $\mathcal{D}$
28.7 ± 0.2	0.77 ± 0.01	0.79 ± 0.01	0.05
49.8 ± 0.3	0.80 ± 0.01	0.83 ± 0.01	0.06
101.1 ± 0.7	0.86 ± 0.01	0.87 ± 0.01	0.03
336 ± 3	0.91 ± 0.01	0.92 ± 0.01	0.03
503 ± 5	0.92 ± 0.01	0.93 ± 0.01	0.02
3410 ± 40	0.93 ± 0.01	0.96 ± 0.01	0.02

Table 4.2: Quantum process tomography for adiabatic state transfer at each dissipation level in the channel described in the main text. The measured fidelity is calculated from $\mathcal{F}_m = \mathrm{Tr}(\chi_m \cdot \chi_{\mathrm{ideal}})$, where χ_m is the process matrix without measurement correction, and the measurement-corrected fidelity $\mathcal{F}_c = \mathrm{Tr}(\chi_c \cdot \chi_{\mathrm{ideal}})$, where χ_c is corrected for readout error. The trace distance is calculated from $\mathcal{D} = \sqrt{\mathrm{Tr}\Big([\chi_c - \chi_{\mathrm{sim}}]^2\Big)}$.

4.7.4 Concurrence

The two-qubit concurrence $\mathcal{C}$ of the Bell singlet state is calculated from the reconstructed density matrix ρ using the standard definition [82, 83]:

$$\mathcal{C}(\rho) \equiv \max\{0, \lambda_1 - \lambda_2 - \lambda_3 - \lambda_4\}, \tag{4.8}$$

where λ_i are the square roots of the eigenvalues of the matrix $\rho(\sigma_y \otimes \sigma_y)\rho^*(\sigma_y \otimes \sigma_y)$, in descending order and ρ^* is the elementwise complex conjugate of the density matrix ρ.

4.8 Theory of adiabatic state transfer

4.8.1 State transfer via the dark state

We present here the theory for the adiabatic protocol implemented in the experiments described in the main text. We assume the three quantum systems (qubit Q_1, the transmission line standing mode, and qubit Q_2), are all frequency-resonant, and we restrict the discussion to the single-excitation subspace of this system. We can write the relevant terms in the system Hamiltonian in the rotating frame of the coupled system as

$$H/\hbar = g_1(t)(|e0g\rangle\langle g1g| + |g1g\rangle\langle e0g|) + g_2(t)(|g0e\rangle\langle g1g| + |g1g\rangle\langle g0e|), \tag{4.9}$$

where $g_1(t)$ is the time-dependent coupling between qubit Q_1 and the transmission line standing mode, and $g_2(t)$ that for qubit Q_2.

Diagonalizing the Hamiltonian reveals three instantaneous eigenstates of the coupled system:

$$|B_\pm(t)\rangle = \frac{1}{\sqrt{2}}\left(\sin\theta(t)|e0g\rangle + \cos\theta(t)|g0e\rangle \pm |g1g\rangle\right), \tag{4.10}$$

$$|D(t)\rangle = \cos\theta(t)|e0g\rangle - \sin\theta(t)|g0e\rangle, \tag{4.11}$$

where the instantaneous mixing angle $\theta(t)$ is given by

$$\tan\theta(t) = g_1(t)/g_2(t). \tag{4.12}$$

The "dark" eigenstate $|D(t)\rangle$ has no occupancy in the transmission line mode and is at zero energy. The two eigenstates $|B_\pm(t)\rangle$ are the so-called "bright" states, as they include photon occupancy of the transmission line mode. These states have the eigenenergies $E_\pm = \pm\hbar\bar{g}$ respectively, where $\bar{g} = \sqrt{g_1(t)^2 + g_2(t)^2}$.

The dressed eigenstates can be revealed using qubit spectroscopy. In Fig. 4.6, with Q_2 resonant with the channel mode and with fixed couplings $g_1 = g_2$, sweeping Q_1's frequency through the channel mode frequency reveals three eigenstates separated in frequency by $g_{1,2}/2\pi$, as expected. A numerical simulation (Fig. 4.6(b)) correctly identifies the middle eigenstate as the dark state $|D(t)\rangle$, with no occupancy in the channel, with the other two eigenstates above and below $|D(t)\rangle$ identified as the two bright states $|B_\pm(t)\rangle$.

The adiabatic protocol uses the dark state $|D(t)\rangle$ to achieve the desired state transfer from Q_1 to Q_2 without populating the channel mode. This is achieved by using the sine and cosine time dependence for g_1 and g_2 respectively, as described in the main text, such that the dark state is $|e0g\rangle$ at $t = 0$ and $|g0e\rangle$ at $t = t_f$, and varies smoothly between these limits during the transfer.

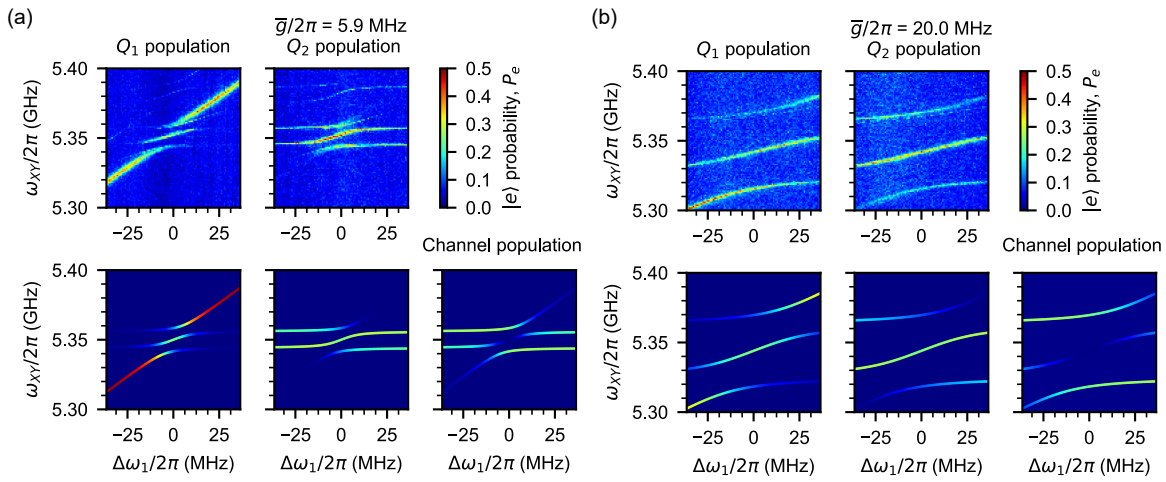

Figure 4.6: Two-qubit coupled spectroscopy near the resonant channel mode $\omega_r/2\pi = 5.351$ GHz at two coupler settings, (a) $g_1/2\pi = g_2/2\pi = 5.9 \pm 0.1$ MHz and (b) $g_1/2\pi = g_2/2\pi = 20.0 \pm 0.1$ MHz. Upper panels are experimental measurements, lower panels are numerical simulations. Q_2 is set to be resonant with the channel mode and Q_1 is biased to frequency $\omega_r + \Delta\omega_1$, where $\Delta\omega_1$ is varied along the horizontal axis. Qubit spectroscopy is carried out by driving Q_1 with a weak 5 μs-long pulse at each frequency $\omega_{XY}/2\pi$, then simultaneously measuring each qubit's excited state population P_{e,Q_1} and P_{e,Q_2} using dispersive readout [44, 45]. The two bright states are frequency-offset from the zero-energy dark eigenstate by the coupling $\pm\bar{g}/2\pi = \pm\sqrt{g_1^2 + g_2^2}/2\pi$.

4.8.2 Adiabatic condition

As the adiabatic protocol relies on remaining in the dark eigenstate throughout the transfer, the protocol needs to be executed slowly, to minimize non-adiabatic errors from coupling to the bright eigenstates. We control for this here by ensuring that integral of the two coupling functions in time satisfies [67, 84, 85, 86, 87, 88]

$$\int_0^{t_f} \bar{g}(t)\, \mathrm{d}t = \int_0^{t_f} \sqrt{g_1^2 + g_2^2}\, \mathrm{d}t \approx 4\pi, \tag{4.13}$$

which is much greater than the usual minimum threshold of $3\pi/2$ for efficient state transfer with greater than 85% efficiency [67].

We note that the simple coupling scheme adopted here keeps the effective coupling $\bar{g} = \sqrt{g_1^2 + g_2^2}$ constant, and correspondingly the energy splittings between the eigenstates are con-

stant during the transfer. This type of coupling scheme is known as a parallel adiabatic passage (PAP) and is commonly adopted in STIRAP-like adiabatic protocol, as non-adiabatic errors are minimized by avoiding anti-level crossing points during the transfer [88, 89].

4.9 Numerical model and discussion

4.9.1 Master equation model

We model the quantum behavior of the coupled system using the multi-mode Jaynes-Cummings Hamiltonian H. Our simulation model comprises two qubits (lowering operators σ_1, σ_2) coupled to $2N+1$ harmonic oscillator modes (lowering operators a_n). We can write the coupled Hamiltonian in the rotating frame of the resonant channel mode as

$$H/\hbar = \Delta\omega_1\sigma_1^\dagger\sigma_1 + \Delta\omega_2\sigma_2^\dagger\sigma_2 + \sum_{n=-N}^{N} \Delta_n a_n^\dagger a_n \tag{4.14}$$

$$+ \sum_{n=-N}^{N} g_1(t)\left(\sigma_1 a_n^\dagger + \sigma_1^\dagger a_n\right) + \sum_{n=-N}^{N} g_2(t)(-1)^n\left(\sigma_2 a_n^\dagger + \sigma_2^\dagger a_n\right), \tag{4.15}$$

where $\Delta\omega_{1,2}$ are the qubit detunings from the central resonant mode $n = 0$, $\Delta_n = n\omega_{\mathrm{FSR}}$ is the detuning of the nth channel mode from the $n = 0$ central mode, and $g_1(t)$ and $g_2(t)$ are the time-dependent couplings of Q_1 and Q_2 to the nth channel mode, assumed to be independent of n. This is justified by the high mode number (~ 64) of the resonant channel modes used; neighboring modes thus have similar coupling strength. We further note that even and odd channel modes have different signs for g_2 compared to g_1, owing to the parity of their wavefunctions $\psi_n(x)$[90, 91].

To simulate the time-domain evolution of our coupled quantum system, we numerically integrate the Lindblad master equation[92, 93] with the Hamiltonian using the python package QuTiP [94]. We account for qubit relaxation and decoherence by including the Lindblad collapse operators $\sigma_-/\sqrt{T_{1,\mathrm{int}}}$ and $\sigma_z/\sqrt{2T_\phi}$, where $1/T_\phi = 1/T_{2,\mathrm{Ramsey}} - 1/2T_{1,\mathrm{int}}$. The energy lifetime of the channel modes T_{1r} is taken to be identical for all oscillator modes and is accounted for by the Lindblad collapse operators $a_n/\sqrt{T_{1r}}$. Qubit parameters are obtained from independent qubit

measurements, while T_{1r} is obtained using the method outlined in Fig. 2 of the main text. The numerical simulations include $2N + 1 = 5$ modes, each containing two Fock states $|0\rangle$ and $|1\rangle$. The coupling functions $g_{1,2}(t)$ are varied dynamically in time using the coupling described in Fig. 3 of the main text. We use this model to simulate the time evolution of Q_1 and Q_2 in Fig. 3 of the main text as well as to obtain the expected process and Bell state fidelities, which account for the finite qubit lifetime and coherence (Fig. 3, 4).

4.9.2 Adiabatic protocol in the strong multi-mode coupling regime

Using the master equation model (see above), we explore the performance of our adiabatic protocol as it approaches the strong multi-mode coupling regime, where the coupling between the qubit and the channel mode is of order the free spectral range ($\bar{g} \sim \omega_{FSR}$). We quantify the performance of the protocol by calculating the maximum transfer efficiency η attainable at each effective coupling $\bar{g}$. The results of the simulations are shown in Fig 4.7. This simulation includes $2N + 1 = 15$ channel modes, each containing two Fock states $|0\rangle$ and $|1\rangle$. We did not perform numerical simulations for $\bar{g}/\omega_{FSR} > 1$, as this requires including more than 17 channel modes in the coupled Hamiltonian in Eq. (4.14) for accurate simulations, consuming significant computational resources for the resultantly large Hilbert space.

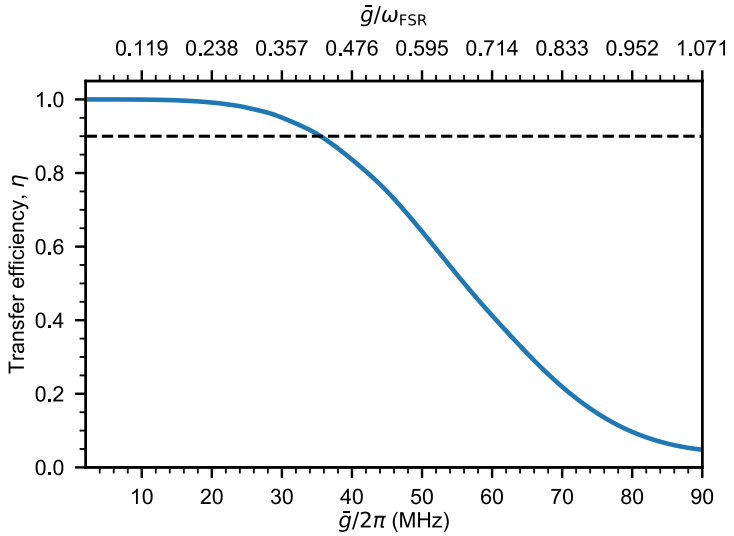

Figure 4.7: Calculated maximum transfer efficiency η as a function of the coupling strength $\bar{g}$. In the numerical simulation, the free spectral range of the channel is kept fixed at $\omega_{FSR}/2\pi = 84$ MHz, while the effective coupling strength $\bar{g}$ is varied. For coupling strengths $\bar{g}/2\pi \gtrsim 36$ MHz, interference effects from interactions with neighboring resonant modes become significant, reducing the transfer efficiency attainable with the adiabatic protocol. Dashed line marks where $\eta = 90\%$.

4.9.3 *Spurious coupling of Q_1 to the external load*

The primary source of infidelity for the adiabatic protocol is the reduced lifetime of Q_1 when the couplers G_1 and D_1 are both turned on, as this couples both the channel mode and the qubit to the external $50\ \Omega$ load. In the ideal case, this coupler only changes the loss in the channel; however, due to the close proximity of Q_1 to this coupler in the circuit, the qubit is also coupled to the $50\ \Omega$ load. This can be understood by the simplified circuit model shown in Fig. 4.8(a): When Q_1 is exactly resonant with the channel mode, the series resonance presented by the channel (represented by the series $L_r - C_r$ in the diagram) shorts the parallel load resistance $R_{L,\text{eff}}$, so there is little to no effect on the qubit. Conversely, a slight detuning of the qubit from this resonant frequency increases the $L_r - C_r$ impedance, so the external load is no longer exactly shorted and can load the qubit. This substantially reduces Q_1's T_1 lifetime when the coupler to the load is turned on. We model this effect by first calculating the effective external load $R_{L,\text{eff}}$ at each dissipation settings in the channel mode

$$\frac{1}{T_{1r,\text{ext}}} = \frac{1}{T_{1r}} - \frac{1}{T_{1r,\text{int}}}, \tag{4.16}$$

$$R_{L,\text{eff}} = \frac{L_r}{T_{1r,\text{ext}}}. \tag{4.17}$$

Next, we calculate the equivalent impedance $Z(\Delta\omega_1)$ as seen by the qubit as a function of detuning from the channel mode (Fig. 4.8(b)). The loaded qubit lifetime T_1 is then given by:

$$T_1 = L_q/\text{Re}[Z(\Delta\omega_1)]. \tag{4.18}$$

In Fig. 4.8(c,d), we show the calculated energy relaxation time T_1 of Q_1 due parasitic coupling to the external load at the largest loss case explored here ($T_{1r} = 28.7$ ns) using circuit parameters listed in Table 4.1. In Fig. 4.8(c), we see that for the coupling $|g_1|/2\pi = 15$ MHz, a 0.4 MHz frequency detuning can reduce Q_1's T_1 to 500 ns. We further show the coupling strength dependence of this effect assuming a constant detuning in Fig. 4.8(d). The relaxation of Q_1 for each dissipation

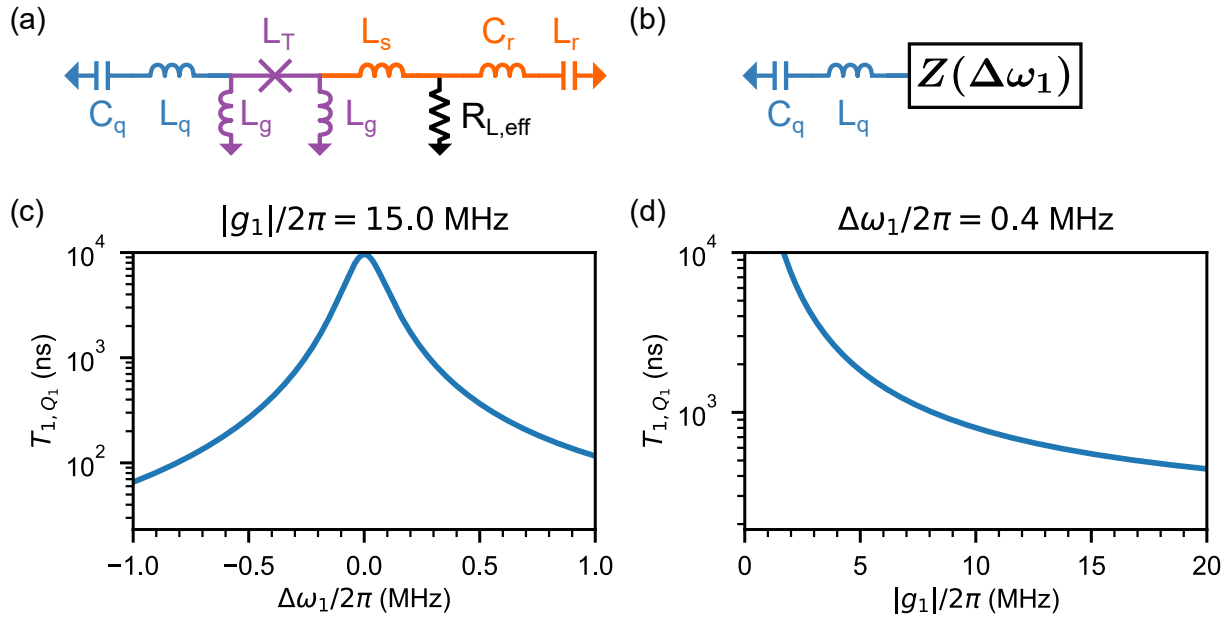

Figure 4.8: (a) Electrical circuit for calculating the parasitic loading of Q_1 from the external 50 Ω load. The qubit is represented by the series $C_q - L_q$; the coupler by the π bridge circuit $L_g - L_T - L_g$; the short length of transmission line to the load $R_{L,\mathrm{eff}}$ by L_s; and finally the lumped model for the channel resonant mode is represented by the series $L_r - C_r$. We then transform the right-half of the circuit to an equivalent impedance $Z(\Delta\omega_1)$ as seen by the qubit (b). We use this circuit model to calculate the loaded energy relaxation times of Q_1 as a function of both detuning from the channel mode $\Delta\omega_1$ and coupling $|g_1|$ using circuit parameters listed in Table 4.1. (c) Calculated Q_1 relaxation times as a function of detunings from the resonant mode for the largest dissipation case ($T_{1r} = 28.7$ ns) and with coupling $|g_1|/2\pi = 15$ MHz. (d) Calculated Q_1 relaxation times as a function of coupling $|g_1|$ assuming a constant detuning of 0.4 MHz from the resonant mode.

setting due to this parasitic coupling has been included in the simulation.

A possible way to overcome this non-ideality and increase the transfer efficiency of the adiabatic protocol further is to decrease the total transfer time t_f, reducing the impact of loss from Q_1. However, this comes at the cost of populating the channel mode during the transfer, as a result of the reduced adiabaticity. We explore these trade-offs for the largest dissipation case explored here using the master equation model with actual device parameters outlined in Table 4.1. In Fig. 4.9, we show that a maximum transfer efficiency of $\eta = 0.73$ is possible with a $t_f = 66$ ns, 0.06 higher than the efficiency achieved in the experiment in the largest loss case, where $T_{1r} = 28.7$ ns, with a total transfer time of $t_f = 132$ ns. We also note that in Fig. 4.9, our choice of $t_f = 132$ ns in

the experiment is a local maximum; this is not coincidental and is expected from theory. The time corresponds to the periodic return of the dark state at discrete times $t_f = (2\pi/\bar{g})\sqrt{n^2 - (1/4)^2}$ for non-zero integer n [77]. For $\bar{g}/2\pi = 15$ MHz, our choice of total transfer time $t_f = 132$ ns is the $n = 2$ case.

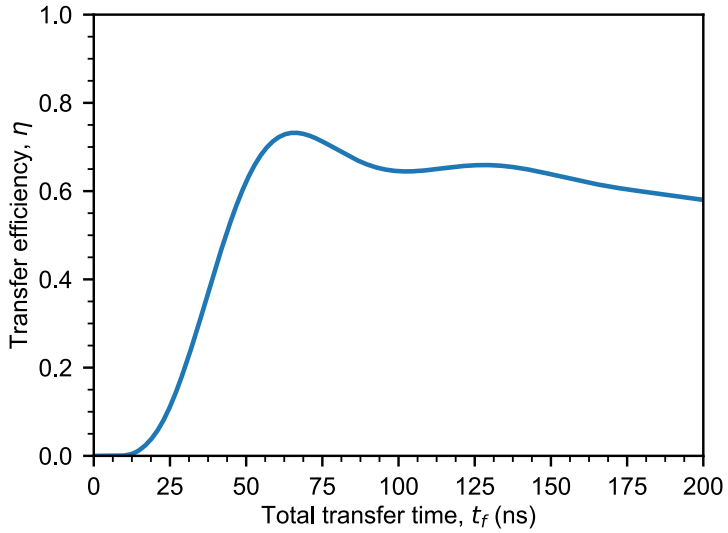

Figure 4.9: Calculated maximum transfer efficiency as a function of transfer time t_f for the largest loss case explored in the experiment, where $T_{1r} = 28.7$ ns. A maximum transfer efficiency of 0.73 occurs at transfer time of $t_f = 66$ ns, 0.06 higher than the efficiency achieved in the experiment with $t_f = 132$ ns.

4.10 Comparing with the itinerant method

The adiabatic method and the relay method used in this experiment are both quite distinct from the "itinerant method" we used in our previous work, Ref. [27]. The adiabatic and relay methods both involve a single extended resonant mode in the weakly-coupled transmission line, where the relay method swaps excitations via the tunable couplers to complete a transfer; the weak coupling makes the extended modes separately addressable. The itinerant method, on the other hand, operates in the very strong coupling regime, where the extended modes involved in the other methods are no longer resolved, and instead state transfers from the qubits are via multiple extended modes simultaneously, allowing spatial localization of the itinerant photon as it travels through the transmission line. We were unfortunately not able to reach this very strong coupling regime in this experiment, and would otherwise have indeed made comparisons to that method.

4.11 Additional quantum state transfer and remote entanglement measurements

In Fig. 4.10–4.13, we show additional measurements similar to those shown in Fig. 4.4 above, for other dissipation settings in the channel mode. These measurements were made using both the adiabatic protocol and the relay method. Results from a master equation simulation, accounting for channel dissipation as well as qubit imperfections are shown as well.

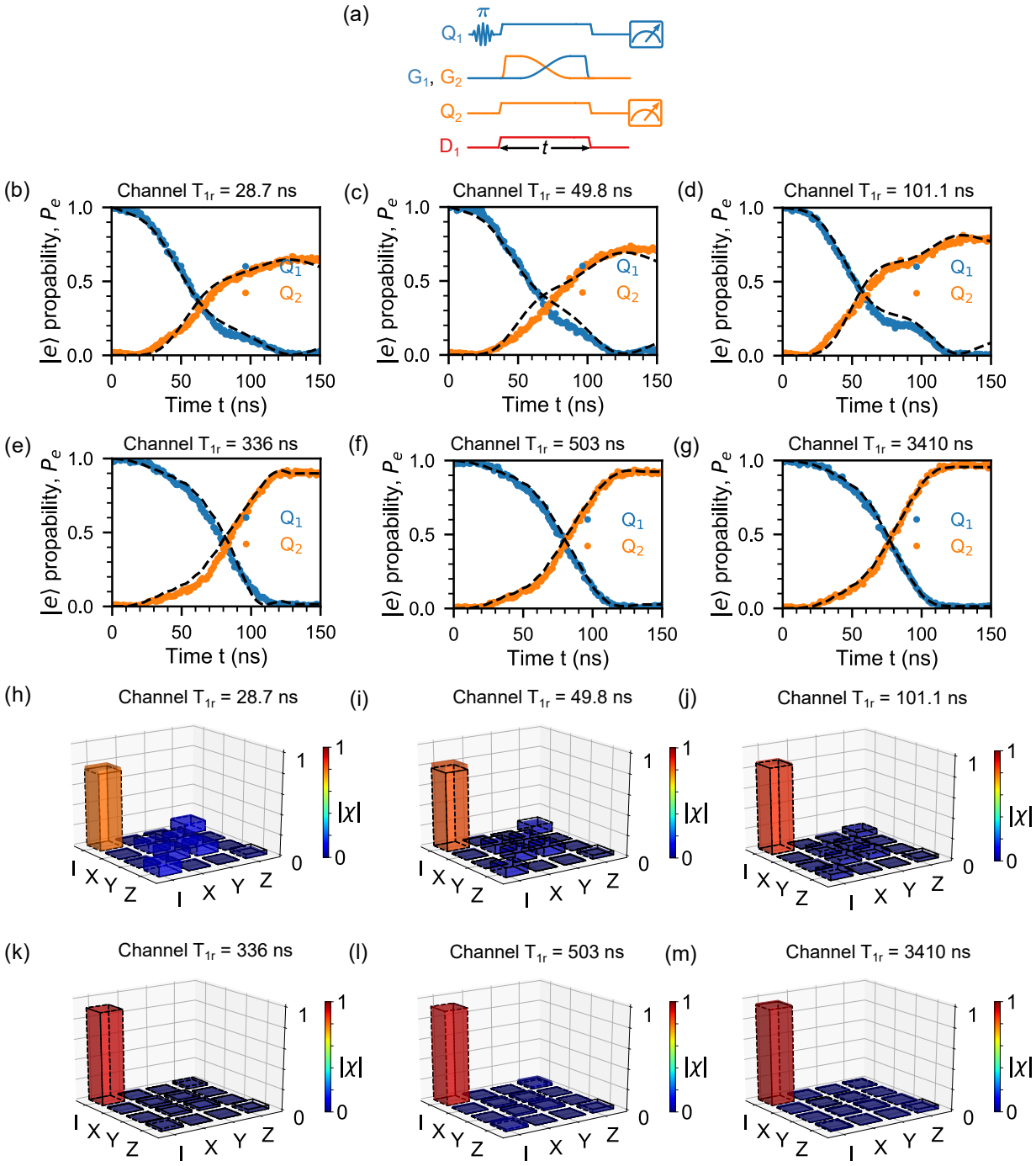

Figure 4.10: Additional quantum state transfer measurements using the adiabatic protocol. (a) Control pulse sequence. (b-g) Adiabatic state transfer between qubits Q_1 and Q_2, measured with different dissipation settings for the resonant channel mode, quantified by the resonant mode lifetime T_{1r}. Blue (orange) circles represent simultaneously measured excited state populations of Q_1 (Q_2) at time t. (h-m) Quantum process tomography at the maximum transfer efficiency point for each dissipation setting in panels b-g. In all panels, dashed lines are the results from master equation simulations, accounting for channel dissipation and qubit imperfections.

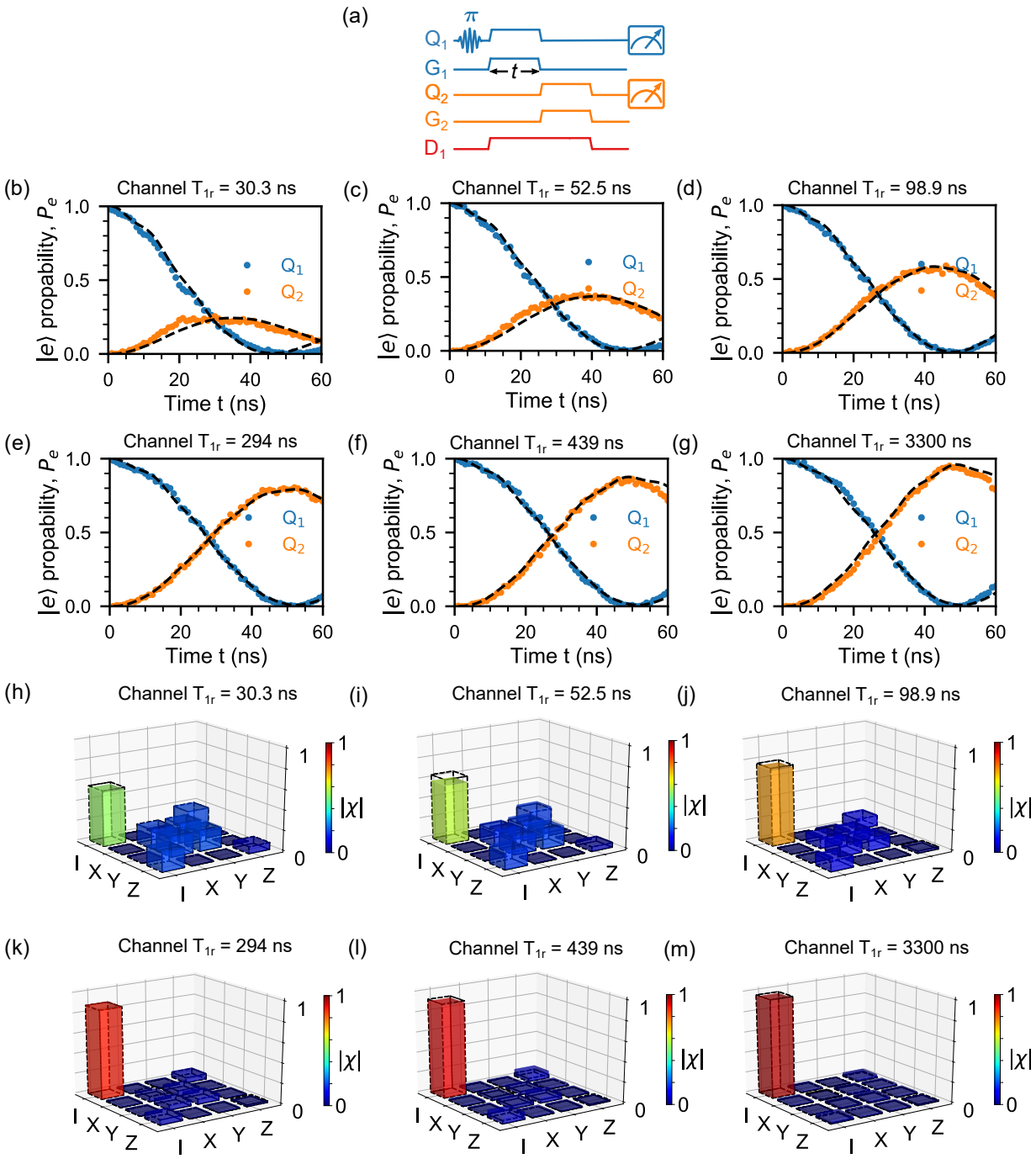

Figure 4.11: Additional quantum state transfer measurements using the relay method. (a) Control pulse sequence. (b-g) Quantum state transfer from Q_1 to Q_2 using the resonant channel mode as a relay, measured with different dissipation settings for the resonant channel mode, quantified by the resonant mode lifetime T_{1r}. Blue (orange) circles represent simultaneously measured excited state populations of Q_1 (Q_2) versus swap time t. (h-m) Quantum process tomography at the maximum transfer efficiency point for each dissipation setting in panels b-g. In all panels, dashed lines are the results from master equation simulations, accounting for channel dissipation and qubit imperfections.

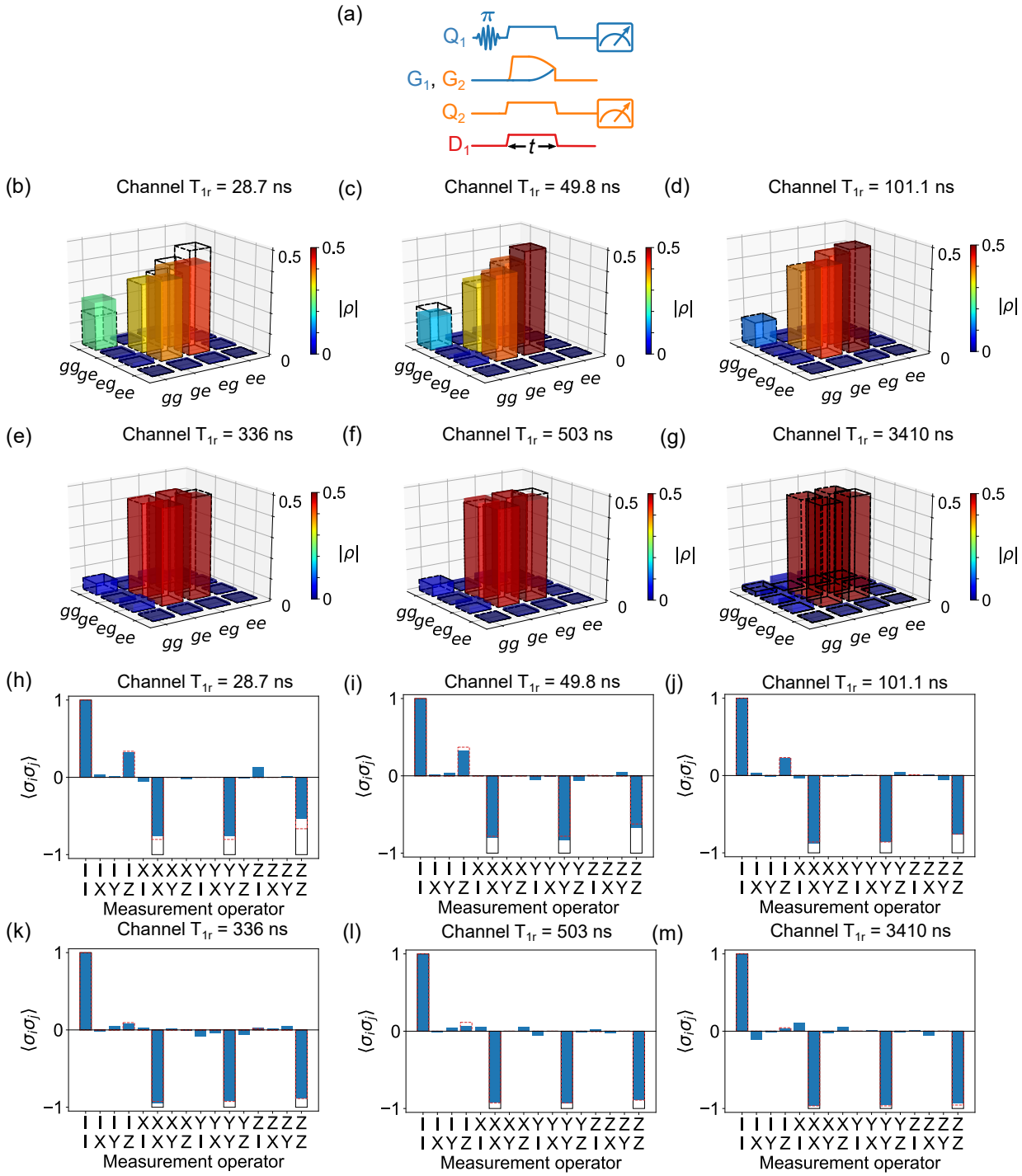

Figure 4.12: Additional remote entanglement measurements using the adiabatic protocol. (a) Control pulse sequence. (b-g) Reconstructed density matrix of the Bell states generated using the adiabatic protocol, measured with different dissipation settings for the resonant channel mode, quantified by the resonant mode lifetime T_{1r}. (h-m) Expectation values for the two-qubit Pauli operators $\langle \sigma_i \sigma_j \rangle$ for the Bell state density matrix in panels b-g. Solid lines show the expectation values for the ideal Bell singlet state $|\psi^-\rangle = (|eg\rangle - |ge\rangle)/\sqrt{2}$. In all panels, dashed lines are the results from master equation simulations, accounting for channel dissipation and qubit imperfections.

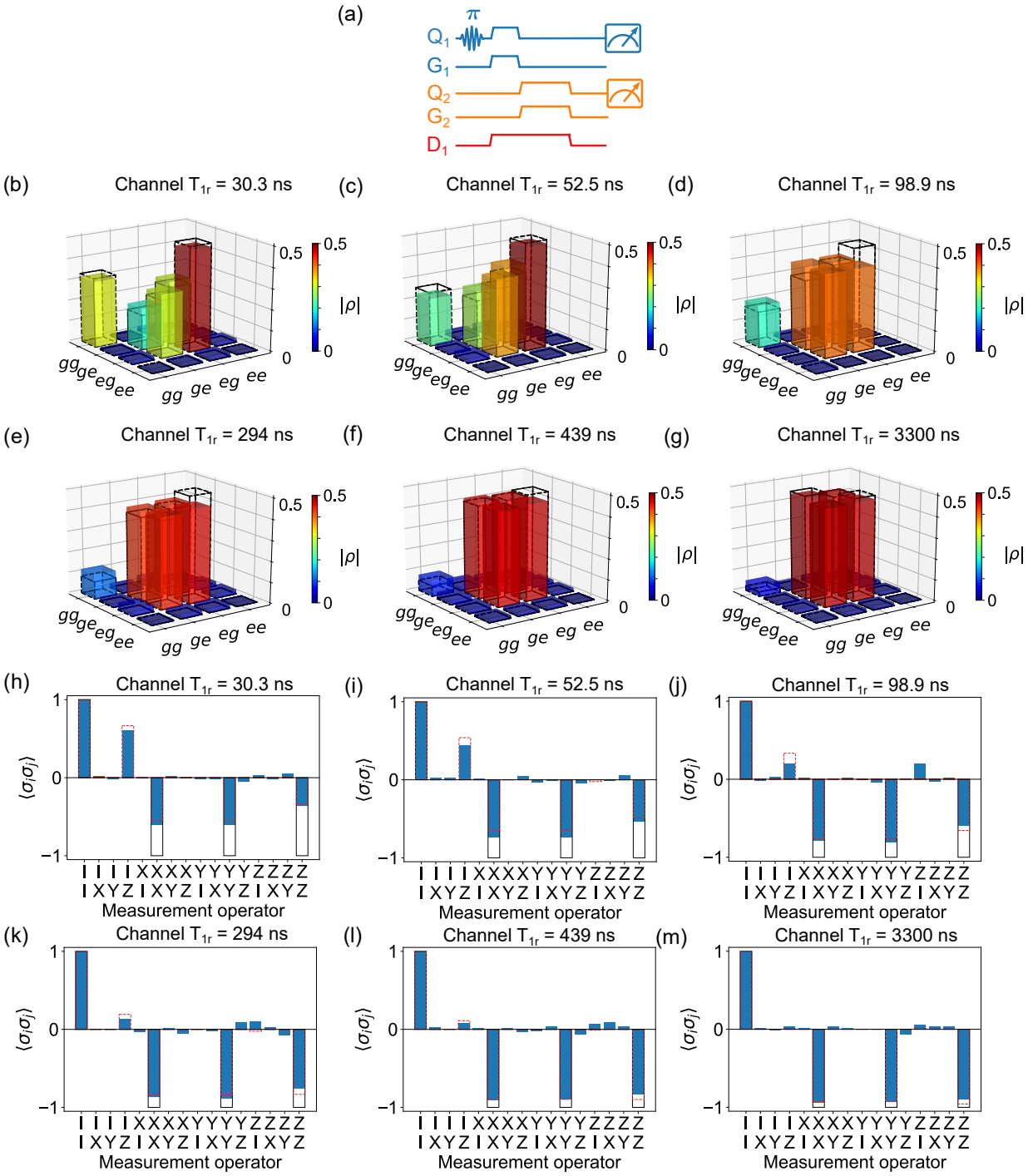

Figure 4.13: Additional remote entanglement measurements using the relay method. (a) Control pulse sequence. (b-g) Reconstructed density matrix of the Bell states generated with the relay method, measured with different dissipation settings for the resonant channel mode, quantified by the resonant mode lifetime T_{1r}. (h-m) Expectation values for the two-qubit Pauli operators $\langle \sigma_i \sigma_j \rangle$ for the Bell state density matrix in panels b-g. Solid lines show the expectation values for the ideal Bell singlet state $|\psi^-\rangle = (|eg\rangle - |ge\rangle)/\sqrt{2}$. In all panels, dashed lines are the results from master equation simulations, accounting for channel dissipation and qubit imperfections.

CHAPTER 5
CONCLUSION

Here we conclude by summarizing the main result of this thesis and discussing other applications for the superconducting quantum communication system we have developed.

5.1 Summary

In this thesis, we describe a unique experimental system in which we can explore the performance of quantum communication protocols in the presence of controllable communication loss. We demonstrate an adiabatic protocol that realizes high-fidelity transfer of quantum states and generation of entangled Bell states, limited mostly by spurious coupling of one qubit to the controlled transmission line loss. The adiabatic protocol protects against channel loss, enabling us to generate high fidelity entangled state through a lossy channel.

5.2 Outlook

The platform we have developed is well-suited to explore the impact of channel loss on other error-protecting quantum communication protocols, such as heralding [95, 96, 97] and entanglement distillation [98, 99, 100]. The ability to introduce controlled loss dynamically into the system opens the door to study dissipative dynamics in non-equilibrium systems, enabling approaches such as reservoir engineering [101, 102]. The adiabatic protocol demonstrated here is applicable to other quantum communication systems, for example phonon-based systems where the communication channel is significantly more lossy [103, 104, 28]. Future demonstrations could employ more advanced adiabatic protocols such as shortcuts to adiabaticity [105, 106] and composite adiabatic passage [107, 108] to further improve fidelity.

The adiabatic protocol demonstrated here is by no means limited to a single chip. The fact that the work in this thesis is confined to a single chip is simply because this allows us to more easily fabricate a device with which new physics can be explored without engaging in all the complexities

associated with a multi-chip arrangement. In fact, the on-chip long transmission line can be easily replaced with a superconducting coaxial cable [109] or a flexible cable [110]. The protocol we used here could certainly be extended to a multi-chip platform, using a separate microwave cable to link the chips. This kind of experiment however presents additional challenges to the technical complexity of the experiment, although from a practical point of view such approaches will likely become more common.

We expect that in these kinds of multi-chip, multi-cable experiments, the adiabatic protocol will play an even more important role than here, as it can significantly suppress the impact of cable loss. Here we provide evidence that this method is indeed viable in this sense, even in the presence of very significant loss. For inter-chip remote entanglement generation, we foresee that once the loss in the channel is alleviated by an adiabatic process, as we have shown is possible here, the main limitation will be set by the coherences of the qubits in the nodes. In these cases, other methods such as dressed state engineering [111, 112] can be used to further improve coherences.

APPENDIX A

FABRICATION

In this chapter, we describe the fabrication process flow for the devices in this thesis. The process flow is adopted from UCSB following Ref. [43, 42, 49]. It has evolved over the past few years with for example the inclusion of components such as airbridges. The fabrication process is now stable and has been repeated successfully by many in the lab, as in Ref. [113, 32, 27, 114, 28, 115, 66, 116]. All the fabrication of the samples detailed in this thesis were realized at the Pritzker Nanofabrication Facility (PNF), an ISO Class 5 cleanroom at the University of Chicago.

A.1 Fabrication process flow

1. Base layer
   (a) Al deposition following Section A.2.1.
   (b) Optical lithography following Section A.4.1.
   (c) Al etch following Section A.5.1.
2. SiO_2 scaffold for airbridges
   (a) Optical lithography following Section A.4.2.
   (b) SiO_2 deposition following Section A.2.2.
   (c) Liftoff following Section A.6.3
3. Top Al for airbridges
   (a) Optical lithography following Section A.4.2.
   (b) Top Al deposition following in Section A.2.3.
   (c) Liftoff following Section A.6.3.
4. Au alignment marks for e-beam lithography
   (a) Optical lithography following Section A.4.1.
   (b) Ti/Au deposition following Section A.2.4.
   (c) Liftoff following Section A.6.3.
5. Dice wafer into 30 mm x 42 mm pieces following Section A.6.4.
6. Josephson junctions
   (a) Dolan bridge fabrication following Section A.3.1.
   (b) Double-angle deposition of Al junctions following Section A.3.2.
7. Bandage Al for Josephson junctions
   (a) Optical lithography following Section A.4.1.
   (b) Top Al deposition following Section A.2.3.
   (c) Liftoff following Section A.6.3.

8. Perform DC measurement on the test junctions.
9. Airbridges release with vapor HF following Section A.5.2.
10. Dice wafer into 6 mm x 15 mm dies following Section A.6.4.

A.2 Electron beam deposition

A.2.1 Base layer Al deposition

For the base layer of the circuit, we first deposit 100 nm Al on sapphire using electron beam deposition. Aluminum is chosen as the base metal for two primary reasons: (1) High quality aluminum thin film can be readily deposited using conventional electron beam deposition systems in a clean room. In particular, high quality superconducting resonators and qubits made of e-beam evaporated aluminum on sapphire have been demonstrated [31, 41]. (2). Aluminum can be controllablely oxidized to form high quality stoichiometric oxides, suitable to be used as the insulating barrier for Josephson tunnel junctions. For the substrate of our device, we choose sapphire for its low loss tangent and good adhesion with aluminum. Recall that sapphire is Al_2O_3. We start off the fabrication process with a double side polished $430\,\mu\mathrm{m}$ thick 100 mm diameter c-plane sapphire wafer from Kyocera.[1].

1. Solvent clean following Section A.6.1.
2. Bake on a $200\,^{\circ}\mathrm{C}$ hot plate for 10 minutes.
3. Pre-condition the chamber by depositing 100 nm of Ti at 0.5 nm/s and 100 nm of Al at 0.2 nm/s using Angstrom Evo-Vac E-beam Evaporator[2].
4. Load the sample into the chamber and deposit 100 nm of Al at 0.2 nm/s (5 rpm sample rotation, 1×10^{-7} mbar base pressure).
5. Unload the sample and inspect it under the microscope.[3]

A.2.2 Scaffold SiO_2 deposition for airbridges

We fabricate airbridges on the samples following Ref. [49]. The fabrication involves two liftoff processes and a release via vapor HF in the end. Airbridges play a crucial role of grounding

1. https://global.kyocera.com/

2. https://angstromengineering.com/

3. It is best practice to inspect the sample under the microscope and take pictures at every step in the fabrication. This will make it easier to catch and debug possible mistakes in the fabrication later on.

broken ground planes patches across transmission lines without shorting the transmission lines. This reduces unwanted slotline modes on the chips which can be a source of dissipation for the qubits. The final suspended airbridges have no lossy dielectric and provide ideal connections for such purposes. We pattern airbridges with optical lithography and negative resist nLOF 2020. We utilize the natural undercut from an under-dosed negative photoresist to create the gradual ramp for the airbridges.

However, nLOF utilizes TMAH-based developer AZ 300 MIF which can etch aluminum. To protect the base aluminum during development of nLOF 2020 in AZ300 MIF, we use a bilayer process following Ref. [49]. We first spin on a layer of electron beam resist polymethyl methacrylate (PMMA) as a protection layer to protect the base aluminum when developing in AZ300 MIF. After lithography and development, we remove the PMMA protection layer underneath with downstream O_2 plasma ash, taking advantage of the high ashing selectivity of e-beam resist versus optical resist. With the pattern lithographed, we deposit $1\,\mu\mathrm{m}$ SiO_2 scaffold for the airbridges using electron beam deposition followed by a liftoff process.

1. Solvent clean following Section A.6.1.
2. Spin on 950K PMMA A2 (4500 rpm, 30 s).
3. Bake on a $160\,^{\circ}\mathrm{C}$ hot plate for 10 minutes.
4. Optical lithography with negative photoresist nLOF 2020 following Section A.4.2.
5. Inspect under the microscope.
6. Remove the PMMA protection layer by downstream O_2 ashing.
   (RF power: 300 W, O_2 flow: 200 sccm, time: 20 minutes, temperature: $70\,^{\circ}\mathrm{C}$)
7. Electron beam deposition of SiO_2 using Angstrom Nextdep E-beam Evaporator[4].
   (a) Pump the chamber overnight to achieve base pressure $< 1 \times 10^{-7}$ mbar. Chamber pressure is *critical* for proper adhesion between the deposited SiO_2 and the substrate. If chamber pressure is too high, with the substrate shutter closed, deposit Ti getter to lower the chamber pressure.

4. https://angstromengineering.com/

(b) Prior to the deposition, melt the SiO_2 pellets in the crucible by sweeping the electron beam for 5 minutes to ensure an uniformly melted source.

(c) Deposit $1\,\mu\mathrm{m}$ SiO_2 at 0.2 nm/s at an 45° angle with no substrate rotation. [5]

(d) Unload the sample and inspect it under the microscope.

A.2.3 Top Al deposition for airbridges

The airbridge fabrication is followed by a second aluminum deposition and liftoff. The 500 nm top aluminum across the SiO_2 scaffold for the airbridges and the 100 nm bandage aluminum for the Josephson junctions are deposited using electron beam deposition. The depositions are preceded by an *in situ* Ar ion mill to remove the native oxide on the base aluminum and establish galvanic connections between the deposited top aluminum and the base aluminum.

1. Solvent clean following Section A.6.1.
2. Spin on 950K PMMA A2 (4500 rpm, 30 s).
3. Bake on a $160\,^{\circ}\mathrm{C}$ hot plate for 10 minutes.
4. Optical lithography with negative photoresist nLOF 2020 following Section A.4.2.
5. Inspect under the microscope.
6. Remove the PMMA protection layer by downstream O_2 ashing.
   (RF power: 300 W, O_2 flow: 200 sccm, time: 20 minutes, temperature: $70\,^{\circ}\mathrm{C}$)
7. Electron beam deposition Al using Plassys MEB550S Electron Beam Evaporator.
   (a) Pump down for two hours (base pressure $< 1 \times 10^{-7}$ mbar).
   (b) Ar ion mill for 4 minutes to remove native oxide on the base layer Al.
      i. Beam voltage: 400 V
      ii. Accelerating voltage: 80 V
      iii. Beam current: 15 mA
      iv. Process pressure: 5×10^{-4} mbar

5. When depositing a liftoff layer, it is best practice to not rotate the substrate during deposition such that the deposited film only coats a single sidewall of the photoresist. This enables an easier liftoff.

v. Ar flow rate: 6 sccm

(c) With the substrate shutter closed, deposit Ti getter for 3 minutes at 0.2 nm/s to lower the chamber pressure.

(d) Deposit Al at 1 nm/s normal to the substrate. Deposit 500 nm of Al for the top Al for airbridges and 300 nm for bandage Al for Josephson junctions. No substrate rotation during deposition.

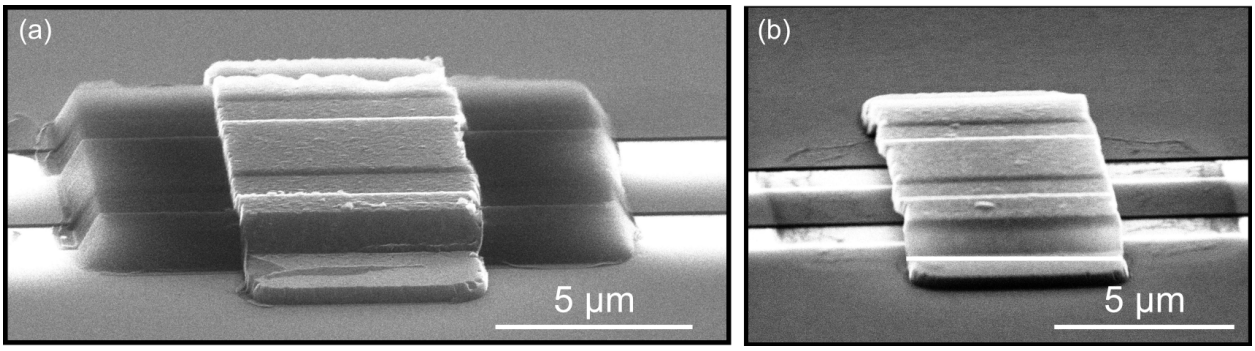

Figure A.1: (a) Scanning electron micrograph of an airbridge over a transmission line with the supporting SiO_2 scaffold (dark grey). (b) The scaffold is etched away via vapor HF (Section A.5.2) as the last step in the fabrication process resulting in a free-standing airbridge (white).

A.2.4 Ti/Au deposition for alignment marks

To align the e-beam patterning of the Josephson junctions following Section A.3 to the underlying Al base layer, we create Ti/Au alignment marks on the sample using aligned optical lithography, electron beam deposition, and liftoff. Unlike aluminum, gold has a high atomic number and thus has high contrast when viewed in the e-beam alignment system. This makes it a suitable choice as e-beam lithography alignment marks.

1. Downstream O_2 clean.

   (RF power: 50W, O_2 flow: 200 sccm, time: 10 s, temperature: $25\,^{\circ}\mathrm{C}$).

2. Inspect under the microscope.

3. Electron beam deposition of Ti/Au with no substrate rotation.

   (a) Deposit 10 nm of Ti at 0.1 nm/s

   (b) Deposit 150 nm of Au at 0.2 nm/s.

   (c) Unload the sample and inspect it under the microscope.

A.3 Josephson junction fabrication

We fabricate Josephson junctions using the standard Dolan bridge technique [36]. Following Ref. [42], we lithograph a shadow mask through a PMMA/methacrylic acid (MAA) copolymer bilayer to create a bridge of resist suspended in air. The bridge is lithographed using electron beam lithography with a Raith EBPG5000 Plus system; we do not use proximity effect correction. For the deposition of the junction, we first deposit at one angle to deposit the first electrode, oxidize the surface to create the thin insulating oxide, and deposit at the second angle to deposit the second superconducting electrode. The junction is formed at the overlapping shadow region between the two deposition layers.

A.3.1 Dolan bridge fabrication

1. Solvent clean following Section A.6.1.
2. Bake on a $115\,^{\circ}\mathrm{C}$ hot plate for 5 minutes.
3. Blow wafer with N_2.[6]
4. Spin on 500 nm thick MAA EL9 (1500 rpm, 45 s).
5. Bake on a $160\,^{\circ}\mathrm{C}$ hot plate for 10 minutes.
6. Spin on 300 nm thick PMMA 950K A4 (2000 rpm, 40 s).
7. Bake on a $160\,^{\circ}\mathrm{C}$ hot plate for 10 minutes
8. Deposit 10 nm of Au at 0.05 nm/s and 3 rpm substrate rotation using thermal evaporator. The thermally deposited gold acts as a conduction layer to prevent charging effect during lithography. Without the thermally evaporated gold, on an electrically insulating substrate like sapphire, charges from the e-beam have no path to ground. They can accumulate on the resist and deflect the incoming electron, distorting the write.
9. Write the pattern with e-beam writer with 100 kV beam voltage and 1 nA beam current. To expose just only the MAA layer for undercuts or both the PMMA and MAA layers, we

6. It is best practice to always blow wafer with N_2 before applying resist. Any dust on the surface of the wafer can hinder one from obtaining a nice smooth surface of resist.

expose with the following dosages.

(a) MAA only (for undercuts): $350\,\mu\mathrm{C/cm^2}$

(b) PMMA + MAA dose: $1500\,\mu\mathrm{C/cm^2}$

(c) Clearing dose (for contact pads): $2000\,\mu\mathrm{C/cm^2}$

The high clearing dose is to ensure complete clearing/exposure of e-beam resist at the contact area between the Josephson junction deposited later and the base wiring metal underneath. As MAA is much more sensitive to dose than the PMMA above, the low MAA dose allows us to selectively expose the MAA underneath and create the undercut for the suspended bridge (Dolan bridge) needed for shadow evaporation of the junction.

10. Strip Au in TFA gold etchant Type TFA (Transene) for 10 s.
11. DI water rinse.
12. Develop in 3:1 isopropyl alcohol (IPA):methyl isobutyl ketone (MIBK) mixture for 40 s with gentle agitation side to side, 0.5 Hz.
13. Immerse in IPA for 10 s with gentle agitation side to side, 0.5 Hz.
14. Blow dry with N_2 at 30 psi.
15. Downstream O_2 clean.

    (RF power: 50 W, O_2 flow: 200 sccm, time: 5 s, temperature: $25\,^{\circ}\mathrm{C}$).
16. Inspect under the microscope.

A.3.2 Double-angle deposition

The Josephson junction is deposited with double-angle deposition in Plassys MEB550S Electron Beam Evaporator[7]. The junction deposition is not preceded by an *in situ* Ar ion mill to avoid substrate damage beneath the deposited junction [117]. Instead, to create galvanic contact between the junctions and the base layer metal, we follow the junction deposition by an additional bandage layer. The bandages layer utilizes a similar process as the top aluminum layer for airbridges which includes an *in situ* Ar ion mill. To prevent Ar ion mill from damaging the substrate, the bandage

7. https://plassys.com/evaporation-hv-uhv/

layer only exposes a small area of the base metal layer for galvanic contact with the junction while keeping the entire substrate covered.

1. Pump down overnight in the deposition chamber (pressure $< 1 \times 10^{-7}$ mbar).
2. With the substrate shutter closed, deposit Ti getter for 3 minutes at 0.2 nm/s to lower the chamber pressure.
3. Deposit 65 nm of Al at 1 nm/s at 60° from normal to the substrate.
   ($\sim$30 nm of film deposited on the substrate)
4. Oxidize in 85/15 Ar/O_2 mixture at 30 mbar for 50 minutes.
5. Deposit 100 nm of Al at 1 nm/s normal to the substrate.
6. Oxidize in 85/15 Ar/O_2 mixture at 5 mbar for 5 minutes. This creates a controlled oxidized layer on top of the deposited junction.
7. Unload the sample and inspect it under the microscope.

A.4 Optical lithography

A.4.1 Optical lithography with positive resist AZ 703

Optical lithography of the base layer control wiring, gold alignment marks, and the bandages for the junction are done with 900 nm thick positive I-line photoresist AZ MiR 703 and exposed with a Heidelberg MLA150 Direct Write Lithographer[8]. The Direct Write Lithographer directly exposes the wafer with the laser without the use of photomask. This affords flexibility in pattern design as well as fast turnaround time. The patterned resist is then developed with a AZ MIF 300 developer. Care must be taken when using a TMAH-based developer like AZ MIF 300 as it can etch aluminum. We thus minimize the development time in our process.

1. Solvent clean following Section A.6.1.
2. Bake on a $115\,^{\circ}\mathrm{C}$ hot plate for 5 minutes.
3. Blow wafer with N_2.
4. Spin on 900 nm thick AZ MiR 703 (4500 rpm, 30 s).
5. Soft bake on a $90\,^{\circ}\mathrm{C}$ hot plate for 1 minute.
6. Optical lithography with Heidelberg MLA150 Direct Write Lithographer.
   (a) Critical dimension bias: -200 nm[9]
   (b) Exposure time: $100\,\mathrm{mJ/cm^2}$ (varied, depending on the material underneath)
   (c) Laser: 375 nm
7. Post-exposure bake on a $115\,^{\circ}\mathrm{C}$ hot plate for 1 minute. Put the wafer in the center of the hot plate.[10]
8. Let the sample sit for 1 minute.

8. https://heidelberg-instruments.com/en/products/mla150.html

9. Under biasing (shrinking) the design increases the process latitude of the exposure. See Ref. [118] for a detailed discussion.

10. It is best practice to put the wafer in the center of the hot plate whenever possible. We have observed temperature gradient $\pm\,5\,^{\circ}\mathrm{C}$ across the hot plate surface. Thus, it is best to put the sample at a consistent location on the hot plate across different fabrication runs for consistent fabrication.

9. Develop in AZ MIF 300 developer with gentle agitation side to side, 0.5 Hz, for 1 minutes.
10. Immerse in DI water with gentle agitation side to side, 0.5 Hz, for 30 s.
11. Run DI water down the wafer, rinsing each die for ~ 1 s.
12. Blow dry with N_2 at 45 psi.
13. Inspect under the microscope.

A.4.2 Optical lithography with negative resist nLOF 2020

This is the standard procedure for photolithography with $3\,\mu\mathrm{m}$ thick negative photoresist, nLOF 2020. Note that nLOF 2020 must be kept in the fridge at all times. Only take it out of the fridge 20 minutes before spinning the resist.

1. Bake on a $115\,^{\circ}\mathrm{C}$ hot plate for 5 minutes.
2. Blow wafer with N_2
3. Spin on $3\,\mu\mathrm{m}$ thick AZ nLOF 2020 (1500 rpm, 45 s).
4. Soft bake on a $110\,^{\circ}\mathrm{C}$ hot plate for 1 minute.
5. Aligned optical lithography with Heidelberg MLA150 Direct Write Lithographer.
   (a) Critical dimension bias: -200 nm
   (b) Exposure time: $100\,\mathrm{mJ/cm^2}$ (varied, depending on the underlying materials)
   (c) Laser: 375 nm
6. Post-exposure bake on a $110\,^{\circ}\mathrm{C}$ hot plate for 1 minutes.
7. Let the sample sit for 1 minute.
8. Develop in AZ MIF 300 developer with *vigorous* agitation left and right, 1 Hz, for 2 minutes.
9. Immerse in DI water with gentle agitation side to side, 0.5 Hz, for 30 s.
10. Run DI water down the wafer, rinsing each die for $\sim$1 s.
11. Blow dry with N_2 at 45 psi.

A.5 Dry etching

A.5.1 ICP Chlorine etch for base layer Al

Etching of the base layer Al is done via a PlasmaTherm APEX inductively coupled plasma (ICP) chlorine etcher with a BCl_3/Cl_2 etching process. We choose ICP etch over wet etch for its good etching anisotropy as well as the smooth etching surface obtained from ICP etch; see Fig. A.2.

1. Prepare a bucket of DI water next to the etcher.
2. Run a O_2 plasma clean to clean the etching chamber.
3. Preconditioning the chamber by running a test etch for 3 minutes with the following etch parameters.

ICP power	400 W
ICP bias power	33 W
Cl_2 flow	30 sccm
BCl_3 flow	30 sccm
Ar flow	10 sccm
Process pressure	5 mTorr

Table A.1: ICP chlorine etch parameters.

4. Load wafer into the etcher and run the etch for 24 s with the above etch parameters.
5. Vent the chamber. Immediately after the chamber is vented, immerse the wafer into the DI water nearby for 10 minutes to passivate residual Cl on the sample. Residual Cl can combine with H_2 in the air to form HF which can attack aluminum.
6. Blow dry with N_2 at 45 psi.
7. Inspect under the microscope.
8. Strip the photoresist following Section A.6.2.
9. Inspect under the microscope.

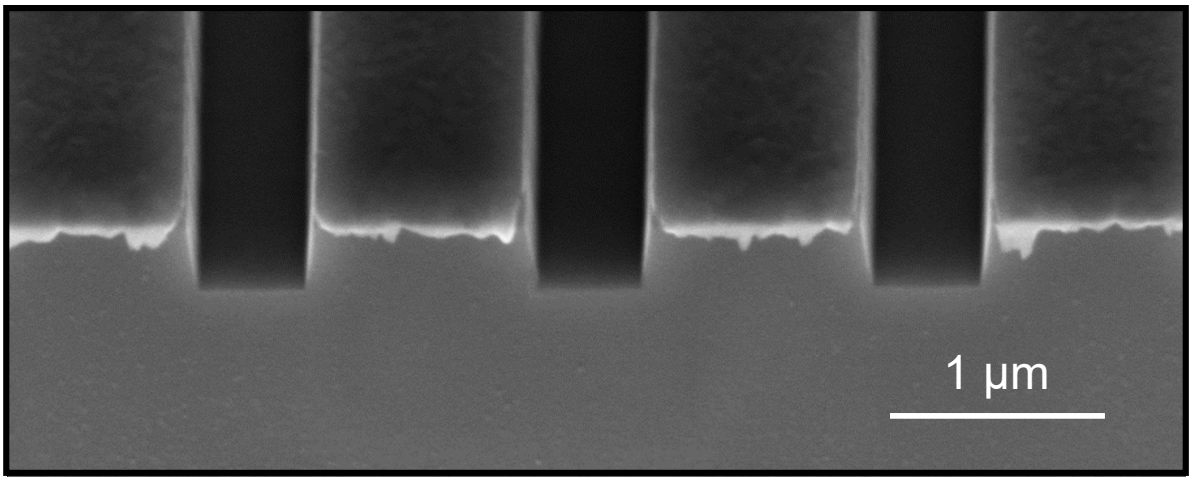

Figure A.2: Etch profile of an ICP BCl_3/Cl_2 etch. ICP etch is highly directional and can etch a near smooth vertical sidewall.

A.5.2 Airbridges release with vapor HF

The airbridges are released using a vapor HF process with the following chemical reaction:

$$SiO_2 + 4HF \rightarrow SiF_4 + 2H_2O. \tag{A.1}$$

Vapor HF does not etch aluminum, aluminum oxide, and sapphire; this process is thus compatible with the qubit fabrication. Note, this is however not the case for *hydrous* HF which can etch both aluminum and aluminum oxide. The fabricated airbridges are mechanically fragile and cannot withstand any sonication once released. Consequently, we reserve the airbridge release as the final step in the device fabrication process.

1. We release the SiO_2 scaffold of the airbridges using vapor HF in a Memsstar Orbis Alpha Oxide HF Vapor Etch system[11] with the following parameters.

11. https://memsstar.com/mems-tools/wafer-processing-system-orbis-alpha-rd/

Process pressure	15 Torr
H_2O	5 mg/min
HF flow	40 sccm
N_2 flow	20 sccm
Etch time	30 s

Table A.2: Vapor HF etch parameters.

2. Unload the sample and inspect it under the microscope.
3. Over a dish, squirt down both sides of the chip with acetone for 30 s and then immediately soak the chip in acetone in a new dish. This removes the etching residue left underneath the airbridges. Do not use sonication as airbridges are mechanically fragile and will break once sonicated.
4. Soak the chip in acetone for 5 minutes and then in IPA for another 5 minutes.
5. Blow dry with N_2 at 45 psi.
6. Inspect under the SEM.

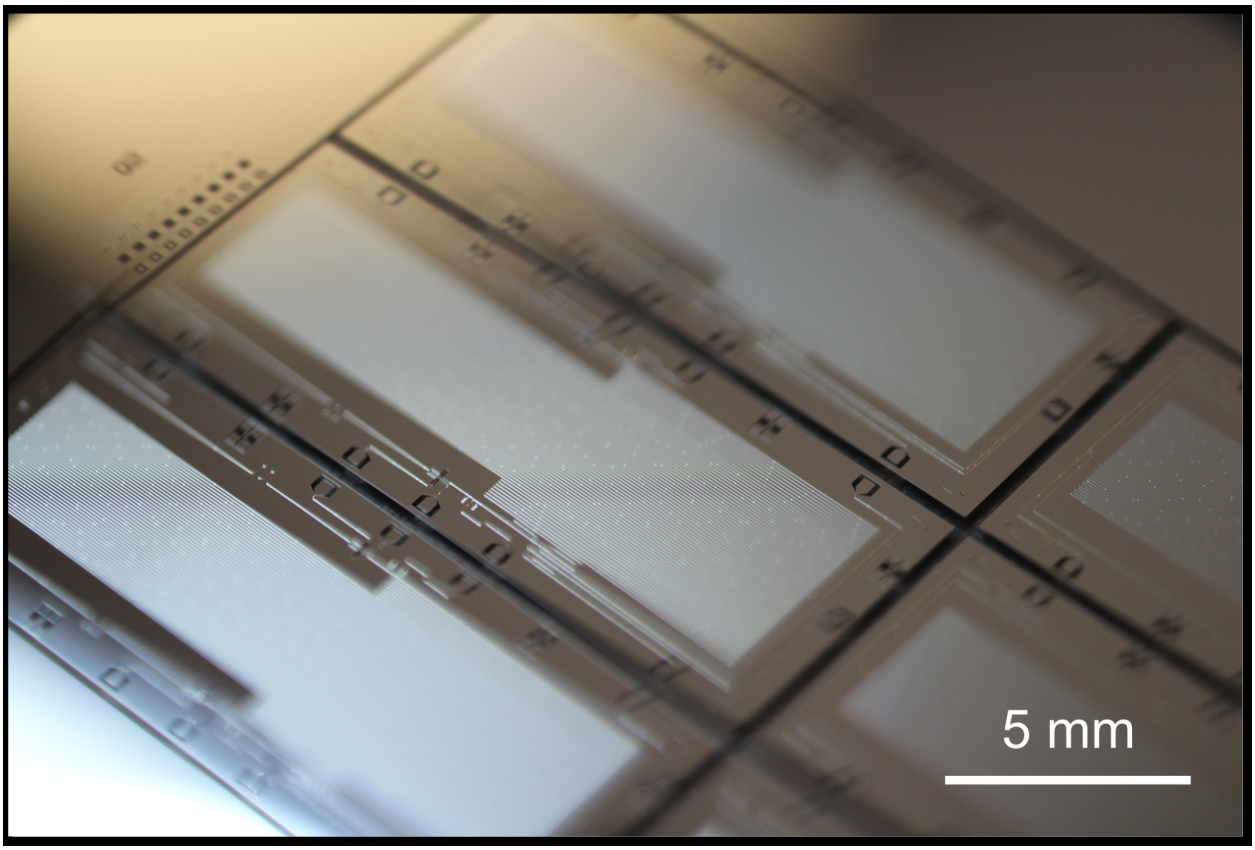

Figure A.3: Completed superconducting quantum circuits. Photograph of an array of completed devices used in Chapter 4 fabricated using this process flow. The light areas are aluminum and the dark areas are the exposed sapphire substrate which has been etched away.

A.6 Repeated processes

A.6.1 Solvent clean

The standard solvent clean involves sonication in acetone and IPA to provide a general-purpose sample clean, typically before lithography or deposition processes.

1. Acetone, sonicating at 104 kHz, 5 minutes.
2. IPA, sonicating at 104 kHz, 5 minutes.
3. Under the DI water goose neck, rinse the wafer with DI water for 30 s. Skip if there is both gold and aluminum exposed on the sample. There is an electrochemical reaction where DI water acts as an electrolyte and aluminum and gold act as electrodes that results in corrosion of aluminum.
4. Spin dry the sample completely with the spinner (3000 rpm, 30s). This is *crucial* to ensure that no residue water droplet remains on the surface of the wafer.

A.6.2 Photoresist strip

Processes such as etching are aggressive. Photoresist can be heated or cross-linked during these processes making them hard to strip via conventional methods. We have developed an aggressive photoresist strip process which involves sonication in heated NMP stripper to remove the cross-linked photoresist following such processes. The strip process is used directly after the ICP etch.

1. Downstream O_2 ashing.
   (RF power: 300 W, O_2 flow: 200 sccm, time: 4 minutes, temperature: $70\,^{\circ}\mathrm{C}$).
2. Place the sample face down in NMP and cover the dish with aluminum foil, and sonicate in $80\,^{\circ}\mathrm{C}$ heated bath.
   (a) 5 minutes at 40 kHz.
   (b) 5 minutes at 72 kHz.
   (c) 5 minutes at 104 kHz.

(d) 5 minutes at 170 kHz.

3. Remove from NMP and, over the NMP, squirt down both sides with IPA for 30 s total.
4. Immerse in an IPA bath, 5 minutes.
5. Immerse in a DI water bath, 1 minute.
6. Under the DI water goose neck, rinse the wafer with DI water for 30 s total.
7. Blow dry with N_2 at 45 psi.
8. (Optional) Additional downstream O_2 ashing.

   (RF power: 100 W, O_2 flow: 50 sccm, time: 3 minutes, temperature: $100\,^{\circ}\mathrm{C}$).

A.6.3 Liftoff

We use liftoff with optical and electron beam lithography to create airbridges and Josephson junctions, respectively. The standard liftoff process involves a long soak in heated N-methyl-2-pyrrolidone (NMP) to remove the photoresist underneath the deposited metal.[12]

1. Place sample face down in NMP covered and place in the $80\,^{\circ}\mathrm{C}$ heated bath for 4 hours.[13]
2. Remove the sample from NMP and, over the NMP, squirt down both sides with NMP for 30 s total. This should remove most of the deposited film.
3. Soak in another pre-heated NMP at $80\,^{\circ}\mathrm{C}$, 5 minutes.
4. Remove from NMP and, over the NMP, squirt down both sides with IPA for 30 s total.
5. Move the sample into a fresh IPA bath and soak for 5 minutes.
6. Move the sample into a second fresh IPA bath and soak for 5 minutes.
7. Blow dry with N_2 at 45 psi.
8. Inspect under the microscope.

12. Do not immerse carbon-tipped tweezers in heated NMP. There is a chemical reaction that results in melted tweezers and bits of plastic floating around.

13. Do not leave Josephson junctions overnight in NMP as NMP can etch Al over time, albeit at a slow rate.

A.6.4 Wafer dicing

1. Spin on $200\,\mu\mathrm{m}$ thick AZ MiR 1518 (2000 rpm, 30 s) as dicing resist to protect the sample from debris during dicing.
2. Bake on a $115\,^{\circ}\mathrm{C}$ hot plate for 2 minutes.
3. Mount the sample onto the dicing tape.
4. Dice the wafer using DISCO DAD3240 Automatic Dicing Saw.[14]
   (a) blade: 8 mil, $200\,\mu\mathrm{m}$ thick Thermocarbon diamond blade[15]
   (b) cutting speed: 0.5 mm/s.
5. Release the dicing tape with UV exposure of 90 s.
6. Remove the chip from the dicing tape.
7. Under the DI water goose neck, rinse the wafer with DI water for 30 s total.
8. Over a dish, squirt down both sides of the chip with acetone for 30 s and then immediately soak the chip in acetone in a new dish for 5 minutes to remove the dicing resist.
9. Soak in IPA for 5 minutes.
10. Blow dry with N_2 at 45 psi.
11. Inspect under microscope.

14. https://www.disco.co.jp/eg/products/dicer/index.html

15. http://www.thermocarbon.com/

BIBLIOGRAPHY

[1] P.W. Shor. Algorithms for quantum computation: discrete logarithms and factoring. In *Proceedings 35th Annual Symposium on Foundations of Computer Science*. IEEE Comput. Soc. Press, 1994.

[2] G. D. Fuchs, V. V. Dobrovitski, D. M. Toyli, F. J. Heremans, C. D. Weis, T. Schenkel, and D. D. Awschalom. Excited-state spin coherence of a single nitrogen–vacancy centre in diamond. *Nature Physics*, 6(9):668–672, 2010.

[3] William F. Koehl, Bob B. Buckley, F. Joseph Heremans, Greg Calusine, and David D. Awschalom. Room temperature coherent control of defect spin qubits in silicon carbide. *Nature*, 479(7371):84–87, 2011.

[4] Erik Lucero, R. Barends, Y. Chen, J. Kelly, M. Mariantoni, A. Megrant, P. O'Malley, D. Sank, A. Vainsencher, J. Wenner, T. White, Y. Yin, A. N. Cleland, and John M. Martinis. Computing prime factors with a josephson phase qubit quantum processor. *Nature Physics*, 8(10):719–723, 2012.

[5] Christopher R. Monroe, Robert J. Schoelkopf, and Mikhail D. Lukin. Quantum connections. *Scientific American*, 314(5):50–57, 2016.

[6] Jarryd J. Pla, Kuan Y. Tan, Juan P. Dehollain, Wee H. Lim, John J. L. Morton, David N. Jamieson, Andrew S. Dzurak, and Andrea Morello. A single-atom electron spin qubit in silicon. *Nature*, 489(7417):541–545, 2012.

[7] W. Huang, C. H. Yang, K. W. Chan, T. Tanttu, B. Hensen, R. C. C. Leon, M. A. Fogarty, J. C. C. Hwang, F. E. Hudson, K. M. Itoh, A. Morello, A. Laucht, and A. S. Dzurak. Fidelity benchmarks for two-qubit gates in silicon. *Nature*, 569(7757):532–536, 2019.

[8] Stephan Ritter, Christian Nölleke, Carolin Hahn, Andreas Reiserer, Andreas Neuzner, Manuel Uphoff, Martin Mücke, Eden Figueroa, Joerg Bochmann, and Gerhard Rempe. An

elementary quantum network of single atoms in optical cavities. *Nature*, 484(7393):195–200, 2012.

[9] David P. DiVincenzo. The physical implementation of quantum computation. *Fortschritte der Physik*, 48(9-11):771–783, 2000.

[10] M. H. Devoret and R. J. Schoelkopf. Superconducting circuits for quantum information: An outlook. *Science*, 339(6124):1169–1174, 2013.

[11] Frank Arute, Kunal Arya, Ryan Babbush, Dave Bacon, Joseph C. Bardin, Rami Barends, Rupak Biswas, Sergio Boixo, Fernando G. S. L. Brandao, David A. Buell, Brian Burkett, Yu Chen, Zijun Chen, Ben Chiaro, Roberto Collins, William Courtney, Andrew Dunsworth, Edward Farhi, Brooks Foxen, Austin Fowler, Craig Gidney, Marissa Giustina, Rob Graff, Keith Guerin, Steve Habegger, Matthew P. Harrigan, Michael J. Hartmann, Alan Ho, Markus Hoffmann, Trent Huang, Travis S. Humble, Sergei V. Isakov, Evan Jeffrey, Zhang Jiang, Dvir Kafri, Kostyantyn Kechedzhi, Julian Kelly, Paul V. Klimov, Sergey Knysh, Alexander Korotkov, Fedor Kostritsa, David Landhuis, Mike Lindmark, Erik Lucero, Dmitry Lyakh, Salvatore Mandrà, Jarrod R. McClean, Matthew McEwen, Anthony Megrant, Xiao Mi, Kristel Michielsen, Masoud Mohseni, Josh Mutus, Ofer Naaman, Matthew Neeley, Charles Neill, Murphy Yuezhen Niu, Eric Ostby, Andre Petukhov, John C. Platt, Chris Quintana, Eleanor G. Rieffel, Pedram Roushan, Nicholas C. Rubin, Daniel Sank, Kevin J. Satzinger, Vadim Smelyanskiy, Kevin J. Sung, Matthew D. Trevithick, Amit Vainsencher, Benjamin Villalonga, Theodore White, Z. Jamie Yao, Ping Yeh, Adam Zalcman, Hartmut Neven, and John M. Martinis. Quantum supremacy using a programmable superconducting processor. *Nature*, 574(7779):505–510, 2019.

[12] H. J. Kimble. The quantum internet. *Nature*, 453(7198):1023–1030, 2008.

[13] C. Monroe and J. Kim. Scaling the ion trap quantum processor. *Science*, 339(6124):1164–1169, 2013.

[14] Liang Jiang, Jacob M. Taylor, Anders S. Sørensen, and Mikhail D. Lukin. Distributed quantum computation based on small quantum registers. *Physical Review A*, 76(6):062323, 2007.

[15] B. Hensen, H. Bernien, A. E. Dréau, A. Reiserer, N. Kalb, M. S. Blok, J. Ruitenberg, R. F. L. Vermeulen, R. N. Schouten, C. Abellán, W. Amaya, V. Pruneri, M. W. Mitchell, M. Markham, D. J. Twitchen, D. Elkouss, S. Wehner, T. H. Taminiau, and R. Hanson. Loophole-free bell inequality violation using electron spins separated by 1.3 kilometres. *Nature*, 526(7575):682–686, 2015.

[16] Juan Yin, Yuan Cao, Yu-Huai Li, Sheng-Kai Liao, Liang Zhang, Ji-Gang Ren, Wen-Qi Cai, Wei-Yue Liu, Bo Li, Hui Dai, Guang-Bing Li, Qi-Ming Lu, Yun-Hong Gong, Yu Xu, Shuang-Lin Li, Feng-Zhi Li, Ya-Yun Yin, Zi-Qing Jiang, Ming Li, Jian-Jun Jia, Ge Ren, Dong He, Yi-Lin Zhou, Xiao-Xiang Zhang, Na Wang, Xiang Chang, Zhen-Cai Zhu, Nai-Le Liu, Yu-Ao Chen, Chao-Yang Lu, Rong Shu, Cheng-Zhi Peng, Jian-Yu Wang, and Jian-Wei Pan. Satellite-based entanglement distribution over 1200 kilometers. *Science*, 356(6343):1140–1144, 2017.

[17] Artur K. Ekert. Quantum cryptography based on bell's theorem. *Physical Review Letters*, 67(6):661–663, 1991.

[18] P. Kurpiers, P. Magnard, T. Walter, B. Royer, M. Pechal, J. Heinsoo, Y. Salathe, A. Akin, S. Storz, J.-C. Besse, S. Gasparinetti, A. Blais, and A. Wallraff. Deterministic quantum state transfer and remote entanglement using microwave photons. *Nature*, 558(7709):264–267, 2018.

[19] N. Roch, M. E. Schwartz, F. Motzoi, C. Macklin, R. Vijay, A. W. Eddins, A. N. Korotkov, K. B. Whaley, M. Sarovar, and I. Siddiqi. Observation of measurement-induced entanglement and quantum trajectories of remote superconducting qubits. *Physical Review Letters*, 112(17):170501, 2014.

[20] A. Narla, S. Shankar, M. Hatridge, Z. Leghtas, K. M. Sliwa, E. Zalys-Geller, S. O. Mundhada, W. Pfaff, L. Frunzio, R. J. Schoelkopf, and M. H. Devoret. Robust concurrent remote entanglement between two superconducting qubits. *Physical Review X*, 6(3):031036, 2016.

[21] C. Dickel, J. J. Wesdorp, N. K. Langford, S. Peiter, R. Sagastizabal, A. Bruno, B. Criger, F. Motzoi, and L. DiCarlo. Chip-to-chip entanglement of transmon qubits using engineered measurement fields. *Physical Review B*, 97(6):064508, 2018.

[22] J. I. Cirac, P. Zoller, H. J. Kimble, and H. Mabuchi. Quantum State Transfer and Entanglement Distribution among Distant Nodes in a Quantum Network. *Physical Review Letters*, 78(16):3221–3224, 1997.

[23] Alexander N. Korotkov. Flying microwave qubits with nearly perfect transfer efficiency. *Physical Review B*, 84(1):014510, 2011.

[24] Christopher J. Axline, Luke D. Burkhart, Wolfgang Pfaff, Mengzhen Zhang, Kevin Chou, Philippe Campagne-Ibarcq, Philip Reinhold, Luigi Frunzio, S. M. Girvin, Liang Jiang, M. H. Devoret, and R. J. Schoelkopf. On-demand quantum state transfer and entanglement between remote microwave cavity memories. *Nature Physics*, 14(7):705–710, 2018.

[25] P. Campagne-Ibarcq, E. Zalys-Geller, A. Narla, S. Shankar, P. Reinhold, L. Burkhart, C. Axline, W. Pfaff, L. Frunzio, R. J. Schoelkopf, and M. H. Devoret. Deterministic Remote Entanglement of Superconducting Circuits through Microwave Two-Photon Transitions. *Physical Review Letters*, 120(20):200501, 2018.

[26] N. Leung, Y. Lu, S. Chakram, R. K. Naik, N. Earnest, R. Ma, K. Jacobs, A. N. Cleland, and D. I. Schuster. Deterministic bidirectional communication and remote entanglement generation between superconducting qubits. *npj Quantum Information*, 5(1):18, 2019.

[27] Y. P. Zhong, H.-S. Chang, K. J. Satzinger, M.-H. Chou, A. Bienfait, C. R. Conner, É Dumur, J. Grebel, G. A. Peairs, R. G. Povey, D. I. Schuster, and A. N. Cleland. Violating Bell's

inequality with remotely connected superconducting qubits. *Nature Physics*, 15(8):741–744, 2019.

[28] A. Bienfait, K. J. Satzinger, Y. P. Zhong, H.-S. Chang, M.-H. Chou, C. R. Conner, É Dumur, J. Grebel, G. A. Peairs, R. G. Povey, and A. N. Cleland. Phonon-mediated quantum state transfer and remote qubit entanglement. *Science*, 364(6438):368–371, 2019.

[29] Michel H. devoret and John M. Martinis. Implementing qubits with superconducting integrated circuits. *Quantum Information Processing*, 3(1-5):163–203, 2004.

[30] David M. Pozar. *Microwave Engineering*. John Wiley and Sons Inc, 2011.

[31] A. Megrant, C. Neill, R. Barends, B. Chiaro, Yu Chen, L. Feigl, J. Kelly, Erik Lucero, Matteo Mariantoni, P. J. J. O'Malley, D. Sank, A. Vainsencher, J. Wenner, T. C. White, Y. Yin, J. Zhao, C. J. Palmstrøm, John M. Martinis, and A. N. Cleland. Planar superconducting resonators with internal quality factors above one million. *Applied Physics Letters*, 100(11):113510, 2012.

[32] Kevin J. Satzinger. *Quantum contol of surface acoustic wave phonons*. PhD thesis, University of California Santa Barbara, 2018.

[33] B.D. Josephson. Possible new effects in superconductive tunnelling. *Physics Letters*, 1(7):251–253, 1962.

[34] B. D. Josephson. The discovery of tunnelling supercurrents. *Reviews of Modern Physics*, 46(2):251–254, 1974.

[35] J. Bardeen, L. N. Cooper, and J. R. Schrieffer. Theory of superconductivity. *Physical Review*, 108(5):1175–1204, 1957.

[36] G. J. Dolan. Offset masks for lift-off photoprocessing. *Applied Physics Letters*, 31(5):337–339, 1977.

[37] David I. Schuster. *Circuit Quantum Electrodynamics*. PhD thesis, Yale University, 2007.

[38] Markus Ansmann. *Benchmarking the Superconducting Josephson Phase Qubit:The Violation of Bell's Inequality*. PhD thesis, University of California Santa Barbara, 2009.

[39] Charles Kittel. *Introduction to Solid State Physics*. John Wiley and Sons Inc, 2004.

[40] Jens Koch, Terri M. Yu, Jay Gambetta, A. A. Houck, D. I. Schuster, J. Majer, Alexandre Blais, M. H. Devoret, S. M. Girvin, and R. J. Schoelkopf. Charge-insensitive qubit design derived from the Cooper pair box. *Physical Review A*, 76(4):042319, 2007.

[41] R. Barends, J. Kelly, A. Megrant, D. Sank, E. Jeffrey, Y. Chen, Y. Yin, B. Chiaro, J. Mutus, C. Neill, P. O'Malley, P. Roushan, J. Wenner, T. C. White, A. N. Cleland, and John M. Martinis. Coherent Josephson Qubit Suitable for Scalable Quantum Integrated Circuits. *Physical Review Letters*, 111(8):080502, 2013.

[42] Julian S. Kelly. *Fault-tolerant superconducting qubit*. PhD thesis, University of California Santa Barbara, 2015.

[43] Daniel T. Sank. *Fast, Accurate State Measurement in Superconducting Qubits*. PhD thesis, University of California Santa Barbara, 2014.

[44] Evan Jeffrey, Daniel Sank, J. Y. Mutus, T. C. White, J. Kelly, R. Barends, Y. Chen, Z. Chen, B. Chiaro, A. Dunsworth, A. Megrant, P. J. J. O'Malley, C. Neill, P. Roushan, A. Vainsencher, J. Wenner, A. N. Cleland, and John M. Martinis. Fast Accurate State Measurement with Superconducting Qubits. *Physical Review Letters*, 112(19):190504, 2014.

[45] J. Kelly, R. Barends, A. G. Fowler, A. Megrant, E. Jeffrey, T. C. White, D. Sank, J. Y. Mutus, B. Campbell, Yu Chen, Z. Chen, B. Chiaro, A. Dunsworth, I.-C. Hoi, C. Neill, P. J. J. O'Malley, C. Quintana, P. Roushan, A. Vainsencher, J. Wenner, A. N. Cleland, and John M. Martinis. State preservation by repetitive error detection in a superconducting quantum circuit. *Nature*, 519(7541):66–69, 2015.

[46] E.T. Jaynes and F.W. Cummings. Comparison of quantum and semiclassical radiation theories with application to the beam maser. *Proceedings of the IEEE*, 51(1):89–109, 1963.

[47] Jean-Michel Raimond Serge Haroche. *Exploring the Quantum: Atoms, Cavities, and Photons*. OXFORD UNIV PR, 2006.

[48] Daniel Sank, Zijun Chen, Mostafa Khezri, J. Kelly, R. Barends, B. Campbell, Y. Chen, B. Chiaro, A. Dunsworth, A. Fowler, E. Jeffrey, E. Lucero, A. Megrant, J. Mutus, M. Neeley, C. Neill, P. J. J. O'Malley, C. Quintana, P. Roushan, A. Vainsencher, T. White, J. Wenner, Alexander N. Korotkov, and John M. Martinis. Measurement-induced state transitions in a superconducting qubit: Beyond the rotating wave approximation. *Physical Review Letters*, 117(19):190503, 2016.

[49] A. Dunsworth, R. Barends, Yu Chen, Zijun Chen, B. Chiaro, A. Fowler, B. Foxen, E. Jeffrey, J. Kelly, P. V. Klimov, E. Lucero, J. Y. Mutus, M. Neeley, C. Neill, C. Quintana, P. Roushan, D. Sank, A. Vainsencher, J. Wenner, T. C. White, H. Neven, John M. Martinis, and A. Megrant. A method for building low loss multi-layer wiring for superconducting microwave devices. *Applied Physics Letters*, 112(6):063502, 2018.

[50] Yu Chen, C. Neill, P. Roushan, N. Leung, M. Fang, R. Barends, J. Kelly, B. Campbell, Z. Chen, B. Chiaro, A. Dunsworth, E. Jeffrey, A. Megrant, J. Y. Mutus, P. J. J. O'Malley, C. M. Quintana, D. Sank, A. Vainsencher, J. Wenner, T. C. White, Michael R. Geller, A. N. Cleland, and John M. Martinis. Qubit Architecture with High Coherence and Fast Tunable Coupling. *Physical Review Letters*, 113(22):220502, 2014.

[51] Charles J. Neil. *A path towards quantum supremacy with superconducting qubits*. PhD thesis, University of California Santa Barbara, 2017.

[52] Michael R. Geller, Emmanuel Donate, Yu Chen, Michael T. Fang, Nelson Leung, Charles Neill, Pedram Roushan, and John M. Martinis. Tunable coupler for superconducting xmon qubits: Perturbative nonlinear model. *Physical Review A*, 92(1):012320, 2015.

[53] C. Neill, P. Roushan, M. Fang, Y. Chen, M. Kolodrubetz, Z. Chen, A. Megrant, R. Barends, B. Campbell, B. Chiaro, A. Dunsworth, E. Jeffrey, J. Kelly, J. Mutus, P. J. J. O'Malley, C. Quintana, D. Sank, A. Vainsencher, J. Wenner, T. C. White, A. Polkovnikov, and J. M. Martinis. Ergodic dynamics and thermalization in an isolated quantum system. *Nature Physics*, 12(11):1037–1041, 2016.

[54] P. Roushan, C. Neill, J. Tangpanitanon, V. M. Bastidas, A. Megrant, R. Barends, Y. Chen, Z. Chen, B. Chiaro, A. Dunsworth, A. Fowler, B. Foxen, M. Giustina, E. Jeffrey, J. Kelly, E. Lucero, J. Mutus, M. Neeley, C. Quintana, D. Sank, A. Vainsencher, J. Wenner, T. White, H. Neven, D. G. Angelakis, and J. Martinis. Spectroscopic signatures of localization with interacting photons in superconducting qubits. *Science*, 358(6367):1175–1179, 2017.

[55] Fei Yan, Philip Krantz, Youngkyu Sung, Morten Kjaergaard, Daniel L. Campbell, Terry P. Orlando, Simon Gustavsson, and William D. Oliver. Tunable coupling scheme for implementing high-fidelity two-qubit gates. *Physical Review Applied*, 10(5):054062, 2018.

[56] X. Li, T. Cai, H. Yan, Z. Wang, X. Pan, Y. Ma, W. Cai, J. Han, Z. Hua, X. Han, Y. Wu, H. Zhang, H. Wang, Yipu Song, Luming Duan, and Luyan Sun. Tunable coupler for realizing a controlled-phase gate with dynamically decoupled regime in a superconducting circuit. *Physical Review Applied*, 14(2):024070, 2020.

[57] Yuan Xu, Ji Chu, Jiahao Yuan, Jiawei Qiu, Yuxuan Zhou, Libo Zhang, Xinsheng Tan, Yang Yu, Song Liu, Jian Li, Fei Yan, and Dapeng Yu. High-fidelity, high-scalability two-qubit gate scheme for superconducting qubits. *arXiv preprint arXiv:2006.11860*, 2020.

[58] Michele C. Collodo, Johannes Herrmann, Nathan Lacroix, Christian Kraglund Andersen, Ants Remm, Stefania Lazar, Jean-Claude Besse, Theo Walter, Andreas Wallraff, and Christopher Eichler. Implementation of conditional-phase gates based on tunable zz-interactions. *arXiv preprint arXiv:2005.08863*, 2020.

[59] C. Lang, C. Eichler, L. Steffen, J. M. Fink, M. J. Woolley, A. Blais, and A. Wallraff. Correlations, indistinguishability and entanglement in hong–ou–mandel experiments at microwave frequencies. *Nature Physics*, 9(6):345–348, 2013.

[60] M. Pechal, J.-C. Besse, M. Mondal, M. Oppliger, S. Gasparinetti, and A. Wallraff. Superconducting switch for fast on-chip routing of quantum microwave fields. *Physical Review Applied*, 6(2):024009, 2016.

[61] O. Naaman, M. O. Abutaleb, C. Kirby, and M. Rennie. On-chip josephson junction microwave switch. *Applied Physics Letters*, 108(11):112601, 2016.

[62] Benjamin J. Chapman, Bradley A. Moores, Eric I. Rosenthal, Joseph Kerckhoff, and K. W. Lehnert. General purpose multiplexing device for cryogenic microwave systems. *Applied Physics Letters*, 108(22):222602, 2016.

[63] Steven Schuermans, Michaël Simoen, Martin Sandberg, Philip Krantz, C. M. Wilson, and Per Delsing. An on-chip mach-zehnder interferometer in the microwave regime. *IEEE Transactions on Applied Superconductivity*, 21(3):448–451, 2011.

[64] Baleegh Abdo. Lossless microwave switch based on tunable filters for quantum information processing, 2017.

[65] C. D. Tesche and J. Clarke. Dc squid - noise and optimization. *Journal of Low Temperature Physics*, 29(3-4):301–331, 1977.

[66] H.-S. Chang, Y. P. Zhong, A. Bienfait, M.-H. Chou, C. R. Conner, É. Dumur, J. Grebel, G. A. Peairs, R. G. Povey, K. J. Satzinger, and A. N. Cleland. Remote entanglement via adiabatic passage using a tunably dissipative quantum communication system. *Physical Review Letters*, 124(24):240502, 2020.

[67] Nikolay V. Vitanov, Andon A. Rangelov, Bruce W. Shore, and Klaas Bergmann. Stimulated Raman adiabatic passage in physics, chemistry, and beyond. *Reviews of Modern Physics*, 89(1):015006, 2017.

[68] Klaas Bergmann, Hanns-Christoph Nagerl, Cristian Panda, Gerald Gabrielse, Eduard Miloglyadov, Martin Quack, Georg Seyfang, Gunther Wichmann, Silke Ospelkaus, Axel Kuhn, Stefano Longhi, Alexander Szameit, Philipp Pirro, Burkard Hillebrands, Xue-Feng Zhu, Jie Zhu, Michael Drewsen, Winfried K Hensinger, Sebastian Weidt, Thomas Halfmann, Hai-Lin Wang, Gheorghe Sorin Paraoanu, Nikolay V Vitanov, Jordi Mompart, Thomas Busch, Timothy J Barnum, David D Grimes, Robert W Field, Mark G Raizen, Edvardas Narevicius, Marcis Auzinsh, Dmitry Budker, Adriana Pálffy, and Christoph H Keitel. Roadmap on STIRAP applications. *Journal of Physics B: Atomic, Molecular and Optical Physics*, 52(20):202001, 2019.

[69] Mika A. Sillanpaa, Jae I. Park, and Raymond W. Simmonds. Coherent quantum state storage and transfer between two phase qubits via a resonant cavity. *Nature*, 449(7161):438–442, 2007.

[70] Markus Ansmann, H. Wang, Radoslaw C. Bialczak, Max Hofheinz, Erik Lucero, M. Neeley, A. D. O'Connell, D. Sank, M. Weides, J. Wenner, A. N. Cleland, and John M. Martinis. Violation of Bell's inequality in Josephson phase qubits. *Nature*, 461(7263):504–506, 2009.

[71] Alexandre Blais, Ren-Shou Huang, Andreas Wallraff, S. M. Girvin, and R. J. Schoelkopf. Cavity quantum electrodynamics for superconducting electrical circuits: An architecture for quantum computation. *Physical Review A*, 69(6):062320, 2004.

[72] D. I. Schuster, A. Wallraff, A. Blais, L. Frunzio, R.-S. Huang, J. Majer, S. M. Girvin, and R. J. Schoelkopf. ac Stark Shift and Dephasing of a Superconducting Qubit Strongly Coupled to a Cavity Field. *Physical Review Letters*, 94(12):123602, 2005.

[73] A. Wallraff, D. I. Schuster, A. Blais, L. Frunzio, J. Majer, M. H. Devoret, S. M. Girvin, and R. J. Schoelkopf. Approaching Unit Visibility for Control of a Superconducting Qubit with Dispersive Readout. *Physical Review Letters*, 95(6):060501, 2005.

[74] C. Macklin, K. O'Brien, D. Hover, M. E. Schwartz, V. Bolkhovsky, X. Zhang, W. D. Oliver, and I. Siddiqi. A near-quantum-limited Josephson traveling-wave parametric amplifier. *Science*, 350(6258):307–310, 2015.

[75] H.-S. Chang, Y. P. Zhong, K. J. Satzinger, M.-H. Chou, A. Bienfait, C. R. Conner, É Dumur, J. Grebel, G. A. Peairs, R. G. Povey, and A. N. Cleland. A fast and large bandwidth superconducting variable coupler. *Submitted*, 2020.

[76] Ying-Dan Wang and Aashish A Clerk. Using dark modes for high-fidelity optomechanical quantum state transfer. *New Journal of Physics*, 14(10):105010, 2012.

[77] Ying-Dan Wang, Rong Zhang, Xiao-Bo Yan, and Stefano Chesi. Optimization of STIRAP-based state transfer under dissipation. *New Journal of Physics*, 19(9):093016, 2017.

[78] Matthew Neeley, M. Ansmann, Radoslaw C. Bialczak, M. Hofheinz, N. Katz, Erik Lucero, A. O'Connell, H. Wang, A. N. Cleland, and John M. Martinis. Process tomography of quantum memory in a Josephson-phase qubit coupled to a two-level state. *Nature Physics*, 4(7):523–526, 2008.

[79] M. Steffen, M. Ansmann, R. C. Bialczak, N. Katz, E. Lucero, R. McDermott, M. Neeley, E. M. Weig, A. N. Cleland, and J. M. Martinis. Measurement of the Entanglement of Two Superconducting Qubits via State Tomography. *Science*, 313(5792):1423–1425, 2006.

[80] Matthew Neeley, Radoslaw C. Bialczak, M. Lenander, E. Lucero, Matteo Mariantoni, A. D. O'Connell, D. Sank, H. Wang, M. Weides, J. Wenner, Y. Yin, T. Yamamoto, A. N. Cleland, and John M. Martinis. Generation of three-qubit entangled states using superconducting phase qubits. *Nature*, 467(7315):570–573, 2010.

[81] J. M. Chow, L. DiCarlo, J. M. Gambetta, A. Nunnenkamp, Lev S. Bishop, L. Frunzio, M. H. Devoret, S. M. Girvin, and R. J. Schoelkopf. Detecting highly entangled states with a joint qubit readout. *Physical Review A*, 81(6):062325, 2010.

[82] William K. Wootters. Entanglement of Formation of an Arbitrary State of Two Qubits. *Physical Review Letters*, 80(10):2245–2248, 1998.

[83] Martin B. Plenio and S. Virmani. An introduction to entanglement measures. *arXiv preprint arXiv:quant-ph/0504163*, 2006. arXiv: quant-ph/0504163.

[84] H. K. Xu, C. Song, W. Y. Liu, G. M. Xue, F. F. Su, H. Deng, Ye Tian, D. N. Zheng, Siyuan Han, Y. P. Zhong, H. Wang, Yu-xi Liu, and S. P. Zhao. Coherent population transfer between uncoupled or weakly coupled states in ladder-type superconducting qutrits. *Nature Communications*, 7(1):11018, 2016.

[85] K. Bergmann, H. Theuer, and B. W. Shore. Coherent population transfer among quantum states of atoms and molecules. *Reviews of Modern Physics*, 70(3):1003–1025, 1998.

[86] Bruce W. Shore. *Manipulating quantum structures using laser pulses*. Cambridge University Press, Cambridge, UK ; New York, 2011.

[87] Marlan O. Scully and Muhammad Suhail Zubairy. *Quantum optics*. Cambridge University Press, Cambridge ; New York, 1997.

[88] G. S. Vasilev, A. Kuhn, and N. V. Vitanov. Optimum pulse shapes for stimulated Raman adiabatic passage. *Physical Review A*, 80(1):013417, 2009.

[89] S. Guerin, S. Thomas, and H. R. Jauslin. Optimization of population transfer by adiabatic passage. *Physical Review A*, 65(2):023409, 2002.

[90] T. Pellizzari. Quantum Networking with Optical Fibres. *Physical Review Letters*, 79(26):5242–5245, 1997.

[91] B Vogell, B Vermersch, T E Northup, B P Lanyon, and C A Muschik. Deterministic quantum state transfer between remote qubits in cavities. *Quantum Science and Technology*, 2(4):045003, 2017.

[92] G. Lindblad. On the generators of quantum dynamical semigroups. *Communications in Mathematical Physics*, 48(2):119–130, 1976.

[93] Daniel F. Walls and Gerard J. Milburn. *Quantum optics*. Springer, Berlin, 2. ed edition, 2008.

[94] J.R. Johansson, P.D. Nation, and Franco Nori. QuTiP: An open-source Python framework for the dynamics of open quantum systems. *Computer Physics Communications*, 183(8):1760–1772, 2012.

[95] Peter J. Mosley, Jeff S. Lundeen, Brian J. Smith, Piotr Wasylczyk, Alfred B. U'Ren, Christine Silberhorn, and Ian A. Walmsley. Heralded Generation of Ultrafast Single Photons in Pure Quantum States. *Physical Review Letters*, 100(13):133601, 2008.

[96] Koji Azuma, Kiyoshi Tamaki, and Hoi-Kwong Lo. All-photonic quantum repeaters. *Nature Communications*, 6(1):6787, 2015.

[97] P. Kurpiers, M. Pechal, B. Royer, P. Magnard, T. Walter, J. Heinsoo, Y. Salathe, A. Akin, S. Storz, J.-C. Besse, S. Gasparinetti, A. Blais, and A. Wallraff. Quantum Communication with Time-Bin Encoded Microwave Photons. *Physical Review Applied*, 12(4):044067, 2019.

[98] Paul G. Kwiat, Salvador Barraza-Lopez, Andre Stefanov, and Nicolas Gisin. Experimental entanglement distillation and hidden non-locality. *Nature*, 409(6823):1014–1017, 2001.

[99] Ruifang Dong, Mikael Lassen, Joel Heersink, Christoph Marquardt, Radim Filip, Gerd Leuchs, and Ulrik L. Andersen. Experimental entanglement distillation of mesoscopic quantum states. *Nature Physics*, 4(12):919–923, 2008.

[100] Hiroki Takahashi, Jonas S. Neergaard-Nielsen, Makoto Takeuchi, Masahiro Takeoka, Kazuhiro Hayasaka, Akira Furusawa, and Masahide Sasaki. Entanglement distillation from Gaussian input states. *Nature Photonics*, 4(3):178–181, 2010.

[101] J. F. Poyatos, J. I. Cirac, and P. Zoller. Quantum Reservoir Engineering with Laser Cooled Trapped Ions. *Physical Review Letters*, 77(23):4728–4731, 1996.

[102] M. B. Plenio and S. F. Huelga. Entangled Light from White Noise. *Physical Review Letters*, 88(19):197901, 2002.

[103] Sylvain Hermelin, Shintaro Takada, Michihisa Yamamoto, Seigo Tarucha, Andreas D. Wieck, Laurent Saminadayar, Christopher Bauerle, and Tristan Meunier. Electrons surfing on a sound wave as a platform for quantum optics with flying electrons. *Nature*, 477(7365):435–438, 2011.

[104] R. P. G. McNeil, M. Kataoka, C. J. B. Ford, C. H. W. Barnes, D. Anderson, G. A. C. Jones, I. Farrer, and D. A. Ritchie. On-demand single-electron transfer between distant quantum dots. *Nature*, 477(7365):439–442, 2011.

[105] Alexandre Baksic, Hugo Ribeiro, and Aashish A. Clerk. Speeding up Adiabatic Quantum State Transfer by Using Dressed States. *Physical Review Letters*, 116(23):230503, 2016.

[106] Brian B. Zhou, Alexandre Baksic, Hugo Ribeiro, Christopher G. Yale, F. Joseph Heremans, Paul C. Jerger, Adrian Auer, Guido Burkard, Aashish A. Clerk, and David D. Awschalom. Accelerated quantum control using superadiabatic dynamics in a solid-state lambda system. *Nature Physics*, 13(4):330–334, 2017.

[107] Boyan T. Torosov, Stephane Guerin, and Nikolay V. Vitanov. High-Fidelity Adiabatic Passage by Composite Sequences of Chirped Pulses. *Physical Review Letters*, 106(23):233001, 2011.

[108] Alexander Bruns, Genko T. Genov, Marcel Hain, Nikolay V. Vitanov, and Thomas Halfmann. Experimental demonstration of composite stimulated Raman adiabatic passage. *Physical Review A*, 98(5):053413, 2018.

[109] Philipp Kurpiers, Theodore Walter, Paul Magnard, Yves Salathe, and Andreas Wallraff. Characterizing the attenuation of coaxial and rectangular microwave-frequency waveguides at cryogenic temperatures. *EPJ Quantum Technology*, 4(1), 2017.

[110] David B Tuckerman, Michael C Hamilton, David J Reilly, Rujun Bai, George A Hernandez, John M Hornibrook, John A Sellers, and Charles D Ellis. Flexible superconducting nb transmission lines on thin film polyimide for quantum computing applications. *Superconductor Science and Technology*, 29(8):084007, 2016.

[111] Kevin C. Miao, Joseph P. Blanton, Christopher P. Anderson, Alexandre Bourassa, Alexander L. Crook, Gary Wolfowicz, Hiroshi Abe, Takeshi Ohshima, and David D. Awschalom. Universal coherence protection in a solid-state spin qubit. *Science*, page eabc5186, 2020.

[112] Ziwen Huang, Pranav S. Mundada, András Gyenis, David I. Schuster, Andrew A. Houck, and Jens Koch. Engineering dynamical sweet spots to protect qubits from $1/f$ noise. *arXiv preprint arXiv:2004.12458*, 2020.

[113] K. J. Satzinger, Y. P. Zhong, H.-S. Chang, G. A. Peairs, A. Bienfait, Ming-Han Chou, A. Y. Cleland, C. R. Conner, É Dumur, J. Grebel, I. Gutierrez, B. H. November, R. G. Povey, S. J. Whiteley, D. D. Awschalom, D. I. Schuster, and A. N. Cleland. Quantum control of surface acoustic-wave phonons. *Nature*, 563(7733):661–665, 2018.

[114] Youpeng Zhong. *Violating Bell's Inequality with remotely-connected superconducting qubits*. PhD thesis, Unversity of Chicago, 2019.

[115] K. J. Satzinger, C. R. Conner, A. Bienfait, H.-S. Chang, Ming-Han Chou, A. Y. Cleland, É. Dumur, J. Grebel, G. A. Peairs, R. G. Povey, S. J. Whiteley, Y. P. Zhong, D. D. Awscha-

lom, D. I. Schuster, and A. N. Cleland. Simple non-galvanic flip-chip integration method for hybrid quantum systems. *Applied Physics Letters*, 114(17):173501, 2019.

[116] A. Bienfait, Y. P. Zhong, H.-S. Chang, M.-H. Chou, C. R. Conner, É. Dumur, J. Grebel, G. A. Peairs, R. G. Povey, K. J. Satzinger, and A. N. Cleland. Quantum erasure using entangled surface acoustic phonons. *Physical Review X*, 10(2):021055, 2020.

[117] A. Dunsworth, A. Megrant, C. Quintana, Zijun Chen, R. Barends, B. Burkett, B. Foxen, Yu Chen, B. Chiaro, A. Fowler, R. Graff, E. Jeffrey, J. Kelly, E. Lucero, J. Y. Mutus, M. Neeley, C. Neill, P. Roushan, D. Sank, A. Vainsencher, J. Wenner, T. C. White, and John M. Martinis. Characterization and reduction of capacitive loss induced by sub-micron josephson junction fabrication in superconducting qubits. *Applied Physics Letters*, 111(2):022601, 2017.

[118] Sami Franssila. *Introduction to Microfabrication*. John Wiley & Sons, Ltd, 2010.